FUNDAMENTAL STUDIES IN QUADRUPOLE ION TRAP MASS SPECTROMETRY

By

RANDALL ERNEST PEDDER

A DISSERTATION PRESENTED TO THE GRADUATE SCHOOL
OF THE UNIVERSITY OF FLORIDA IN PARTIAL FULFILLMENT
OF THE REQUIREMENTS FOR THE DEGREE OF
DOCTOR OF PHILOSOPHY

UNIVERSITY OF FLORIDA

1992

UNIVERSITY OF FLORIDA LIBRARIES

This dissertation is dedicated to my mother and in memory of my father.

ACKNOWLEDGEMENTS

First, I want to thank those people who helped me in my undergraduate chemistry studies at Saint Vincent College, particularly Professor Suzan Maxey, whose insight and guidance led me to make such an educated and wise choice of a graduate school, and Professors Andrew Turner and Shawn Shanmugam, whom I consider both friends and advisors. I would also like to acknowledge my college history professor, Roy Mills, for teaching me how to study and interpret history; the study of the historical aspects of science and mass spectrometry have brought me much insight and pleasure.

I would like to acknowledge the people in the Yost research group who have offered encouragement, advice and guidance on projects. I am especially grateful to Dr. Jodie Johnson, who, depending on the occasion, has acted as advisor, devil's advocate, relentless reminder of deadlines, research partner, and most importantly, friend. A significant number of figures presented in this dissertation were either provided or reworked by Dr. Johnson through the course of our various joint presentations and publications. I will be forever haunted by variations of phrases such as "A dissertation of a thousand pages starts with the first word."

Thanks are extended to Professor John Eyler and Dr. Clifford Watson for their many insightful discussions on ion trajectory modeling and gas-phase dynamics. Dr. Watson provided the BASIC code used to perform FFT's in HyperIon.

I would like to thank those people at Finnigan Corporation who made my six-month co-operative study such a fun and educational experience. Finnigan Corporation is fortunate indeed to have such a concentration of talent under one roof. Barry Boole, Jim Hurst, Gloria Kirchner, Dr. Alan Schoen, John Syka, David Tucker, Steve Kirkish, Dennis Taylor, and Dr. George Stafford are acknowledged for their advice, encouragement, and constructive kibitzing. I would like to thank Dr. Michael Weber-Grabau for his effective management of my project while I was in San Jose. I would like to thank Paul Kelly and Mike Story of Finnigan Corporation, and Carla Wong at NASA Ames Research Center (and of course Professor Richard A. Yost) for helping to arrange for my co-operative study. Finally, I would like to extend my thanks to William Fies, Jr. for providing the original source code for the simulation program, Hyperlon, as well as providing many pleasant afternoons of discussions and training on subjects ranging from ion optics and electronics to trains.

I am grateful to the many people at Millipore Extrel who have supported my aspirations to finish my dissertation this year. Gary Astle, Greg Cessna, Dr. Stephen Penn, and especially Dr. Ross Willoughby are acknowledged for providing me with a flexible work schedule. Dr. Stephen Penn also provided numerous insightful discussions on ionization, gas phase dynamics, and ion motion modeling.

I am thankful to my sisters (in-law) Tina Pedder and Laura Pedder for their rallying support in the typing and formatting of this dissertation.

Thanks are extended to the United States Army Chemical Research, Development, and Engineering Center, Teledyne CME, NASA, and Finnigan Corporation, which provided support for me and the projects I worked on while at the University of Florida.

I would like to thank Dr. Richard A. Yost for supporting my research at the University of Florida, for allowing me the freedom to innovate within the projects, for teaching me how to do science, and for his undying patience in my extended dissertation-writing period. I would also like to thank Katie Yost for sharing her husband during the numerous extended late-night long-distance telephone calls over the last three years.

Finally, I would like to acknowledge my parents and family, without whose love, support, sacrifices, and encouragement I could not have made it this far.

TABLE OF CONTENTS

ACKNOWLEDGEMENTS iii

LIST OF FIGURES ix

LIST OF TABLES xv

ABSTRACT xvi

CHAPTER

1 INTRODUCTION 1
  - Organization of Dissertation 1
  - Historical Development of the Quadrupole Ion Trap Mass Spectrometer 4

2 THEORY OF QUADRUPOLE ION TRAP OPERATION 10
  - Derivation of the Mathieu Equation 12
  - Analytical Solution of the Mathieu Equation 22
    - Calculation of β and Coefficients for Analytical Solution of Mathieu Equation 23
    - Calculated Coefficients for the Analytical Solution 26
  - Calculation of Ion Velocity and Ion Kinetic Energy 33
    - Pseudopotential Well Method for Calculation of Ion Velocity and Ion Kinetic Energy 34
    - Expanded Analytical Solution Method for Calculation of Ion Velocity and Kinetic Energy 38
  - Mathieu Stability Diagrams 53
    - Stability Diagrams Scaled to m/z 55
    - Positive and Negative Ion Stability Diagrams 55
    - Mass-Selective Instability 58
    - Correspondence Between q, β, and Secular Frequency . . . 58
    - Correspondence Between q and m/z 60
    - Correspondence Between q, β, and Secular Frequency . . . 60
    - Analysis of Frequencies in the r Direction 60
  - Conclusions 64

3 SIMULATION OF ION MOTION AND MODELING OF ION ENERGETICS IN A QUADRUPOLE ION TRAP 67
  - Introduction 67
  - Numerical Integration of the Mathieu Equation 68

Previous Work in Computer Simulation of Ion Motion in Quadrupole Devices 68
The HyperIon Numerical Integration Program 71
Experimental Conditions for HyperIon Numerical Integration 72
HyperIon Simulation Example: Simulation of the Trajectory of Wuerker's Stored Microparticle. 74
HyperIon Modeling of Resonance Excitation 79
Theoretical Aspects of Ion Injection 89
Phase Space Dynamics 90
Conclusions 99

4 SIMULATION AND EXPERIMENTAL CHARACTERIZATION OF ELECTRON ENERGY IN A QUADRUPOLE ION TRAP 102
Introduction 102
Electron Ionization 102
Electron-Capture Negative Chemical Ionization 103
Electron Energy 104
Simulation Studies 105
Experimental Conditions for Simulation Studies 105
Simulation Studies Results and Discussion 108
Calculated Residence Time of Helium Ions 119
Laboratory Studies 120
Experimental Conditions for Laboratory Experiments 120
Experimental Correlation of RF Voltage with Effective Electron Energy 122
Experimental Evidence for Electron-Capture Negative Chemical Ionization 126
Contributions of Charge Exchange to Electron Ionization in a Quadrupole Ion Trap 131
Conclusions and Future Work 135

5 OFF-AXIS ION INJECTION INTO A QUADRUPOLE ION TRAP WITH A QUADRUPOLE DEFLECTOR 139
Introduction 139
Previous Work in Injection of Ions into a Quadrupole Ion Trap 141
The Ideal Ion Injection System 143
Injection Optics Options 146
Bessel Box 149
Different Uses of Quadrupole Fields 150
Simion Modeling of Quadrupole Deflector Injection System 153
Energy Dependence of Quadrupole Deflector 155
Angular Acceptance of Quadrupole Deflector Design 157
Positional Acceptance of Quadrupole Deflector Design 157
Variations of the Quadrupole Deflector 160
Experimental Design 163
Experimental Results and Discussion 167

Initial Attempts to Obtain Spectra 167
Multiplier Noise 170
Ion Injection Time 174
Collection Efficiency Measurements 174
Energy Acceptance of Quadrupole Deflector Ion Injection System . 185
Transmission and Detection Efficiencies 194
Conclusions 203

6 CONCLUSIONS AND FUTURE WORK 206
Conclusions 206
Future Work 211

APPENDIX A
ANALYTIC.BAS SOURCE CODE 216

APPENDIX B
HYPERION.BAS SOURCE CODE 221

REFERENCES 234

BIOGRAPHICAL SKETCH 243

LIST OF FIGURES

Figure 1-1: Schematic drawing of a quadrupole ion trap analyzer. 5

Figure 2-1: Equipotential contours for an ideal quadrupole ion trap. Quadrupolar field lines were calculated by solving equation 2.1. . . . 13

Figure 2-2: Dipolar equipotential contours plotted for a quadrupole ion trap. Note that the plate capacitor approximation is reasonable near the radial center of the ion trap but errs with significant radial distance. 14

Figure 2-3: Relative amplitudes of coefficients (C_{2n} from equation 2.42) plotted as a function of the Mathieu parameter q for RF-only operation of the quadrupole ion trap. 28

Figure 2-4: Relative amplitudes of coefficients (C_{2n} from equation 2.42) plotted as a function of β for RF-only operation of the quadrupole ion trap. 29

Figure 2-5: Relative amplitudes (C_{2n}) as a function of resonant frequencies ($\omega_n/2\pi$) for various values of q. Frequency ranges of fundamental (n=0) and first nine harmonic frequencies (n=+-1 to +-5) are indicated. 31

Figure 2-6: Relative amplitudes (C_{2n}) as a function of frequency (ω_n). Frequency ranges of the fundamental and three harmonics (n= 0, -1, +1, -2) are indicated. Additional data points were calculated using HyperIon. 32

Figure 2-7: Velocity components from table 2-3 plotted as a function of β. 48

Figure 2-8: Maximum ion velocities from table 2-4 plotted as a function of β. . . 50

Figure 2-9: Maximum ion kinetic energies from table 2-5 plotted as a function of β. 52

Figure 2-10: Mathieu stability diagram for the first stability region showing iso-β lines. 54

Figure 2-11: Mathieu stability diagrams for the positive ions m/z 17, 18, and 19, plotted in RF-DC space. 56

Figure 2-12: Mathieu stability diagrams for the positive (dotted lines) and negative (solid lines) ions of mass 17 plotted in RF-DC space. 57

Figure 2-13: Theoretical RF voltage calibration curve for mass selective instability operation of the quadrupole ion trap. $q_{instability}$ was taken as 0.908. $V_{0\text{-}p}$ equals 12.477 times m/z. 59

Figure 2-14: Correspondence between the Mathieu parameter q_z and β_r, β_z and secular (fundamental) frequency (ω_0). $\omega_0 = \beta\Omega_0/2$ 61

Figure 2-15: Correspondence between mass and the Mathieu parameter q with a constant RF voltage corresponding to m_{cutoff} = 10 amu. 62

Figure 2-16: Correspondence between mass and β_z and secular frequency for RF-only operation with a constant RF voltage corresponding to m_{cutoff} = 10 amu. 63

Figure 3-1: Two-to-one Lissajous figure representing the a projection into the r-z plane of the trajectory of an ion stored in the ion trap with a=0 and q=0.232, corresponding to those noted in the figure caption of Figure 7 of reference 4. 75

Figure 3-2: z trajectory plotted as a function of time with fast Fourier transform corresponding to the ion trajectory shown in Figure 3-1. Fundamental frequency is calculated to be 90 kHz from the fast Fourier transform. 76

Figure 3-3: r trajectory plotted as a function of time with fast Fourier transform corresponding to the ion trajectory shown in Figure 3-1. Fundamental frequency is calculated to be 45 kHz from the fast Fourier transform. 77

Figure 3-4: Simulated resonance excitation trajectory of m/z 134 in the z direction as a function of time. q_z=0.3, resonance excitation voltage and frequency were 1000 $mV_{p\text{-}p}$ at 118.8 kHz. 81

Figure 3-5: Fluence calculated via HyperIon for m/z 134 plotted as a function of the Mathieu parameter q_z. 84

Figure 3-6: Simulated HyperIon resonance excitation experiment for m/z 134 at a q_z of 0.905. 85

Figure 3-7: Maximum axial and radial energies for m/z 134 as a function of q_z and m_{cutoff}. Energies were calculated using the expanded analytical solution model of ion energetics, presented in Chapter 2. 88

Figure 3-8: Phase space diagram for the z coordinate of an ion stored in the quadrupole ion trap with q_z=0.05. Each ellipse is labeled with the RF phase angle at which its data points were sampled. 91

Figure 3-9: Phase space diagram for the z coordinate of an ion stored in the quadrupole ion trap with q_z=0.3. Each ellipse is labeled with the RF phase angle at which its data points were sampled. 92

Figure 3-10: Phase space diagram for the z coordinate of an ion stored in the quadrupole ion trap with q_z=0.9. Each ellipse is labeled with the RF phase angle at which its data points were sampled. 93

Figure 3-11: Maximum ion velocities as a function of mass for ions stored in a quadrupole ion trap with RF voltage set to correspond with m_{cutoff} of 10 amu. 96

Figure 3-12: Maximum ion kinetic energies as a function of mass for ions stored in a quadrupole ion trap with RF voltage set to correspond with m_{cutoff} of 10 amu. 98

Figure 4-1: Mathieu stability diagrams for the positive and negative ions of m/z 17 plotted in RF-DC space. Point A corresponds to 164.1 volts RF, and 0 volts DC. Points B and C correspond to 164.1 volts RF with -/+ 15.8 volts DC. 107

Figure 4-2: Electron trajectories corresponding to initial RF phases of 0, 90, and 180 degrees. 109

Figure 4-3: Electron trajectories for electrons with initial incidence angles of 0, 20, 40, 60, and 80 degrees. 112

Figure 4-4: Electron energy as a function of initial RF phase angle. Initial electron energy is 12.5 eV. The inset identifies normalized RF voltage as a function of RF phase. 113

Figure 4-5: Maximum electron energy as a function of initial RF phase angle for electrons injected at RF and DC voltages for points A, B, and C in Figure 4-1. The inset identifies normalized RF voltage as a function of RF phase. 115

Figure 4-6: Electron energy as a function of RF voltage low-mass cutoff for scan lines which pass through the origin of Figure 4-1 and through each of points A, B, and C. Initial electron energy is 12.5 eV. 116

Figure 4-7: Electron transit time and distance traveled as a function of the initial RF phase angle. Inset identifies normalized RF voltage as a function of RF phase. 118

Figure 4-8: Helium ion (m/z 4) trajectory for an ion created near the geometric center of the ion trap. Initial conditions: 'x'= 0.000001 m, 'z'=0.00001 m, RF phase angle = 0°, RF voltage: 10 amu low mass cutoff. 121

Figure 4-9: Normalized ion intensities of selected fragment ions of n-butylbenzene plotted along with ionization cross section data for a typical organic molecule (C_2H_2) (4-13). 123

Figure 4-10: Theoretical stability diagrams for positive and negative ions of perfluorotributylamine with experimentally determined boundaries. . . 128

Figure 4-11: Positive and negative ions of perfluorotributylamine plotted as a function of DC voltage applied to the ring electrode just prior to the analytical scan, with RF voltage set to a low mass cutoff of 270 amu. 129

Figure 4-12: Acquired spectra demonstrating simultaneous storage and detection of positive and negative ions of perfluorotributylamine. Spectra correspond to points indicated in Figure 4-11. 130

Figure 4-13: Effect of helium, nitrogen, and oxygen charge exchange on apparent energetics of electron ionization of n-butylbenzene. 133

Figure 5-1: Ion optical devices considered for this system. The devices shown are: (a) Bessel box, (b) split tubular lens, (c) Balzers off-axis lens system, (d) quadrupole deflector, (e) tandem quadrupole deflector, (f) monopole deflector 148

Figure 5-2: Schematic of a quadrupole deflector built from round rods. The grounded shield lenses are used to create a field free region for transmission of ions into and out of the hyperbolic field. 152

Figure 5-3: SIMION simulation showing the energy dependance of ion transmission through the quadrupole deflector. The trajectories correspond to initial ion energies of 15, 25, 35, 45, 55, and 65 eV from left to right. 156

Figure 5-4: Angular acceptance of ion injection optics. Initial angles ranged from -50° to +50°. 158

Figure 5-5: Positional acceptance of ion injection optics. The trajectories are shown starting at various initial positions at the exit aperture of the ion source. 159

Figure 5-6: Enlarged view of trajectory shown in Figure 5-5 which shows the defocusing effect of the entrance endcap of the ion trap analyzer. . 161

Figure 5-7: SIMION simulation of tandem quadrupole deflectors. Initial conditions were 0.25 eV initial energy with various initial angles. . . 162

Figure 5-8: Final design of quadrupole deflector ion injection system. 164

Figure 5-9: Early mass spectrum of perfluorotributylamine ions injected from an EI source. Ion energy is nominally 6 eV. 169

Figure 5-10: Methane ECNCI mass spectrum of injected perfluorotributylamine ions. Ion source pressure was 200 millitorr methane. Note the improper mass assignment of m/z's 557 and 595. 171

Figure 5-11: Profile mass spectrum of injected perfluorotributylamine negative ion m/z 633. 172

Figure 5-12: Multiplier background noise: (a) Filament off; (b) Filament on, with ions deflected 180° from ion trap analyzer. 173

Figure 5-13: Intensities of bromine negative ions m/z 79 and 81 from chemical ionization of bromobenzene plotted as a function of trapping RF voltage during ion injection. 175

Figure 5-14: Intensity ratio of bromine negative ions m/z 79 over m/z 81, plotted as a function of trapping RF voltage during ion injection. . . . 177

Figure 5-15: The intensities for the two bromine isotopes shown in Figure 5-13, plotted as a function of the Mathieu parameter q. 178

Figure 5-16: Intensity of the argon positive ion m/z 40 plotted as a function of the Mathieu parameter q. Nominal injected ion energy is 5 eV. . . . 181

Figure 5-17: Intensity of the argon positive ion m/z 40 plotted as a function of the Mathieu parameter q. Nominal injected ion energy is 40 eV. . . 182

Figure 5-18: Intensity of the argon positive ion m/z 40 plotted as a function of the Mathieu parameter q. Nominal injected ion energy is 70 eV. . . 183

Figure 5-19: A schematic representation of the stopping potential experiment. The source voltage, extraction voltage, and tube lens voltage were kept constant while the stopping voltage was varied. 187

Figure 5-20: Results from the stopping potential experiment with a -10 volt extraction voltage. Measured ion current is plotted as a function of stopping plate voltage. The first derivative of this trace represents a histogram of energy distributions. 188

Figure 5-21: SIMION plot showing the field penetration of the extraction voltage into the ion source. Equipotential contours correspond to +9, +6, +3, -10, and -30 volts (from left to right). 189

Figure 5-22: Results from the stopping potential experiment with a -314 volt extraction voltage. Measured ion current is plotted as a function of stopping plate voltage. The first derivative of this trace represents a histogram of energy distributions. 191

Figure 5-23: Ion current plotted as a function of source potential, measured at various places in the quadrupole deflector system. The source voltage was varied, with a constant potential applied to the extraction and tube lenses. 193

Figure 5-24: Summary of the transmission efficiencies of the quadrupole deflector injection system with an ion source potential of 8 volts. . . 195

Figure 5-25: Percentage of ion current which travels through the entrance endcap of the ion trap analyzer plotted as a function of source potential. 200

Figure 5-26: Detection efficiencies of ion injection system plotted as a function of ion source potential. 202

LIST OF TABLES

Table 2-1: Normalized coefficients ($|C_{2n}|$) in percent, from equation 2.41, calculated through solution of equation 2.45. These values were calculated using the BASIC program Analytic which is reproduced in Appendix A. 42

Table 2-2: Frequencies of ion motion ($\omega_0/2\pi$) in kilohertz for various values of q and β as calculated using equation 2.44, with $\Omega_0/2\pi$ taken as 1.1 MHz. Negative signs represent phase information. 43

Table 2-3: Scaled velocity terms ($A|C_{2n}\omega_n|$) with A taken as z radius for stretched ion trap (A=0.007825 m). C_{2n} and ω_n taken from Tables 2-1 and 2-2. All velocities are in meters/second. 44

Table 2-4: Maximum ion velocities in the z direction calculated via various methods. All velocities are in meters/second. See text for details. 45

Table 2-5: Maximum ion kinetic energies for m/z 134 calculated via various methods. All kinetic energies are in units of eV. Ring RF Voltage is included for comparison. See text for details. 46

Table 3-1: Comparison between normalized coefficients (C_{2n}) calculated using equation 2.48, and frequencies calculated through solution of equation 2.47 with coefficients and frequencies calculated using HyperIon. 78

Table 3-2: Fluences required for ejection of m/z 134 calculated as a function of q. March data were taken from Table 2 of reference 25; Resonance excitation voltage was 1 V_{0-p}. 82

Abstract of Dissertation Presented to the Graduate School
of the University of Florida in Partial Fulfillment of the
Requirements for the Degree of Doctor of Philosophy

FUNDAMENTAL STUDIES IN QUADRUPOLE ION TRAP MASS SPECTROMETRY

By

Randall Ernest Pedder

December 1992

Chairperson: Dr. Richard A. Yost
Major Department: Chemistry

The quadrupole ion trap, although it dates back to Nobel prize-winning work by Wolfgang Paul in 1953, has only in the last decade emerged as a commonly used analytical mass spectrometer. Recent advances have added some remarkable capabilities to quadrupole ion trap operation. Development and refinement of these new capabilities requires understanding of the fundamental principles of ion trap operation.

The physics of the quadrupole ion trap mass spectrometer was studied theoretically and experimentally. A rigorous derivation of the Mathieu equation of ion motion is presented, including an additional term to model the effects of the application of a supplemental AC resonance excitation voltage, based on the assumption that the field is similar to that of a plate capacitor.

Ion trajectories and maximum kinetic energies (pseudo-potential well depth) were calculated for ions stored in the quadrupole ion trap. A new method for calculating the maximum kinetic energy for ions stored in a quadrupole ion trap is proposed. Numerical integration of the Mathieu equation of motion was performed using a fourth-order Runge-

Kutta algorithm in a BASIC computer program called Hyperlon. The effects of resonance excitation were modeled and experimentally probed.

The effective energy of electrons injected into the quadrupole ion trap was studied theoretically and experimentally. The existence of low-energy electrons in the quadrupole ion trap was predicted and experimentally verified.

A novel quadrupole deflector ion injection system was used to couple a high-pressure chemical ionization ion source with a commercially available ion trap mass spectrometer. This ion injection system was studied experimentally and through SIMION simulations. Collection and detection efficiencies of the ion injection system were characterized, and nonlinear resonance effects attributed to hexapolar, octopolar, and higher order fields were studied.

The fundamental results presented in this dissertation offer potential for further improvements in the operation of the quadrupole ion trap mass spectrometer through a firm understanding of its operating principles.

CHAPTER 1
INTRODUCTION

The primary objective of the research reported in this dissertation was the characterization of the fundamental processes associated with the quadrupole ion trap. Basic theory, computer models, and experimental results were utilized to help characterize and explain experimental phenomena.

The basic theory of operation of the quadrupole ion trap mass spectrometer has been known for fourty years (1,2,3). However, a plethora of new modes of operation for the quadrupole ion trap has accompanied the recent commercial introduction of the ion trap (4). This work is an attempt to characterize some of these new operating modes from a fundamental standpoint, ultimately allowing for better experimental design through *a priori* prediction of optimal experimental parameters, rather than empirical variation of experimental conditions to optimize for a particular effect.

Organization of Dissertation

This dissertation is divided into six chapters. This first chapter provides background information useful for understanding the significance of the research presented in later chapters. The major milestones in quadrupole ion trap history are outlined, along with a summary of the operational modes which have been used with quadrupole ion trap mass spectrometers. Previous work in computer modeling of ion motion in quadrupole mass spectrometers is reviewed briefly.

In the second chapter, the fundamental theory of quadrupole ion trap operation is reviewed. A rigorous derivation of the Mathieu equation of motion for ions in a quadrupole ion trap is presented. Included is the derivation of the equation for the field perturbation due to the application of a supplementary alternating current (AC) voltage across the endcaps. The analytical solution of the Mathieu equation is reviewed, along with some methods for estimating the energetics of ion motion in the quadrupole ion trap. A new method for estimating ion energetics is derived from the analytical solution and is compared with more traditional methods. The Mathieu stability diagram (a plot of the solutions to the Mathieu equation) is discussed in detail. Some operational modes of the quadrupole ion trap are reviewed.

The third chapter introduces the computer simulation of ion motion in an ion trap via the BASIC computer program Hyperlon. In Hyperlon, the Mathieu equation of ion motion is solved using a numerical integration method (fourth-order Runge-Kutta), with graphical display of the calculated trajectory. A typical ion trajectory is seen to be periodic with time, with a variable instantaneous velocity. Some results of simulated resonance excitation experiments are described and analyzed with regard to the competition between resonance ejection and collision-induced dissociation. The method for calculating phase space diagrams is presented along with an analysis of ion injection through phase space diagrams.

In the fourth chapter, the results of simulation studies for the calculation of electron energy are presented. The average kinetic energy of electrons injected into the ion trap (electron energy) is calculated by numerical integration of the Mathieu equation. Electron energy is calculated as a function of the phase and amplitude of RF voltage applied to the ring electrode during electron injection. Laboratory results are presented which correlate effective electron energy to the trapping potential applied to the ring electrode. The presence of low-energy electrons from electron injection is predicted and experimentally verified.

The injection of ions into a quadrupole ion trap from an external ion source is modeled and characterized experimentally, with the results presented in Chapter 5. In this work, a novel off-axis ion optics system is used to couple a high-pressure chemical ionization source with a quadrupole ion trap. The ion optics simulation program, SIMION, was used to model various electrode configurations, with the most promising configuration constructed and used experimentally. Such experimental phenomena as the efficiency of collection of injected ions, the dependence of the quality of injected ion spectra upon the amplitude of the trapping voltages applied to the ring electrode, and the effects of injected ion kinetic energy on sensitivity and spectral quality are discussed.

Also included in Chapter five is a discussion of the effects of nonlinear resonances on mass spectral quality. Mechanical imperfections due to non-ideal hyperbolic electrode geometries result in third, fourth and sixth order field distortions. These field distortions manifest themselves as nonlinear resonances within the quadrupolar field, selectively exciting ions at certain frequencies, resulting in premature ion ejection. Nonlinear resonances of stored ions are especially apparent in ion injection experiments. This chapter includes experimental data demonstrating the occurrence of nonlinear resonances.

The sixth and final chapter summarizes the results of this work and presents some ideas for further developments of HyperIon computer simulations, as well as future work in the injection of ions from an external ion source into a quadrupole ion trap mass spectrometer.

Historical Development of the Quadrupole Ion Trap Mass Spectrometer

The quadrupole ion trap mass spectrometer is a mechanically simple device consisting of three electrically isolated, solid, stainless steel electrodes (see Figure 1-1). Traditionally, the electrodes are fashioned such that the electrode surfaces are hyperbolic, defined by the equation: $x^2 + y^2 = 2z^2$. The Finnigan ITMS electrode geometry deviates slightly from this ideal (5) with z_0 some ten percent larger than the theoretical value. This geometry is identified as the Finnigan stretched trap geometry in this dissertation. The electrodes are rotationally symmetric, with a toroidal shaped ring electrode sandwiched between two inverted domes. Radio frequency (RF) and direct current (DC) voltages are applied to these electrodes, creating an electrodynamic containment field within this bounded volume which is suitable for the storage of electrically charged particles or ions. Ions created within or injected into this volume may be stored indefinitely with stable periodic trajectories depending upon the trapping conditions and the mass-to-charge ratio (m/z) of the ion (2, 6, 7, 8). Ions stored in an ion trap can be detected by mass-selective ejection of those ions to an external detector or by measuring the image current induced at the electrodes by the ions as they orbit within the trap (2, 9).

The quadrupole ion trap was first proposed by Paul and Steinwedel of the University of Bonn, as another arrangement of electrodes (in addition to the quadrupole mass filter, a four-electrode arrangement of parallel rods) in which a quadrupolar field could be maintained (1). The landmark quadrupole ion trap publication contains

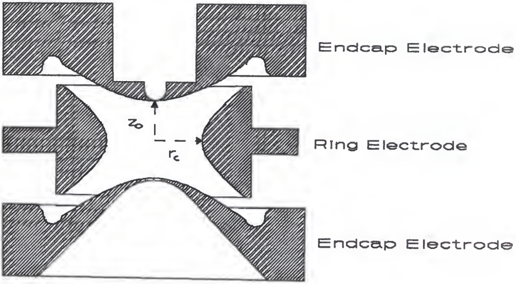

Figure 1-1: Schematic drawing of a quadrupole ion trap analyzer.

results from Fischer's doctoral research of the late 1950s at the University of Bonn (2). In this work Fischer presents a thorough introduction to Mathieu theory and the theory of ion motion for ions stored within a quadrupole ion trap. Fischer also discusses the operational mode in use at that time, namely a single-frequency Purcell-type resonance absorption technique with a combined RF and DC voltage trapping field. In this mode of operation, the energy absorbed by ions from a resonance circuit applied to the endcaps of the ion trap is measured and is related to the concentration of stored ions with that resonant frequency. For a variety of reasons, this scheme is no longer used.

Also published in the late 1950s was the work of Wuerker, Shelton, and Langmuir at the University of California, demonstrating the storage of small micro-particles of aluminum, with photographic detection of these particles (6). In this work, charged aluminum micro-particles stored in the electrodynamic field of the quadrupole ion trap were photographed with various storage fields strengths (applied RF and DC voltages). Such an apparatus was used as "an analogue computer of the Mathieu differential equation"(6, page 347). The frequency of ion motion was measured by application of a range of small supplemental alternating current (AC) frequencies across the endcaps of the ion trap, with visual determination of resonance of the stored particle(s) with the applied frequency. In addition, this publication demonstrates the crystallization of ion trajectories through collisional damping with a bath gas.

The work of Dawson and Whetten at General Electric in the late 1960s demonstrated the first use of the quadrupole ion trap as a mass spectrometer, with pulsed ionization followed by a brief storage period and pulsed ejection to an external electron multiplier (7, 10, 11). In this operational mode, mass selection is effected by suitable combinations of RF and DC voltages applied to the ion trap such that only one m/z is stable at a time. Ions are ejected by a short DC voltage pulse applied to one of the endcaps. This DC voltage pulse destabilizes the ion trajectory, extracting ions from the trap through holes drilled in the end-cap, to an electron multiplier. The authors observed that "a light gas can act to stabilize the motion of a heavier ion with which it cannot charge exchange." (11, page 110) This phenomenon was later utilized by workers at Finnigan MAT in their development of the mass-selective instability mode of ion trap operation (8).

After Dawson's introduction of the pulse-out ejection operational mode of the quadrupole ion trap, a number of other groups started experimenting with quadrupole ion traps as mass spectrometers. Two notable groups are those of John Todd at the University of Kent and Ray March at Trent University. These two closely related groups published a number of fundamental papers, often in collaboration, throughout the 1970s, 1980s and 1990s. The Todd research group demonstrated the use of the quadrupole ion trap as a low pressure chemical ionization source for a quadrupole mass filter (12, 13), as well as producing a number of excellent publications relating to fundamental aspects of ion storage and ion-ion interaction (14, 15, 16, 17, 18). The term QUISTOR (Quadrupole Ion STORe) was first coined by the Todd group (13), and is generally used to refer to a quadrupole ion trap operated using Dawson's pulse-out ejection technique.

The work of the March group has included the theory and application of cylindrical ion traps (19), and the use of the quadrupole ion trap as a selective ion reactor (20, 21). In this latter work, a timing sequence (scan function) of RF and DC voltages was used to effect selected ion storage of a narrow range of masses, with variable reaction times following isolation. Such methods were used to probe ion kinetics. Additional experiments included selective excitation of stored ions involved in a chemical reaction, resulting in altered ion kinetics. More recently the March group has published a monograph on quadrupole storage mass spectrometry (22), as well as a series of papers on computer simulation of ion motion in quadrupole ion traps (23, 24, 25).

The quadrupole ion trap mass spectrometer has recently surged in popularity as a result of its commercial introduction by Finnigan MAT in the form of a mass-selective gas chromatography (GC) detector, the Ion Trap Detector (ITD)(4, 8). In this system, ions are formed within the ion trap by the injection of electrons into the ion trap, resulting in ionization of neutral gas molecules through electron ionization (EI). After a brief storage period in which a range of masses is confined by the RF-only containment field, the RF voltage is ramped linearly, resulting in sequential ejection of ions from the ion trap to an external electron multiplier. These ions are ejected in order of increasing mass-to-charge ratio (m/z) to produce a mass spectrum. This RF-only operation of the quadrupole ion trap results in an enhanced duty cycle compared with that of Dawson's pulse-out ejection technique in which only a single m/z is observed for each ionization period.

More recently, enhanced capabilities have been added by Finnigan MAT to this mass spectrometer system, supplementing the basic capability of mass selective ejection/detection. Very narrow mass ranges can be isolated within the ion trap through the application of DC pulses of short duration in addition to the RF voltage applied to the ring electrode (26, 27, 28). Selected ions can be kinetically excited through the application of a supplementary AC voltage with frequency corresponding to the resonance frequency of the selected ion (29). This resonance excitation can result in collisionally induced dissociation (CID) when these kinetically excited ions are allowed to collide with neutral target molecules. Resonance excitation using very large amplitude voltages results in ion ejection(26), recently demonstrated by the Cooks group at Purdue University to improve mass resolution, while simultaneously extending the usable mass range of the quadrupole ion trap to significantly heavier ions (30). The Yost group at the University of Florida has demonstrated parent and neutral loss scans in the quadrupole ion trap through simultaneous or sequential application of voltages of multiple frequencies (31, 32). In addition, it has been shown that ions can be generated external to the ion trap, followed by injection into the trap, and subsequent mass analysis. (33, 34, 35, 36, 37, 38, 39)

As new ion trap operating modes are rapidly being proposed and implemented, their characterization is necessary for maximum utility of those modes. The multitude of interdependent parameters to be set in these ever-more complicated experiments requires expert knowledge of their interaction for optimal use. Once the interaction of various parameters is known, optimal experimental parameters can be predicted and tested under computer control, reducing the amount of effort required to set up a given experiment. Such computer-optimized experiments would require a large knowledge base of the operating theory for the various modes of ion trap operation to maximize their power. With the ever-increasing popularity of mass spectrometry, and the ever-increasing shortage of trained mass spectrometrists, it is clearly necessary to simplify the operation of such complex instruments to allow for their use with minimal training. The goal of this research was to probe the fundamentals of the quadrupole ion trap to understand and simplify its operation.

CHAPTER 2
THEORY OF QUADRUPOLE ION TRAP OPERATION

While a theoretical treatment of the operation of the quadrupole ion trap can be found in numerous papers and some books (3, 22), recently introduced operating modes such as MS/MS and axial modulation (both through resonance excitation) are not thoroughly considered in those works. In this chapter, the basic theory of operation of the quadrupole ion trap is introduced, and some basic operational modes of the quadrupole ion trap are presented. A rigorous derivation of the Mathieu equation is given, with modifications to describe resonance excitation. The equations for the analytical solution of the Mathieu equation are reviewed, and a new model for the estimation of ion kinetic energy is presented based on this analytical solution of the Mathieu equation. Velocities and kinetic energies calculated using this new model are compared to those calculated via numeric integration of the Mathieu equation, and to Dehmelt's pseudopotential well model and its derivatives.

The derivation of the equations describing the motion of an ion in a quadrupole ion trap mass spectrometer with hyperbolic fields has been demonstrated numerous times in the literature (3, 40). This chapter contains a derivation of the equations of motion for an ion in a quadrupole ion trap with both the standard RF and DC voltages applied to the ring electrode, and a supplementary AC resonance excitation voltage applied across the two endcaps, with the supplementary potential applied in opposing phases on opposing endcaps. Experimentally, such a field perturbation results in resonance excitation if the frequency of the supplementary AC field corresponds to the secular frequency of motion for a given ion. This derivation is limited in scope to the potential in the z direction (between the endcap electrodes); however, a similar derivation could be made for each of the x and y directions. This derivation was developed through combination of the derivations given in references 3 and 40.

The equation for dipolar excitation has been previously presented by Fischer (2), but erroneously transcribed on page 49 of Dawson's book (3). More recently, March et al. have presented a derivation of dipolar excitation (23). It is assumed here that the field contribution due to the supplementary AC potential applied in opposing phases across the endcap electrodes results in the electrical equivalent of a parallel plate capacitor. Since the endcap electrodes are hyperbolic in shape, rather than parallel plates, there will be some inherent error in calculations using the plate capacitor model. These errors should be presumed negligible for those cases where ions have minimal x or y components (i.e. ions damped to the radial center of the trap). Since in practice, ion detection requires that ions be stored near the center of the ion trap prior to ejection, this plate capacitor assumption is a reasonable approximation of the true field.

Another assumption in this derivation is that of ideal geometry of the electrodes. In the Finnigan stretched trap geometry with holes in the endcaps, higher order fields are present (hexapolar, octopolar, dodecapolar...); however, these higher order terms are neglected in this derivation. Scaling of the resonance excitation voltage to the stretched trap geometry, however, is inherent in the equation as derived.

Derivation of the Mathieu Equation

As mentioned in Chapter 1, the ideal quadrupole ion trap mass spectrometer consists of three electrically isolated, solid, stainless steel electrodes fashioned such that the electrode surfaces are hyperbolic (see Figure 2-1), defined by the equation:

$$x^2+y^2=2z^2 \tag{2.1}$$

When an electric field Φ_0 is applied between these three electrodes, the electric potential Φ at any point within this electrode structure is given by the equation:

$$\Phi=\frac{\Phi_0}{2}\cdot\left(\frac{x^2}{x_0^2}+\frac{y^2}{y_0^2}-\frac{z^2}{z_0^2}\right)+\frac{\Phi_0}{2} \tag{2.2}$$

where x_0, y_0, and z_0 correspond to the hyperbola radii of the electrode surface in the x, y and z directions respectively, and x, y, and z correspond to the coordinates of the point in question. This equation describes a quadrupolar field as shown in Figure 2-1.

An additional term can be added to this equation which corresponds to the supplementary AC resonance excitation potential applied across the endcaps (z direction only):

$$\Phi=\frac{\Phi_0}{2}\cdot\left(\frac{x^2}{x_0^2}+\frac{y^2}{y_0^2}-\frac{z^2}{z_0^2}\right)+\frac{\Phi_0}{2}+\Phi_t\cdot\left(\frac{z}{z_0}\right) \tag{2.3}$$

where Φ_t is the resonance excitation or "tickle" potential. This additional term describes a dipolar field as shown in Figure 2-2.

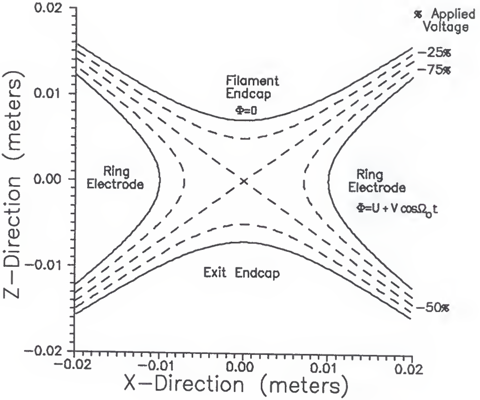

Figure 2-1: Equipotential contours for an ideal quadrupole ion trap. Quadrupolar field lines were calculated by solving equation 2.1.

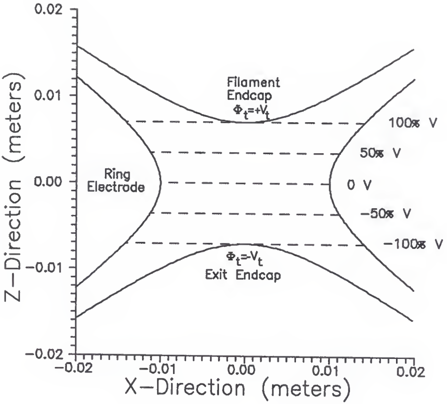

Figure 2-2: Dipolar equipotential contours plotted for a quadrupole ion trap. Note that the plate capacitor approximation is reasonable near the radial center of the ion trap but errs with significant radial distance.

Note that equation 2.3, is subject to, and satisfies the requirements of the LaPlace equation:

$$\nabla^2\Phi=\frac{\delta^2\Phi}{\delta x^2}+\frac{\delta^2\Phi}{\delta y^2}+\frac{\delta^2\Phi}{\delta z^2}=0 \tag{2.4}$$

where ∇ is the Del (partial differential) operator, and Φ is potential.

The force $\vec{F}$ exerted by an electric field on a positively charged particle is:

$$\vec{F}=m\cdot(\vec{acc})=-e\vec{\nabla}\Phi=-e(\frac{\delta\Phi}{\delta x}\vec{i}+\frac{\delta\Phi}{\delta y}\vec{j}+\frac{\delta\Phi}{\delta z}\vec{k})=F_x\vec{i}+F_y\vec{j}+F_z\vec{k} \tag{2.5}$$

where m is the mass of the charged particle, acc is the acceleration, e is the charge on an electron, Φ is the potential $\nabla\Phi$ is the electric field, and i, j, and k are the unit vectors in the x, y, and z directions.

Consider only the force in the z direction:

$$F_z=m\cdot(acc_z)=-e(\frac{\delta\Phi}{\delta z}) \tag{2.6}$$

Differentiate equation 2.3 with respect to z:

$$\frac{\delta\Phi}{\delta z}=\frac{\Phi_0}{2}\cdot(\frac{-2z}{z_0^2})+\Phi_1(\frac{1}{z_0}) \tag{2.7}$$

Substitute equation 2.7 into equation 2.6:

$$F_z=-e\frac{\delta\Phi}{\delta z}=\frac{e\Phi_0 z}{z_0^2}-\frac{e\Phi_t}{z_0} \qquad (2.8)$$

Let the applied ring electrode potential Φ_0 be defined as:

$$\Phi_0=U+V\cos\Omega_0 t \qquad (2.9)$$

where U is the applied DC potential, V the applied zero-to-peak RF potential, Ω_0 is the RF drive frequency, and t is time.

Let the supplementary AC resonance excitation (tickle) potential be defined as:

$$\Phi_t=V_t\cos\Omega_t t \qquad (2.10)$$

where V_t is the applied zero-to-peak resonance excitation potential, and Ω_t the resonance excitation frequency.

Substitute equations 2.9 and 2.10 into equation 2.7:

$$\frac{\delta\Phi}{\delta z}=\frac{z}{z_0^2}(U+V\cos\Omega_0 t)-\frac{1}{z_0}V_t\cos\Omega_t t \qquad (2.11)$$

and thus:

$$F_z=\frac{ez}{z_0^2}(U+V\cos\Omega_0 t)-\frac{e}{z_0}V_t\cos\Omega_t t \qquad (2.12)$$

From equation 2.6:

$$acc_z=\frac{F_z}{m} \tag{2.13}$$

Let:

$$acc_z=\frac{d^2z}{dt^2} \tag{2.14}$$

and combine equation 2.12, equation 2.13, and equation 2.14:

$$\frac{d^2z}{dt^2}=\frac{ez}{mz_0^2}(U+V\cos\Omega_0 t)-\frac{e}{mz_0}V_t\cos\Omega_t t \tag{2.15}$$

Let

$$\xi=\frac{\Omega_0 t}{2} \tag{2.16}$$

$$\frac{d}{dt}=\frac{d}{dt}\cdot\frac{d\xi}{d\xi}=\frac{d\xi}{dt}\cdot\frac{d}{d\xi} \tag{2.17}$$

From chain rule:

And:

$$\frac{d^2}{dt^2}=\frac{d}{dt}\cdot\left(\frac{d\xi}{dt}\cdot\frac{d}{d\xi}\right) \tag{2.18}$$

Expand:

$$\frac{d^2}{dt^2}=\frac{d^2\xi}{dt^2}\cdot\frac{d}{d\xi}+\frac{d\xi}{dt}\cdot\frac{d}{dt}\cdot\frac{d}{d\xi} \tag{2.19}$$

Substitute equation 2.17 into equation 2.19:

$$\frac{d^2}{dt^2}=\frac{d^2\xi}{dt^2}\cdot\frac{d}{d\xi}+\left(\frac{d\xi}{dt}\right)^2\cdot\frac{d^2}{d\xi^2} \tag{2.20}$$

Differentiate equation 2.16 with respect to time:

$$\frac{d\xi}{dt}=\frac{\Omega_0}{2} \tag{2.21}$$

Differentiate equation 2.21 with respect to time:

$$\frac{d^2\xi}{dt^2}=0 \tag{2.22}$$

Substitute equations 2.21 and 2.22 into equation 2.20:

$$\frac{d^2}{dt^2}=\frac{\Omega_0^2}{2^2}\cdot\frac{d^2}{d\xi^2}=\frac{\Omega_0^2}{4}\cdot\frac{d^2}{d\xi^2} \qquad (2.23)$$

Substitute equation 2.23 into equation 2.15:

$$\frac{\Omega_0^2}{4}\cdot\frac{d^2z}{d\xi^2}=\frac{e}{mz_0^2}(U+V\cos\Omega_0 t)z-\frac{e}{mz_0}V_t\cos\Omega_t t \qquad (2.24)$$

Rearrange:

$$\frac{d^2z}{d\xi^2}=\frac{4ez}{mz_0^2\Omega_0^2}(U+V\cos\Omega_0 t)-\frac{4e}{mz_0\Omega_0^2}V_t\cos\Omega_t t \qquad (2.25)$$

The canonical form of the Mathieu differential equation is:

$$\frac{d^2y}{dv^2}=-(a-2q\cos 2v)y \qquad (2.26)$$

To put equation 2.25 into a Mathieu-like format, use the following substitutions:

$$a_z=\frac{-4eU}{mz_0^2\Omega_0^2} \qquad (2.27)$$

$$q_z=\frac{2eV}{mz_0^2\Omega_0^2} \qquad (2.28)$$

$$b_z = \frac{-4eV_t}{mz_0\Omega_0^2} \qquad (2.29)$$

Since the Finnigan ITMS software (Rev B) uses peak-to-peak voltage notation for the excitation voltage, there is a factor of two reduction in the scaling of the b parameter since $V_{pp} = 2\ V_{0\text{-}p}$.

$$b_z = \frac{-2eV_{t,pp}}{mz_0\Omega_0^2} \qquad (2.30)$$

Substituting these parameters into equation 2.25:

$$\frac{d^2z}{d\xi^2} = -(a+2q\cos\Omega_0 t)z + b\cos\Omega_t t \qquad (2.31)$$

From equation 2.16,

$$\Omega_0 t = 2\xi \qquad (2.32)$$

Substituting equation 2.32 into equation 2.31,

$$\frac{d^2z}{d\xi^2} = -(a+2q\cos 2\xi)z + b\cos\Omega_t t \qquad (2.33)$$

Equation 2.33 represents the equation of motion in the z direction for an ion stored in an ideal quadrupole ion trap mass spectrometer. The b term of equation 2.33, defined in equation 2.30, corresponds to the force on an ion stored in a quadrupole ion trap due to a supplementary sinusoidal excitation voltage applied to the endcap electrodes with a phase differential of 180°.

A similar derivation may be applied in the x and y (or r) directions without the perturbation term, yielding:

$$a_r = \frac{4eU}{mr_0^2\Omega_0^2} \qquad (2.34)$$

$$q_r = \frac{-2eV}{mr_0^2\Omega_0^2} \qquad (2.35)$$

Now for an ideal quadrupole ion trap,

$$z_0 = \frac{r_0}{\sqrt{2}} \qquad (2.36)$$

and,

$$a_z = \frac{-8eU}{mr_0^2\Omega_0^2} \qquad (2.37)$$

$$q_z = \frac{4eV}{mr_0^2\Omega_0^2} \qquad (2.38)$$

For the Finnigan stretched trap geometry, in which the geometric relationship in equation 2.36 does not hold, a and q can be approximated by:(41)

$$a_z = \frac{-16eU}{m(r_0^2+2z_0^2)\Omega_0^2} \tag{2.39}$$

$$q_z = \frac{8eV}{m(r_0^2+2z_0^2)\Omega_0^2} \tag{2.40}$$

Analytical Solution of the Mathieu Equation

Equation 2.33 identifies the acceleration on an ion in the z direction due to applied electric fields. From this equation the equations for the calculation of velocity and position have been developed (42, 3, 22). Equation 2.41 identifies position (u) as a function of ξ for an ion in pure quadrupolar field, assuming zero initial velocity (22), with A a constant depending on initial conditions, and β a function of a and q, describing the frequency of ion motion.

$$u(\xi) = A\sum_{n=-\infty}^{\infty} C_{2n}\cos(2n+\beta)\xi \tag{2.41}$$

Expanding the first few terms surrounding n=0:

$$\begin{aligned} u(\xi) = A[&C_0\cos(\beta\xi) + C_{-2}\cos((\beta-2)\xi) + \\ &C_{+2}\cos((\beta+2)\xi) + C_{-4}\cos((\beta-4)\xi) + \ldots] \end{aligned} \tag{2.42}$$

Substituting for ξ, using equation 2.16,

$$u(t)=A[C_0\cos(\frac{\beta}{2}\Omega_0 t)+C_{-2}\cos((\frac{\beta}{2}-1)\Omega_0 t)+ \\ C_{+2}\cos((\frac{\beta}{2}+1)\Omega_0 t)+C_{-4}\cos((\frac{\beta}{2}-2)\Omega_0 t)+...] \qquad \textbf{(2.43)}$$

From this equation it is apparent that ion trajectories are a superposition of periodic motions with frequencies (ω_n) a function of β:

$$\omega_n=(\frac{\beta}{2}\pm n)\Omega_0 \quad \text{where} \quad n=0,\pm1,\pm2... \qquad \textbf{(2.44)}$$

Such periodic motion represents a superposition of simple harmonic oscillators, with instantaneous and maximum ion kinetic energy dependent upon initial conditions. Except for any energy imparted to an ion at formation, the trapping potential cannot directly impart a change in average kinetic energy for a stored ion. A change in the trajectory and average kinetic energy of an ion stored in a quadrupole ion trap requires either some change in the trapping potential or some supplemental force (i.e. resonance excitation or collision with a neutral molecule).

Calculation of β and Coefficients for Analytical Solution of Mathieu Equation

The calculation of the coefficients (C_{2n}) for the infinite summation in equation 2.41 has been presented in various forms in references 42, 3, and 22 (books by McLachlan, Dawson and March respectively). McLachlan's monograph gives the most detailed equation which includes enough terms for simple recognition of the sequence for the continued fraction. In each of the presentations cited, the ratio of sequential coefficients is calculated, requiring some scaling of the coefficients and normalization to yield the relative magnitudes of the various coefficients.

The equation given on page 72 of March's book (22) is as follows:

$$\frac{C_{2n}}{C_{2n-2}}=\frac{-q}{(2n+\beta)^2(1-\frac{a}{(2n+\beta)^2}-\frac{q^2}{(2n+\beta)^2(2n+2+\beta)^2(1-\ldots etc})} \qquad \textbf{(2.45)}$$

Expanding this equation to include more terms similar to the treatment shown on page 106 of McLachlan's monograph (42):

$$\frac{C_{2n}}{C_{2n-2}}=\frac{-q}{(2n+\beta)^2(1-\frac{a}{(2n+\beta)^2}-\text{Fraction1})} \qquad \textbf{(2.46)}$$

where Fraction1 is:

$$\text{Fraction1}=\frac{q^2}{(2n+\beta)^2(2n+2+\beta)^2(1-\frac{a}{(2n+2+\beta)^2}-\text{Fraction2})} \qquad \textbf{(2.47)}$$

Fraction2 is:

$$\text{Fraction2}=\frac{q^2}{(2n+2+\beta)^2(2n+4+\beta)^2(1-\frac{a}{(2n+4+\beta)^2}-\text{Fraction3})} \qquad \textbf{(2.48)}$$

Fraction3 is:

$$\text{Fraction3}=\frac{q^2}{(2n+4+\beta)^2(2n+6+\beta)^2(1-\frac{a}{(2n+6+\beta)^2}-\text{Fraction4})} \tag{2.49}$$

and so on...

McLachlan's monograph also presents an alternative continued fraction to calculate the ratio of sequential coefficients on page 106 of reference 42:

$$\frac{C_{2n}}{C_{2n-2}}=\frac{-(2n-2+\beta)^2+a}{q}+\frac{q}{(2n-4+\beta)^2(1-\frac{a}{(2n-4+\beta)^2}-\text{Fraction1a})} \tag{2.50}$$

where Fraction1a is:

$$\text{Fraction1a}=\frac{q^2}{(2n-4+\beta)^2(2n-6+\beta)^2(1-\frac{a}{(2n-6+\beta)^2}-\text{Fraction2a})} \tag{2.51}$$

Fraction2a is:

$$\text{Fraction2a}=\frac{q^2}{(2n-6+\beta)^2(2n-8+\beta)^2(1-\frac{a}{(2n-8+\beta)^2}-\text{Fraction3a})} \tag{2.52}$$

Fraction3a is:

$$\text{Fraction3a}=\frac{q^2}{(2n-8+\beta)^2(2n-10+\beta)^2\left(1-\frac{a}{(2n-10+\beta)^2}-\text{Fraction4a}\right)} \qquad \textbf{(2.53)}$$

and so on...

These two alternative equations yield identical results with accurate selection of β (42). Solving these two equations simultaneously would yield an exact value of β for a given value of a and q (for simplicity, n is chosen to equal one, resulting in the calculation of C_2/C_0). Unfortunately, these equations are too complicated for the identification of a simple relationship between a, q and β. The calculation of β using these equations is typically effected through successive approximation. One simply approximates (guesses) a value for β, and solves each of equations 2.46 and 2.50 for the ratio of a pair of coefficients. If an exact value of β is chosen, then the results from these two equations will be equal. If not, then a new value of β is guessed based on the difference between the two ratio results. Such an algorithm is tedious to perform by hand, but is readily implemented into a computer program. A simple BASIC computer program (Analytic) which uses this algorithm is given in Appendix A.

Calculated Coefficients for the Analytical Solution

A BASIC computer program ANALYTIC.BAS was developed, which, when given the a-q coordinates as inputs, calculates β, the relative amplitudes of the coefficients (C_{2n}) of the analytical solution of the Mathieu equation, frequencies of ion motion, maximum velocity, and maximum kinetic energy for a given coordinate of ion motion (x, y, or z).

The algorithm used in ANALYTIC.BAS can be summarized as follows. First, β is calculated for a given set of a and q values through successive approximation via equations 2.46 and 2.50. The values for a number of ratios of sequential coefficients are calculated by solving equation 2.46 through substitution of a, q, β and n. The unnormalized coefficient C_0 is defined as one. Using the ratios calculated using equation 2.46, the other coefficients are calculated relative to C_0. These coefficients are then normalized such that their sum equals 100%. Attempts to use equation 2.50 in a similar fashion proved unsuccessful; however, the absolute magnitude of the ratio corresponding to n=1 was identical with that calculated using equation 2.46. Thus equation 2.50 was used in combination with 2.46 to calculate β with n=1. The algorithm for the calculation of ion velocities and kinetic energies is presented in a later section of this chapter.

Figure 2-3 shows the relationship between the absolute value of the coefficients (C_n) of the first four terms of equation 2.41 and the Mathieu parameter q for RF-only operation (a=0). Figure 2-4 shows these same coefficients plotted as a function of β. It is apparent in these figures that the amplitudes of the two terms of the expanded equation 2.42 dominate ion motion, with the third and fourth terms accounting for less than ten percent of the total amplitude of ion motion. Absolute values of these amplitudes are plotted in Figures 2-3 and 2-4 in order to aid visualization of the relative magnitudes of the coefficients.

When the amplitudes (C_{2n}) calculated using Analytic program are plotted as a function of frequency (ω_n) of ion motion as calculated using equation 2.44, an

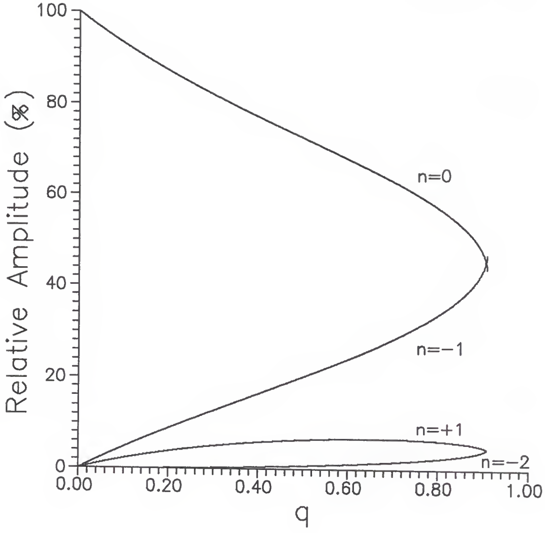

Figure 2-3: Relative amplitudes of coefficients (C_{2n} from equation 2.42) plotted as a function of the Mathieu parameter q for RF-only operation of the quadrupole ion trap.

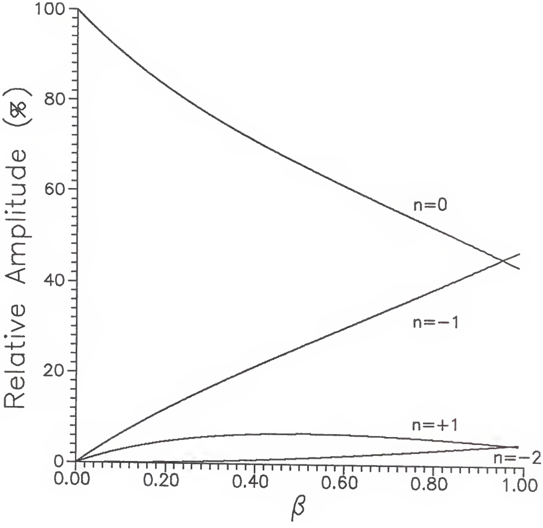

Figure 2-4: Relative amplitudes of coefficients (C_{2n} from equation 2.42) plotted as a function of β for RF-only operation of the quadrupole ion trap.

interesting pattern emerges, as shown in Figure 2-5. Note that absolute values of these frequencies are plotted for ease of visualization; a negative value of frequency merely indicates phase information. Boundaries between frequency regions are indicated by vertical dotted lines. There are gross discontinuities evident in this plot corresponding to integral multiples of the RF drive frequency. There are also subtle discontinuities corresponding to half-integer multiplies of the RF drive frequency. These data are plotted on a logarithmic scale to allow for the display of a wide dynamic range of relative amplitudes. The magnitudes of the relative amplitudes are seen to rapidly diminish with increase in frequency, indicating that truncation of equation 2.42 to four terms would represent greater than 99.5% of the amplitude of ion motion, truncation to six terms would represent greater than 99.99% of the amplitude of ion motion, and truncation to eight terms would represent greater than 99.9999% of the amplitude of ion motion.

Figure 2-6 shows the relative amplitudes of the first four coefficients plotted as a function of frequency of ion motion with a linear y axis. This plot also includes a number of data points which were calculated via numerical integration of the Mathieu equation by the program Hyperlon (details presented in the next chapter). The conditions for numerical integration were as follows: arbitrary position near the center of the quadrupole ion trap, initial velocities corresponding to thermal energy, phase increment and sample frequency eight times per RF cycle (four-times oversampling for the frequency range shown). For each value of the Mathieu parameter q (thus parametrically defining mass, RF frequency and quadrupole radius) a set of 4096 data points was saved to a file, imported into MathCAD (Mathsoft Corp., Cambridge, Massachusetts), apodized via multiplication of the array by π radians of a sine function,

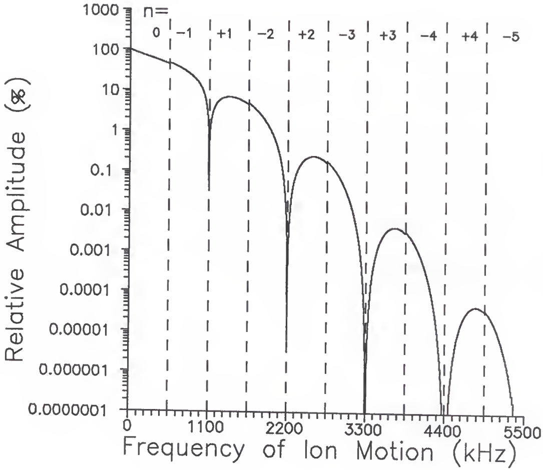

Figure 2-5: Relative amplitudes (C_{2n}) as a function of resonant frequencies ($\omega_n/2\pi$) for various values of q. Frequency ranges of fundamental (n=0) and first nine harmonic frequencies (n=+-1 to +-5) are indicated.

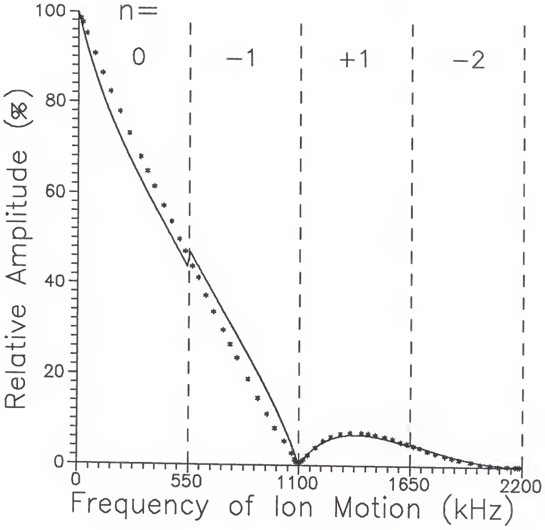

Figure 2-6: Relative amplitudes (C_{2n}) as a function of frequency (ω_n). Frequency ranges of the fundamental and three harmonics (n= 0, -1, +1, -2) are indicated. Additional data points were calculated using Hyperlon.

and a fast Fourier transform algorithm was applied to the apodized data set. The intensity of the first four peaks of the power spectrum were summed and normalized with the resulting normalized coefficients plotted as data points in Figure 2-6. The normalized coefficients calculated through the Runge-Kutta numerical integration are predicted to be slightly larger than those calculated through analytical theory due to the neglect of amplitudes of the higher order frequencies.

The relative magnitudes of these coefficients calculated via two distinct methods appear to track each other nicely; however, there are subtle discontinuities in the analytical solution data circa $\Omega_0/2$ and $3\Omega_0/2$ (550 and 1650 kHz). These discontinuities are not apparent in the numerical integration data, and the cause for this discrepancy is unknown. The following sections detail the utility of knowledge of these relative amplitudes in calculating velocity and kinetic energy for ions stored in the quadrupole ion trap.

Calculation of Ion Velocity and Ion Kinetic Energy

The most commonly cited method of estimating the kinetic energy of an ion stored in a quadrupole ion trap is via the pseudopotential well method originally proposed by Major and Dehmelt (43), and later supplemented by Todd et al. (44). Inherent in this model is the critical assumption that the trajectory of an ion stored in a quadrupole ion trap can be reduced to a single secular frequency. Thorough analysis of the variations of this model presented in the literature, along with an analysis of the analytical solution of ion motion, reveals that this pseudopotential well model underestimates the ion velocities by a factor of three, with resultant underestimation of ion kinetic energies by approximately a factor of ten for $q<0.4$, the stated limit of accuracy of the model. This section of the chapter contains a summary of the development of the pseudopotential well model, followed by a new method for estimating the kinetic energies of an ion stored in the quadrupole ion trap.

Pseudopotential Well Method for Calculation of Ion Velocity and Ion Kinetic Energy

In a landmark paper, Wuerker et al. presented photographs of aluminum microparticles stored in a quadrupole ion trap (6). In this work, the authors cited their use of a quadrupole ion trap as an analog calculator of solutions to the Mathieu equation. The work contains some striking photographs of ion trajectories of single ions which have been reproduced and included in numerous reviews of ion trap theory. Unfortunately, this landmark paper contains an erroneous and often-cited statement on page 346, describing Figure 5 of that paper: "It will be noted that the trajectory is a 2:1 Lissajous pattern upon which is superimposed the driving frequency." This statement erroneously attributes the low amplitude harmonic oscillations (ω_{-1} ω_{+1}...) of ion motion predicted by analytical theory to superposition of the RF drive frequency. Since for low values of q, ($q<0.3$), with no DC voltage, these first two harmonic frequencies are both quite similar in frequency to that of the RF drive, it is quite understandable that these trajectory ripples be erroneously attributed to the RF frequency. The conditions cited in the Wuerker paper were modeled using Hyperlon, and those results are presented in Chapter 3.

In another landmark paper (43), Major and Dehmelt presented a three term truncation of the analytical solution of the Mathieu equation (i.e. equation 2.41), and developed a model for the maximum kinetic energy for an ion stored in a quadrupole ion trap. In their derivations, they made some crude approximations of the relative amplitudes (i.e. C_{-1} and C_{+1} can be approximated by $q/4C_0$), and concluded that for low values of q, the energetics of ion motion is dominated by the fundamental frequency ω_0, which they approximated from:

$$\omega_0^2=\frac{1}{4}(a+\frac{q^2}{2})\Omega^2 \tag{2.54}$$

Thus, in this work, they acknowledged that there is ion motion at other frequencies, but neglect the contribution of these low amplitude oscillations to ion energy.

The work of Todd et al. in Chapter 8 of Quadrupole Mass Spectrometry and its Applications (44) provides an elegant development of the pseudopotential well equation which is based on the work of Wuerker et al. and Major and Dehmelt. It appears as if their development of the equation for the calculation of pseudopotential well depth is based on the assumption that the low amplitude high frequency ripple which is overlaid on the large amplitude secular frequency can be neglected as RF ripple (6). The following derivation is adapted from reference 44 wherein ion motion is reduced to simple harmonic motion:

$$\frac{d^2Z}{dt^2}=-\omega_0^2Z \tag{2.55}$$

where Z is the displacement from the center of the ion trap.

Substituting n=1 into equation 2.44,

$$\omega_0=\frac{\beta}{2}\Omega_0 \tag{2.56}$$

Wuerker et al. (6) demonstrated that the following approximation holds to within 1% for q<0.4:

$$\beta_z=(a_z+\frac{q_z^2}{2})^{\frac{1}{2}} \tag{2.57}$$

Substituting equation 2.28 and 2.56 into 2.57, for the case of $a_z=0$:

$$\omega_0=\frac{\sqrt{2}eV}{2mz_0^2\Omega_0} \tag{2.58}$$

Substituting equation 2.58 into equation 2.55:

$$\frac{d^2Z}{dt^2}=(\frac{e^2V^2}{2m^2z_0^4\Omega_0^2})Z \tag{2.59}$$

The force on an ion of mass m and charge e is therefore:

$$m\frac{d^2Z}{dt^2}=-e\frac{dD_z}{dZ} \tag{2.60}$$

thus

$$\frac{dD_z}{dZ}=\frac{eV^2}{2mz_0^4\Omega_0^2} \tag{2.61}$$

Integrating equation 2.61 between the limits of Z=0 and Z=z_0 gives:

$$D_Z = \frac{eV^2}{4mz_0^2\Omega_0^2} \qquad (2.62)$$

Through equation 2.28, this equation can be rearranged to:

$$D_Z = \frac{q_z V}{8} \qquad (2.63)$$

By a similar fashion D_r can be derived to equal 2 D_z.

Equation 2.63 is elegant in its simplicity, based completely on easily determined quantities (q and RF voltage); however, one must consider the validity of the assumptions asserted in the derivation of the equation, namely the neglect of the contributions of harmonic frequencies to ion motion.

A similar approach is detailed in Chapter 2 of March and Hughes' book on quadrupole ion trap mass spectrometry (22), attributed to Bonner as the smoothed general solution method. In this approach, the assumption is made that for low values of q, the harmonic frequencies contribute little to ion energy and can therefore be neglected. Simplifying equation 2.46 to include a single term with C_0 set to unity:

$$u(t) = A\cos\left(\frac{\beta}{2}\Omega_0 t\right) \qquad (2.64)$$

Differentiating with respect to time t, yielding velocity $\dot{u}(t)$:

$$\dot{u}(t)=-A\frac{\beta\Omega_0}{2}\sin(\frac{\beta\Omega_0 t}{2}) \qquad (2.65)$$

The maximum velocity would thus be the case where the sine function is unity:

$$\dot{u}(t)=-A\frac{\beta\Omega_0}{2} \qquad (2.66)$$

The application of these equations to the quadrupole ion trap requires one to identify the magnitude of A, the amplitude of oscillation. In this simple case, the amplitude A is taken as the radius (in meters) in the direction of the ion motion for calculation of maximum velocity. The units of frequency for Ω_0 are radians-per-second; this frequency must be divided by 2π to convert to Hertz for the results of equation 2.66 to have units of meters-per-second. The smoothed general solution model of Bonner is virtually identical to Dehmelt's pseudopotential well model, with the exception that the smoothed general solution model does not necessarily approximate β using equation 2.57. Maximum kinetic energy can be calculated from the smoothed general solution model using the familiar equation:

$$E=\frac{1}{2}m\dot{u}^2 \qquad (2.67)$$

Expanded Analytical Solution Method for Calculation of Ion Velocity and Kinetic Energy

The key assumption in the methods reviewed in the previous section was evaluated, namely the assumption that ion motion at harmonic frequencies may be neglected in the calculation of ion kinetic energy. Derivation of the equation which describes ion velocity can be performed in a similar fashion to the derivation of Bonner's smoothed general solution, only with the analytical solution expanded to include more terms. Differentiation of equation 2.43 with respect to time results in the following equation:

$$\begin{aligned}\dot{u}(t) = -A\Big(&C_0\frac{\beta\Omega_0}{2}\sin\left(\frac{\beta\Omega_0 t}{2}\right) + C_{-2}\left(\frac{\beta}{2}-1\right)\Omega_0\sin\left(\left(\frac{\beta}{2}-1\right)\Omega_0 t\right) + \\ &C_{+2}\left(\frac{\beta}{2}+1\right)\Omega_0\sin\left(\left(\frac{\beta}{2}+1\right)\Omega_0 t\right) + \\ &C_{-4}\left(\frac{\beta}{2}-2\right)\Omega_0\sin\left(\left(\frac{\beta}{2}-2\right)\Omega_0 t\right) + \ldots\Big)\end{aligned} \tag{2.68}$$

With maximum velocity:

$$\begin{aligned}\dot{u}(t)_{max} = A\Big(&\left|C_0\frac{\beta\Omega_0}{2}\right| + \left|C_{-2}\left(\frac{\beta}{2}-1\right)\Omega_0\right| + \left|C_{+2}\left(\frac{\beta}{2}+1\right)\Omega_0\right| + \\ &\left|C_{-4}\left(\frac{\beta}{2}-2\right)\Omega_0\right| + \ldots\Big)\end{aligned} \tag{2.69}$$

Substituting using equation 2.44:

$$\dot{u}(t)_{max} = -A\left(|C_0\omega_0| + |C_{-2}\omega_{-1}| + |C_{+2}\omega_{+1}| + |C_{-4}\omega_{-2}| + \ldots\right) \tag{2.70}$$

Again, the amplitude A can be taken from the radius of the electrode surface. Average velocities can be calculated using the relationship given in equation 2.69.

The coefficients (C_{2n}) must be normalized to unity before any physically meaningful calculations can be made. This model includes an inherent assumption that there exists some time t such that all of the position cosine terms in equation 2.46 are in phase with each other at a phase angle of 0°, resulting in the sum of the coefficients (C_{2n}) scaled by cosine terms equalling 100%. This assumption is true so long as the frequencies are distinct.

When calculations were made to compare this model with the Bonner smoothed general solution model and the Dehmelt pseudopotential well model, an astonishing observation was made: the velocity of an ion due to low amplitude oscillations at high frequency harmonics exceeds the contribution of the large amplitude low frequency secular motion for RF-only operation of the ion trap!

Tables 2-1, 2-2, 2-3, 2-4, and 2-5 summarize the results from a series of calculations of ion energetics for an ion stored in a quadrupole ion trap. These tables are the output from the aforementioned BASIC program Analytic, which is listed in Appendix A. The parameters used in these calculations can be summarized as follows: amplitude A was taken as z_0 for the Finnigan stretched trap geometry: 0.007825 meters; RF drive frequency (Ω_0) was taken as 1.1 MHz as per the Finnigan ITMS, RF-only operation of the quadrupole ion trap was assumed ($a_0 = 0$). A table of q values was loaded sequentially, with β and the coefficients calculated as described in a previous section of this chapter. Table 2-1 consists of a listing of the relative amplitudes of the coefficients from equation 2.41 for the fundamental and first eight harmonics (as plotted in Figures 2-3, 2-4, and 2-5. At very low values of q and β (<0.1) the amplitude of ion motion at the fundamental (C_0) is indeed much larger than the amplitude at the higher harmonics (C_{2n}). However, at higher values of q, the relative amplitudes of the higher harmonics (C_{2n}) increase dramatically relative to the fundamental (C_0). Except for values of β near unity, the magnitudes of the coefficients follow the trend: $C_0 > C_{-2} > C_{+2} > C_{-4} > C_{+4} > \ldots$

Table 2-2 consists of a listing of the frequencies of ion motion as calculated using equation 2.44. Note that a negative sign on a frequency simply indicates phase information. It may be noted from the information given in this table that the approximation given by Wuerker et al. (equation 2-57) indeed holds true for low values of q (q<0.3) but fails appreciably at higher values of q.

Table 2-3 contains a list of the velocity terms from equation 2.74. These velocity terms were calculated by scaling the absolute value of the relative coefficients from Table 2-1 by the absolute value of their corresponding frequencies given in Table 2-2, scaled by the maximum amplitude of oscillation (A=0.007825 meters). The resulting product was divided by 2π to convert units from radians-per-second to Hertz, resulting in units of velocity of meters/second. Columns 3 to 8 of Table 2-3 are plotted as a function of β in Figure 2-7. It is clear from this figure that the second velocity term ($C_{-2}\omega_{-1}$) of equation 2.70 is larger than the first velocity term ($C_0\omega_0$), which clearly contradicts the critical assumption of Dehmelt, Bonner, et al.

Although the relative amplitude of the fundamental frequency (C_0) is almost always larger than the amplitude of the first harmonic (C_{-2}), it is the product of the amplitude and frequency which determines the velocity. Thus the velocity contribution of the first harmonic is always larger than the velocity contribution of the fundamental frequency. While the relative amplitude of ion motion at the fundamental frequency dominates changes in position, especially at low values of q, ion motion at the fundamental frequency represents little more than one third of the total velocity of ion

Table 2-1: Normalized coefficients ($|C_{2n}|$) in percent, from equation 2.41, calculated through solution of equation 2.45. These values were calculated using the BASIC program Analytic which is reproduced in Appendix A.

q	C_0	C_{-2}	C_{+2}	C_{-4}	C_{+4}	C_{-6}	C_{+6}	C_{-8}	C_{+6}
0.0001	99.9925008	0.0049996	0.0024996	0.0000000	0.0000000	0.0000000	0.0000000	0.0000000	0.0000000
0.0010	99.9250699	0.0499619	0.0249636	0.0000031	0.0000016	0.0000000	0.0000000	0.0000000	0.0000000
0.0050	99.6267233	0.2490657	0.1240943	0.0000780	0.0000387	0.0000000	0.0000000	0.0000000	0.0000000
0.0100	99.2568420	0.4962964	0.2463967	0.0003113	0.0001535	0.0000001	0.0000000	0.0000000	0.0000000
0.0500	96.4125093	2.4125954	1.1636323	0.0076745	0.0035729	0.0000108	0.0000049	0.0000000	0.0000000
0.1000	93.1117360	4.6735244	2.1712433	0.0302724	0.0131020	0.0000861	0.0000356	0.0000001	0.0000001
0.2000	87.1814372	8.8559524	3.7983789	0.1190313	0.0442686	0.0006939	0.0002347	0.0000022	0.0000007
0.3000	81.9030185	12.7390298	5.0035329	0.2669059	0.0844489	0.0023935	0.0006557	0.0000119	0.0000029
0.4000	77.0456768	16.4762595	5.8640810	0.4794572	0.1273048	0.0058873	0.0012861	0.0000396	0.0000075
0.5000	72.4105933	20.2123130	6.4263110	0.7684782	0.1679795	0.0121378	0.0020676	0.0001043	0.0000147
0.6000	67.7889946	24.1168971	6.7100971	1.1560081	0.2022171	0.0226156	0.0029056	0.0002388	0.0000243
0.7000	62.8902756	28.4514916	6.7030362	1.6856949	0.2253812	0.0399133	0.0036631	0.0005051	0.0000350
0.7500	60.1771970	30.9324652	6.5704058	2.0317665	0.2307811	0.0526642	0.0039485	0.0007254	0.0000398
0.8000	57.1062048	33.8009614	6.3222853	2.4653092	0.2301259	0.0698982	0.0041157	0.0010459	0.0000436
0.8500	53.3109330	37.4196662	5.8954696	3.0532596	0.2200193	0.0949687	0.0040775	0.0015453	0.0000450
0.8750	50.7986961	39.8509508	5.5557868	3.4667275	0.2085103	0.1134217	0.0039128	0.0019297	0.0000439
0.9000	46.9249444	43.6427909	4.9704728	4.1268408	0.1851868	0.1436356	0.0034856	0.0025752	0.0000395
0.9025	46.2888951	44.2695432	4.8693537	4.2364875	0.1808809	0.1486873	0.0034001	0.0026839	0.0000385
0.9050	45.4883435	45.0598726	4.7406767	4.3745645	0.1753218	0.1550438	0.0032879	0.0028205	0.0000372
0.9075	44.2105217	46.3246396	4.5327081	4.5946013	0.1661858	0.1651377	0.0030998	0.0030368	0.0000349
0.9080	43.6820043	46.8488891	4.4459860	4.6852977	0.1623324	0.1692769	0.0030195	0.0031250	0.0000339

Table 2-2: Frequencies of ion motion ($\omega_0/2\pi$) in kilohertz for various values of q and β as calculated using equation 2.44, with $\Omega_0/2\pi$ taken as 1.1 MHz. Negative signs represent phase information.

q	β	ω_0	ω_{-1}	ω_{+1}	ω_{-2}	ω_{+2}	ω_{-3}	ω_{+3}	ω_{-4}	ω_{+4}
0.0001	0.000071	0.039	-1100	+1100	-2200	+2200	-3300	+3300	-4400	+4400
0.0010	0.000707	0.389	-1100	+1100	-2200	+2200	-3300	+3300	-4400	+4400
0.0050	0.003536	1.945	-1098	+1102	-2198	+2202	-3298	+3302	-4398	+4402
0.0100	0.007071	3.889	-1096	+1104	-2196	+2204	-3296	+3304	-4396	+4404
0.0500	0.035372	19.455	-1081	+1119	-2181	+2219	-3281	+3319	-4381	+4419
0.1000	0.070847	38.966	-1061	+1139	-2161	+2239	-3261	+3339	-4361	+4439
0.2000	0.142535	78.394	-1022	+1178	-2122	+2278	-3222	+3378	-4322	+4478
0.3000	0.216012	118.807	-981	+1219	-2081	+2319	-3181	+3419	-4281	+4519
0.4000	0.292473	160.860	-939	+1261	-2039	+2361	-3139	+3461	-4239	+4561
0.5000	0.373587	205.473	-895	+1305	-1995	+2405	-3095	+3505	-4195	+4605
0.6000	0.462016	254.109	-846	+1354	-1946	+2454	-3046	+3554	-4146	+4654
0.7000	0.562743	309.508	-790	+1410	-1890	+2510	-2990	+3610	-4090	+4710
0.7500	0.620900	341.495	-759	+1441	-1859	+2541	-2959	+3641	-4059	+4741
0.8000	0.688126	378.469	-722	+1478	-1822	+2578	-2922	+3678	-4022	+4778
0.8500	0.772416	424.829	-675	+1525	-1775	+2625	-2875	+3725	-3975	+4825
0.8750	0.828509	455.680	-644	+1556	-1744	+2656	-2844	+3756	-3944	+4856
0.9000	0.914904	503.197	-597	+1603	-1697	+2703	-2797	+3803	-3897	+4903
0.9025	0.929047	510.976	-589	+1611	-1689	+2711	-2789	+3811	-3889	+4911
0.9050	0.946824	520.753	-579	+1621	-1679	+2721	-2779	+3821	-3879	+4921
0.9075	0.975139	536.326	-564	+1636	-1664	+2736	-2764	+3836	-3864	+4936
0.9080	0.986828	542.755	-557	+1643	-1657	+2743	-2757	+3843	-3857	+4943

Table 2-3: Scaled velocity terms ($A|C_{2n}\omega_n|$) with A taken as z radius for stretched ion trap (A=0.007825 m). C_{2n} and ω_n taken from Tables 2-1 and 2-2. All velocities are in meters/second.

q	β	$AC_0\omega_0$	$AC_{-2}\omega_{-1}$	$AC_{+2}\omega_{+1}$	$AC_{-4}\omega_{-2}$	$AC_{+4}\omega_{+2}$	$AC_{-6}\omega_{-3}$	$AC_{+6}\omega_{+3}$	$AC_{-8}\omega_{-4}$	$AC_{+8}\omega_{+4}$
0.0001	0.000071	2	3	1	0	0	0	0	0	0
0.0010	0.000707	19	27	14	0	0	0	0	0	0
0.0050	0.003536	95	134	67	0	0	0	0	0	0
0.0100	0.007071	190	267	134	0	0	0	0	0	0
0.0500	0.035372	922	1282	640	8	4	0	0	0	0
0.1000	0.070847	1784	2438	1216	32	14	0	0	0	0
0.2000	0.142535	3360	4448	2201	124	50	1	0	0	0
0.3000	0.216012	4784	6145	2998	273	96	4	1	0	0
0.4000	0.292473	6093	7608	3635	481	148	9	2	0	0
0.5000	0.373587	7315	8889	4125	754	199	18	4	0	0
0.6000	0.462016	8469	10030	4467	1106	244	34	5	0	0
0.7000	0.562743	9570	11058	4645	1567	278	59	7	1	0
0.7500	0.620900	10104	11536	4657	1857	288	77	7	1	0
0.8000	0.688126	10626	11991	4596	2208	292	100	7	2	0
0.8500	0.772416	11135	12422	4420	2665	284	134	7	3	0
0.8750	0.828509	11381	12624	4249	2973	272	159	7	4	0
0.9000	0.914904	11609	12806	3918	3443	246	198	7	5	0
0.9025	0.929047	11629	12820	3857	3518	241	204	6	5	0
0.9050	0.946824	11647	12833	3778	3612	235	212	6	5	0
0.9075	0.975139	11658	12838	3647	3758	224	224	6	6	0
0.9080	0.986828	11657	12835	3591	3818	219	229	6	6	0

Table 2-4: Maximum ion velocities in the z direction calculated via various methods. All velocities are in meters/second. See text for details.

q	β	Hyperlon Numerical Integration	$A\Sigma C_{2n}\omega_n$ Expanded Analytical Solution Model	$A\beta\Omega_0/2$ Exact Fundamental Frequency Model	$Aq\Omega_0/2\sqrt{2}$ Estimated Fundamental Frequency Model
0.0001	0.000071	6.620	5.968	1.912	1.912
0.0010	0.000707	66.186	59.683	19.121	19.121
0.0050	0.003536	330.27	297.07	95.605	95.605
0.0100	0.007071	658.92	591.48	191.21	191.21
0.0500	0.035372	3231.8	2856.5	956.51	956.05
0.1000	0.070847	6321.1	5484.5	1915.8	1912.1
0.2000	0.142535	12097	10184	3854.3	3824.2
0.3000	0.216012	17484	14302	5841.2	5736.3
0.4000	0.292473	22520	17976	7908.8	7648.4
0.5000	0.373587	27444	21304	10102	9560.5
0.6000	0.462016	31746	24356	12493	11473
0.7000	0.562743	36188	27184	15217	13385
0.7500	0.620900	38319	28526	16789	14341
0.8000	0.688126	40272	29822	18607	15297
0.8500	0.772416	42220	31070	20887	16253
0.8750	0.828509	43364	31670	22403	16731
0.9000	0.914904	44158	32231	24740	17209
0.9025	0.929047	44369	32281	25122	17257
0.9050	0.946824	44384	32327	25603	17305
0.9075	0.975139	44426	32361	26368	17353
0.9080	0.986828	44444	32361	26685	17362

Table 2-5: Maximum ion kinetic energies for m/z 134 calculated via various methods. All kinetic energies are in units of eV. Ring RF Voltage is included for comparison. See text for details.

q	β	HyperIon Numerical Integration	$m(A\Sigma)^2/2$ Expanded Analytical Solution Model	$m(A\beta\Omega_0/2)^2/2$ Exact Fundamental Frequency Model	$m(Aq\Omega_0/2\sqrt{2})^2/2$ Estimated Fundamental Frequency Model	$qV/8$ Dehmelt Model	$V_{0\text{-}p}$ Ring RF Voltage
0.0001	0.000071	0.00003	0.00002	0.00000	0.00000	0.00000	0.18449
0.0010	0.000707	0.00304	0.00247	0.00025	0.00025	0.00023	1.8449
0.0050	0.003536	0.07575	0.06129	0.00635	0.00635	0.00577	9.2246
0.0100	0.007071	0.30152	0.24296	0.02539	0.02539	0.02306	18.449
0.0500	0.035372	7.2533	5.6666	0.63537	0.63477	0.57654	92.246
0.1000	0.070847	27.748	20.889	2.5489	2.5391	2.3061	184.49
0.2000	0.142535	101.63	72.030	10.317	10.156	9.2246	368.98
0.3000	0.216012	212.30	142.06	23.695	22.852	20.755	553.47
0.4000	0.292473	352.19	224.41	43.439	40.625	36.898	737.96
0.5000	0.373587	523.08	315.18	70.874	63.477	57.654	922.46
0.6000	0.462016	699.90	411.97	108.40	91.407	83.021	1106.9
0.7000	0.562743	909.45	513.20	160.81	124.41	113.00	1291.4
0.7500	0.620900	1019.7	565.10	195.77	142.82	129.72	1383.7
0.8000	0.688126	1126.3	617.63	240.46	162.50	147.59	1475.9
0.8500	0.772416	1238.0	670.41	302.98	183.45	166.62	1568.2
0.8750	0.828509	1305.9	696.53	348.58	194.40	176.56	1614.3
0.9000	0.914904	1354.2	721.44	425.07	205.66	186.80	1660.4
0.9025	0.929047	1367.1	723.67	438.31	206.81	187.84	1665.0
0.9050	0.946824	1368.1	725.73	455.24	207.96	188.88	1669.6
0.9075	0.975139	1370.7	727.25	482.88	209.11	189.92	1674.3
0.9080	0.986828	1371.8	727.25	494.52	209.34	190.13	1675.2

motion. It may be thus concluded that the Dehmelt pseudopotential well method and its derivatives underestimate ion velocity by approximately a factor of three, and thus ion kinetic energy by a factor of nine. Note that these values have been scaled to correspond to a maximum amplitude of oscillation of 0.7825 cm corresponding to the z direction of the stretched quadrupole ion trap; to convert to the r direction, divide these values by 0.7825, the ratio of z_0 to r_0 for the Finnigan stretched trap geometry.

In Table 2-4 is presented a summary of ion velocities calculated using the various methods discussed in this chapter. The third column (Hyperion Numerical Integration) contains the maximum ion velocity as calculated via numerical integration of the Mathieu equation using Hyperlon. An arbitrary initial position was chosen and the Mathieu equation of ion motion was integrated numerically with a step size of one three-hundred-and-sixtieth of an RF cycle. The ratio of maximum instantaneous velocity to maximum instantaneous position for a given ion was scaled by the z radius of the stretched quadrupole ion trap (0.007825 m), to yield maximum velocity at that amplitude. This treatment thus assumes that maximum velocity is a linear function of maximum position. Such a relationship is demonstrated in Chapter 3 as the scalability of phase space ellipses. The fourth column ($A\Sigma C_{2n}\omega_n$ Expanded Analytical Solution Model) of Table 2-4 represents the sums of the rows of Table 2-3. The fifth column ($A\beta\Omega_0/2$ Exact Fundamental Frequency Model) corresponds to the velocity calculated based on Bonner's smoothed general solution method, namely, the neglect of the harmonic frequencies of ion motion, and is calculated as the exact fundamental frequency (from equation 2.59) scaled by the maximum amplitude (0.007825 m), with the units of the product converted to meters/second by multiplication by 2π. The sixth column ($Aq\Omega_0/2\sqrt{2}$ Estimated Fundamental Frequency Model) is essentially a crude

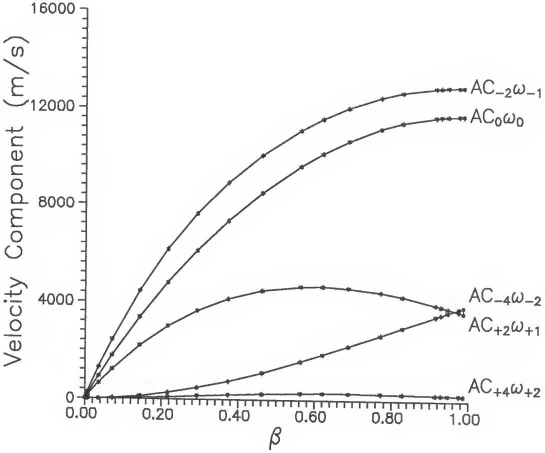

Figure 2-7: Velocity components from table 2-3 plotted as a function of β.

estimation of column five, with β estimated using equation 2.57, with zero a. This column is included because it represents the assumptions utilized in the derivation of the Dehmelt pseudopotential well model.

The columns of velocities from Table 2-4 are plotted in Figure 2-8. Since the basis of the exact fundamental frequency algorithm is a linear relationship between ion velocity and β, its curve is expected to be a straight line. The estimated fundamental frequency model is expected to deviate from the exact fundamental frequency model based on the deviation of the accuracy of equation 2.57 for the calculation of β. The expanded analytical solution model is seen to predict significantly larger ion velocities than either the exact or estimated fundamental frequency models. Curiously, the estimated fundamental frequency model is predicted to be in great error at large values of q and β, yet is closer to the expanded analytical solution model at high q than at low q.

The curve representing Hyperlon numerical integration tracks the expanded analytical solution curve in shape, but is slightly larger in magnitude. The cause for the deviation of the Hyperlon data from the expanded analytical solution is currently unknown. The close tracking of the two methods (Hyperlon, and expanded analytical solution) allows for some confidence in the accuracy of the results presented. Perhaps the assumption of zero initial velocity for the expanded analytical solution model is invalid.

Table 2-5 contains the results of the calculation of maximum ion kinetic energy for m/z 134 via various methods. Column three (Hyperlon Numerical Integration) represents the maximum ion kinetic energy as calculated via numerical integration of the Mathieu equation using Hyperlon. These values were calculated by taking the

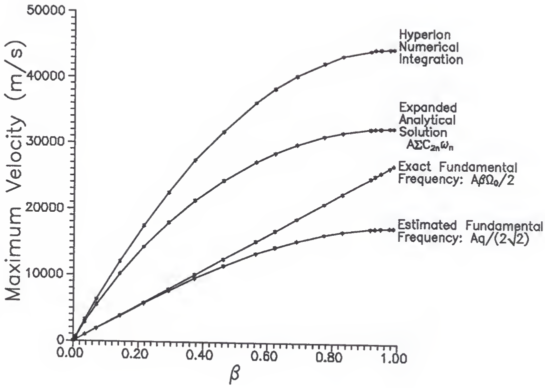

Figure 2-8: Maximum ion velocities from table 2-4 plotted as a function of β.

maximum velocities from Table 2-4 and using equation 2.67 to calculate ion kinetic energies. Conversion from amu·meters²/second² to eV was effected by use of the identities:

$$1\text{eV}=1.602\text{x}10^{-19}\text{kg}\frac{\text{m}}{\text{s}^2} \qquad (2.71)$$

$$1\text{amu}=1.6605\text{x}10^{-27}\text{kg} \qquad (2.72)$$

Columns four, five, and six were calculated in a similar fashion using the corresponding velocities in Table 2-4. The seventh column (qV/8 Dehmelt Model) represents the Dehmelt pseudopotential well model as presented by Todd et al. and was calculated using equation 2.65. The eighth column is a listing of zero-to-peak RF voltages, and was calculated by solution of equation 2.43 for V, with z_0 taken as 0.007825 meters, r_0 taken as 0.010 meters, m taken as 134 amu, and Ω taken as 1.1 MHz.

The maximum ion kinetic energies in columns three to seven in Table 2-5 are plotted as a function of β in Figure 2-9. As would be expected from the proportionality of ion kinetic energy to the square of ion velocity, these curves are an exaggerated version of the relationships shown in Figure 2-8. Notable is the close correspondence between the curves of estimated fundamental frequency and Dehmelt pseudopotential well depth. This is to be expected since they are based on the same fundamental assumptions. The difference between these values is caused by the use of equation 2.40 instead of equation 2.35, which was inherent in the derivation. Equation 2.40 was

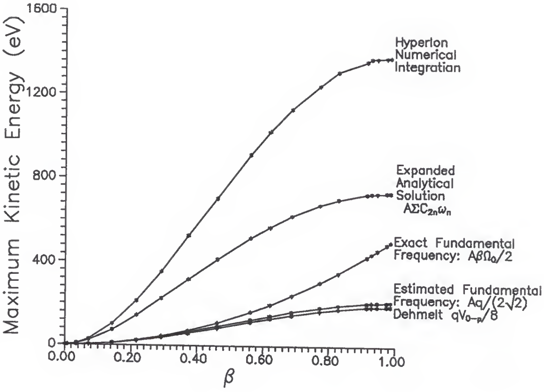

Figure 2-9: Maximum ion kinetic energies from table 2-5 plotted as a function of β.

used because it more truly represents the application of the model to the Finnigan stretched trap geometry.

There is a discrepancy between the expanded analytical solution model and the pseudopotential well model which varies from a factor of five to ten depending on the value of q. At high q, the pseudopotential well model is limited by the poor accuracy of the approximation of β via equation 2.57. The model was never proposed to be accurate at these high values of q (44). This discrepancy suggests that researchers have been underestimating the maximum kinetic energy of an ion stored in a quadrupole ion trap by a factor of ten. The implications of this error are tremendous, causing an opportunity for re-evaluation of published experimental data which identified heretofore unexplainable discrepancies with the pseudopotential well method.

Mathieu Stability Diagrams

This section contains a pedagogical review of Mathieu stability diagrams and related topics. It is included as a review of quadrupole theory which is relevant to the discussion presented in later chapters.

The traditional method for examining the solutions of the parameterized Mathieu equation is to plot a series of solutions in a single graph. Such a graph indicates the range of a and q values which result in stable trajectories simultaneously in the r (x or y) and z directions simultaneously. In addition, the a and q values which result in various values of β are presented in the form of 'iso-β lines'. An example of a parameterized Mathieu stability diagram for a quadrupole ion trap with some iso-β lines is shown in Figure 2-10. The iso-β lines were calculated using a successive approximation algorithm similar to that described in an earlier section of this chapter for

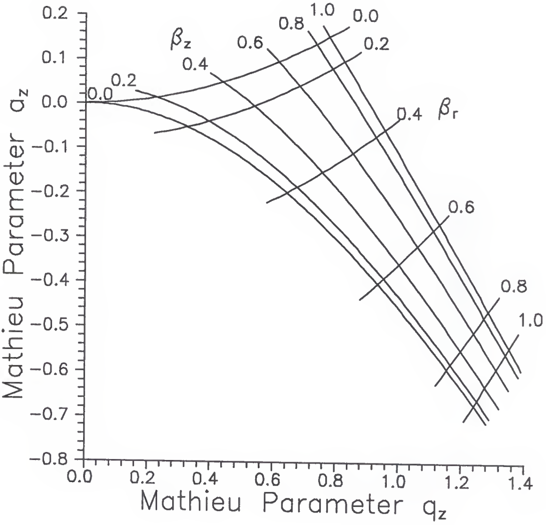

Figure 2-10: Mathieu stability diagram for the first stability region showing iso-β lines.

the calculation of β. The approach for calculating iso-β lines uses the same continued fraction equations, with β held constant, q varied stepwise, and a calculated via successive approximation. The outer limits of the stability diagram are thus the iso-β lines corresponding to β = 0 and 1 in each of the r and z directions.

Stability Diagrams Scaled to m/z

When one scales this parameterized stability diagram from q-a space into RF-DC space using equations 2.27 and 2.28, the resulting plot identifies the stability boundaries and frequencies of ion motion for a given m/z. Figure 2-11 shows three such stability diagrams scaled by mass which illustrate the correspondence between masses and stability limits. From this figure, it is apparent that there exist stability regions (ranges of RF and DC values) which are unique to a given mass (assuming exclusivity of ion polarity). These stability limits at extreme values of positive and negative DC voltage (apices of stability envelope) can be exploited to yield selective mass storage of a unique mass-to-charge ratio through judicious selection of RF and DC voltages (45). Such operation is analogous to the narrow bandpass filter operation of the quadrupole mass filter (1).

Positive and Negative Ion Stability Diagrams

When two stability diagrams are scaled to represent the positive and negative ions of the same mass, it is apparent that there are significant regions where ions of one polarity may be stored exclusive of the other. In Figure 2-12, the points* at the apices corresponding to selective mass storage mentioned in the previous paragraph are identified as points B and C. At the RF voltage identified as point A, application of

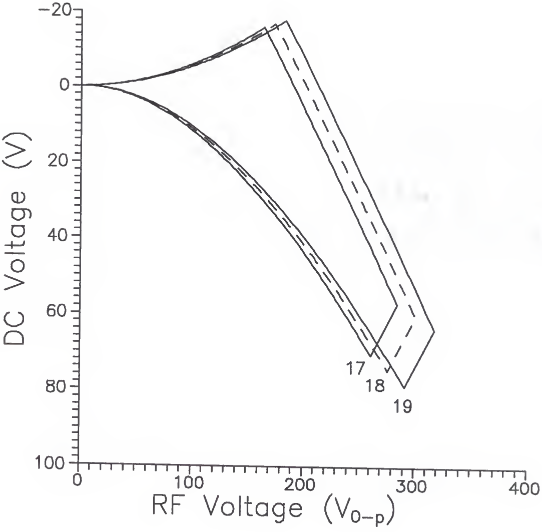

Figure 2-11: Mathieu stability diagrams for the positive ions m/z 17, 18, and 19, plotted in RF-DC space.

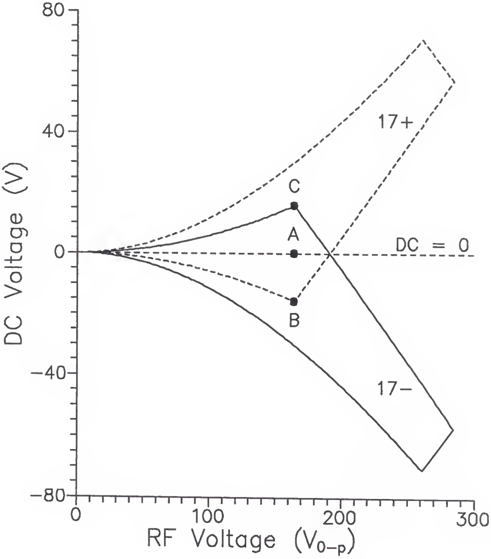

Figure 2-12: Mathieu stability diagrams for the positive (dotted lines) and negative (solid lines) ions of mass 17 plotted in RF-DC space.

DC voltages just larger than those corresponding to points B and C would result in exclusive storage of a narrow range of m/z's of negative or positive ions respectively as has been experimentally demonstrated by Berberich and Yost (45).

Mass-Selective Instability

The mass-selective instability scan mode developed by Finnigan Corporation (46) can be summarized as a linear ramp of RF voltage, which causes masses of increasing m/z to become unstable in the 'z' direction with subsequent detection by some current measuring device. To understand the theoretical basis for this mode of operation, one only needs to examine Figure 2-11. In this figure, it can be seen that the stability diagrams indicate stability for all m/z's at low RF voltages in the absence of DC voltages. As RF voltage is increased, the stability limits for the various masses become important, with lower masses falling out of the stability region before heavier masses. Since there is a linear relationship between the scaling of the parameterized stability diagram to the various m/z's, there is a linear relationship between the RF voltage corresponding to the stability limit of the various m/z's. Such a calibration curve is shown in Figure 2-13, which was calculated via solution of equation 2.40.

Correspondence Between q, β, and Secular Frequency

When the correspondence between q_z and β_z is extracted from the stability diagram shown in Figure 2-10 with the Mathieu parameter a_z assumed zero, the result is a curve which shows a one-to-one correspondence between q_z and β_z. These β

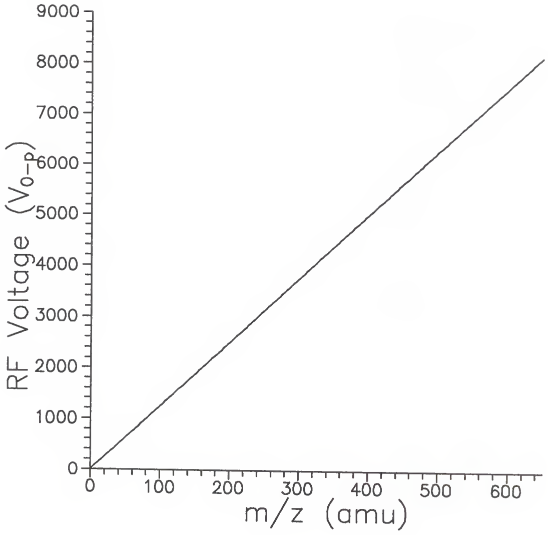

Figure 2-13: Theoretical RF voltage calibration curve for mass selective instability operation of the quadrupole ion trap. $q_{instability}$ was taken as 0.908. $V_{0\text{-}p}$ equals 12.477 times m/z.

values can be scaled using equation 2.44, with the secular frequency corresponding to n=0. The linear relationship between β and secular frequency given in equation 2.56 is utilized in Figure 2-14 through the use of dual y axes. Each point on the stability diagram corresponds to two β values, one for each of the r and z directions.

Correspondence Between q and m/z

When the correspondence between q and m/z is examined for a given value of RF voltage, there is a one-to-one correspondence between q and m/z as shown in Figure 2-15. From this figure it can be seen that as q approaches zero, m/z approaches infinity. Thus it is claimed that RF-only operation of the quadrupole ion trap operates as a high pass filter. There is however a physical limit to the largest m/z which can be stored efficiently based on kinetic energy limits at low q.

Correspondence Between q, β, and Secular Frequency

Replacing the q axis in Figure 2-15 by the corresponding m/z axis results in a calibration of ion secular frequency with m/z (Figure 2-16). Light ions are seen to have very high frequencies of ion motion with heavier ions having correspondingly lower frequencies. The one-to-one relationship to frequency of ion motion in the 'z' direction is maintained.

Analysis of Frequencies in the r Direction

A similar analysis is possible for ion trajectories in the 'r' direction. Figure 2-14 identifies the relationship between q_z and β_r. Since q_r can be defined as half of q_z (from equations 2.35 and 2.38, Figures 2-14 and 2-15 need their m/z axes doubled to

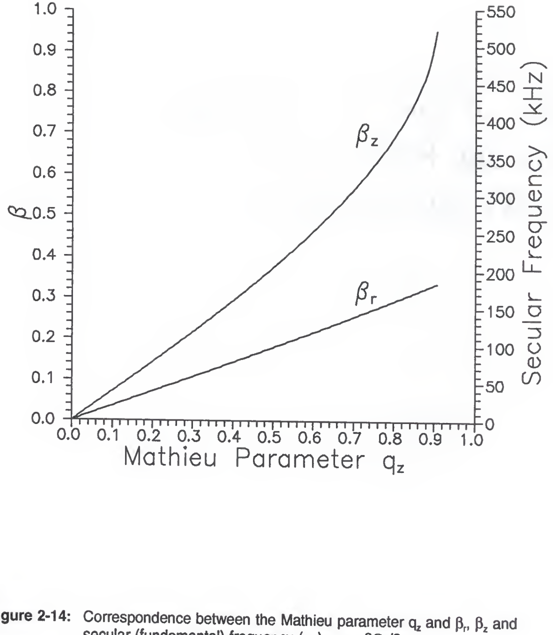

Figure 2-14: Correspondence between the Mathieu parameter q_z and β_r, β_z and secular (fundamental) frequency (ω_0). $\omega_0 = \beta\Omega_0/2$

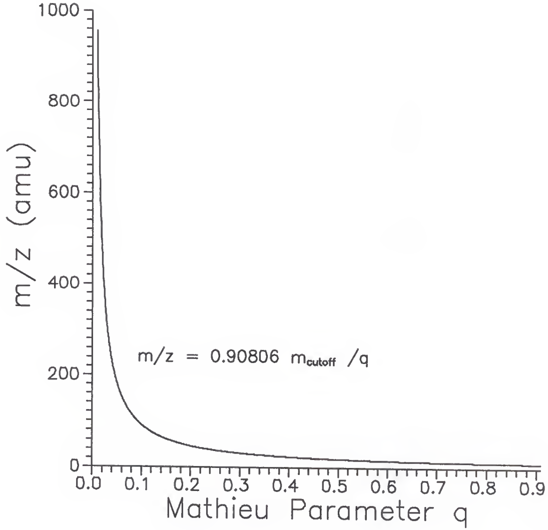

Figure 2-15: Correspondence between mass and the Mathieu parameter q with a constant RF voltage corresponding to m_{cutoff} = 10 amu.

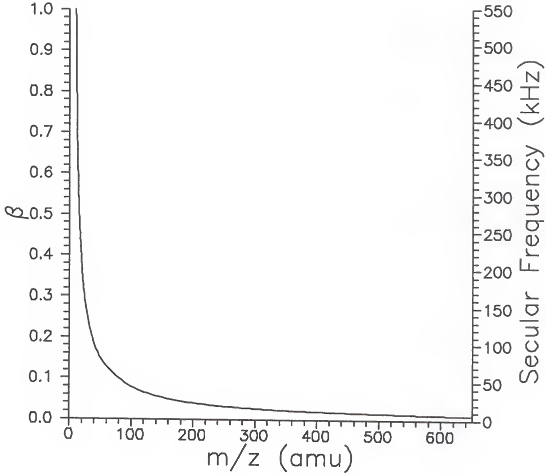

Figure 2-16: Correspondence between mass and β_z and secular frequency for RF-only operation with a constant RF voltage corresponding to $m_{cutoff} = 10$ amu.

identify the correspondence in the 'r' direction. This poses an interesting conclusion. While there is a one-to-one relationship between frequency and m/z in the 'z' direction and in the 'r' direction, when both directions are considered simultaneously, there are two frequencies of ion motion for each m/z. The β values for a given set of a and q parameters can be extracted from the parameterized stability diagram shown in figure 2-10. At every q-a point within the stability region, there are discrete values of β_r and β_z, and thus two discrete secular frequencies. Since a dipolar resonance excitation field acts primarily in the z direction (23), dipolar resonance excitation results in exclusive excitation of a single m/z in the z direction. Since a quadrupolar resonance excitation field acts in both the r and the z direction (23), quadrupolar resonance excitation results in simultaneous excitation of two disparate m/z's, corresponding to the z frequency of a heavy ion and the 'r' frequency of a lighter ion. Thus with quadrupolar resonance excitation, one must consider the fact that each ion has two distinct frequencies, one in each of the r and z directions, whereas with dipolar excitation there is a one-to-one relationship between m/z and fundamental frequency.

Conclusions

In this chapter, the Mathieu equations of motion for an ion in a quadrupole ion trap were derived along with an equation which describes dipolar excitation. A detailed analysis of the analytical solution of this equation was presented, with algorithms for the calculation of β and the characteristic coefficients summarized. The various models for the calculation of ion velocity and kinetic energy were reviewed and critiqued, with a new, more accurate model presented. The Mathieu stability diagram was reviewed along with a brief analysis of some theoretical aspects of quadrupole ion trap operation based on this powerful summary diagram.

The equation of motion for an ion stored in a quadrupole ion trap to which a quadrupolar trapping potential and a dipolar resonance excitation potential are applied was developed. The dipolar excitation field was defined based upon a plate capacitor model in which the field gradient is constant between the endcaps. The magnitude of the resonance excitation field was defined relative to the magnitude of the trapping RF potential.

The trajectory of an ion stored in a quadrupole ion trap is periodic in nature, with the trajectory boundaries unchanging unless that ion is acted upon by some additional force (collision with a neutral molecule, change in trapping field strength, or application of an supplemental resonance excitation field). As such, the quadrupolar trapping potential is effectively a potential energy well, neither adding nor removing energy from an ion stored within.

The analytical solution of the Mathieu equation was reviewed along with some standard algorithms for the calculation of β, frequencies of ion motion (ω_n) and the relative amplitudes of the coefficients (C_{2n}) of the analytical solution. The contribution of higher harmonic frequencies to ion velocities was identified with the astonishing conclusion that the motion at the first harmonic contributes more to ion velocity than motion at the fundamental frequency, even though the amplitude of motion at the fundamental frequency is typically much larger than the amplitude of ion motion at the first harmonic.

The erroneous statement of Wuerker et al. that the high frequency ripple seen in ion trajectories at low q is due to superposition of the RF trapping field is identified, and this erroneous statement is traced through history to the Dehmelt pseudopotential well model, which was shown to underestimate ion energies by an order of magnitude, through neglect of higher harmonic frequencies. It is unfortunate indeed that the pseudopotential well model has been seen such widespread use. It would be very interesting to perform a literature search of experimental data which has been rationalized using the Dehmelt pseudopotential well model, and reinterpret that work using the more accurate model introduced in this chapter. The correspondence between the secular frequency of ion motion and RF and DC voltage and m/z was presented. There is a one-to-one correspondence between secular frequency and m/z in each direction for a given set of experimental conditions. These frequencies differ in the differing directions of ion motion however, resulting in a two-to-two correspondence between frequency and m/z when motion in both the z and r directions are considered. The linear calibration of m/z to RF voltage was presented based on an analysis of the Mathieu stability diagram. Note that all of the data presented in this chapter was based on the Finnigan stretched trap geometry with z_0 taken as 0.007825 meters.

CHAPTER 3

SIMULATION OF ION MOTION AND MODELING OF ION ENERGETICS IN A QUADRUPOLE ION TRAP

Introduction

In Chapter 2, the equations of ion motion for ions stored in the quadrupole ion trap were derived, and an analysis of the analytical solution of the Mathieu equation was presented along with a new model for estimation of ion velocity and ion energetics. Computer programs were written which model ion motion and ion energetics in a quadrupole ion trap based on numerical integration of the perturbed Mathieu equation (equation 2.31), and through analysis of the analytical solution of the Mathieu equation (equations 2.41, and 2.70). Some results of these model programs are presented in this chapter which demonstrate the utility of theoretical modeling of the behavior of ions stored in the quadrupole ion trap. Included in these results are an analysis of modeled ion trajectories which match ion trajectories of aluminum microparticles photographed by Wuerker et al. (6), a review of dipolar resonance excitation as simulated through the plate capacitor model, and a review of some theoretical aspects of ion injection including a discussion of phase space diagrams and an analysis of ion energetics based upon the expanded analytical solution of the Mathieu equation.

Numerical Integration of the Mathieu Equation

Previous Work in Computer Simulation of Ion Motion in Quadrupole Devices

Early workers in quadrupole mass spectrometry relied on analytical theory and tedious hand calculations to predict the experimental effects of applied voltages on ion trajectories. It was not until the mid 1960s that numerical integration of the equations of motion for ions traveling within quadrupole mass spectrometers was first performed with digital computers (47). In this early ion trajectory simulation work, Lever solved the Mathieu equations of motion for an ion traveling through a monopole mass spectrometer using a fourth-order Runge-Kutta algorithm. An IBM mainframe was used to calculate the trajectories with off-line plotting. In this important work, Lever demonstrated that the then current operational mode for the monopole mass spectrometer was not especially effective and proposed a new operational mode based on computer simulation results. Lever outlined the method for computer simulation of ion motion in a quadrupole mass spectrometer, including FORTRAN code for the Runge-Kutta integration algorithm.

Dawson used similar methods to simulate ion motion for ions transmitted through a quadrupole mass filter, as well as within an ion trap, with imperfect fields. (10, 48, 49) In this work, a modified form of the Mathieu equation was solved, simulating ion motion through a quadrupolar field which has additional weak hexapolar fields and octopolar fields. This work addressed the experimental phenomenon of non-Gaussian mass spectral peaks. Dawson showed simulated mass spectral peaks which exhibited splitting, and demonstrated the dependence of this peak splitting on nonlinear resonances due to imperfect fields. Dawson also pioneered the use of matrix methods based on phase-space dynamics to rapidly calculate the maximum ion displacement of an ion trajectory in an ion trap based on its initial conditions (50, 51).

The simulation of collection and storage of ions injected into a quadrupole ion trap was reported by a number of groups in the late 1970s and early 1980s. Ghosh and co-workers, of the Indian Institute of Technology, used numerical methods to solve the Mathieu equation for ions injected into the ion trap under a range of conditions (52). They concluded that injection of ions into the ion trap would be best done by transmitting a divergent beam of ions through one of the endcaps. Physicists Chun-Sing O and Hans A. Schuessler of Texas A&M University used phase-space methods to calculate the ion confinement capabilities of the quadrupole ion trap for ions injected into the ion trap from an external source (53, 54, 55). From these simulation studies, these researchers determined that the optimum conditions for ion injection and collection were small ion energies with large incidence angles. Their conclusions agreed with those of Ghosh, in that injection through an endcap would be more efficient than through the ring electrode. They also determined through simulations that ions are only collected during a very narrow range of RF phases centered around 270° for quadrupole ion traps with RF voltage applied to the ring.

More recently, Todd has simulated the effects of collisions of ions stored in the ion trap with neutral buffer gas molecules (56). Todd demonstrated the effectiveness of helium as a buffer gas in reducing the width of the distribution of ions ejected from an ion trap under the mass selective instability mode of operation. This simulation provides an explanation for the ability of helium buffer gas to reduce the width of an ion mass spectral profile.

Pedder and Yost at the University of Florida have presented simulation results from the BASIC program Hyperlon, which predict the effectiveness of resonance excitation at harmonic frequencies, the effects of buffer gas at collisionally cooling stored ions (57), the resolution of resonance excitation (58), and the effective energy of electrons injected into the quadrupole ion trap (58, 32). The features of Hyperlon are reviewed in this chapter.

The Cooks group at Purdue University has recently demonstrated simulation results which model high resolution operation of the quadrupole ion trap (59, 60). They also have predicted the occurrence of surface-induced dissociation through the simulated application of a DC pulse to the endcap electrodes (61, 62). The Cooks group has also made available upon request the run-time version of a PC-based computer simulation program which allows the calculation of ion position, velocity and kinetic energy as a function of time for a user-defined set of initial conditions.

Ray March et al. have published a series of papers on the subject of computer simulation of ion motion in the quadrupole ion trap (23, 24, 25). In the earliest of these works (23) the Mathieu equation of ion motion with perturbation was integrated using the Livermore Solver for Ordinary Differential Equations (LSODE). This first paper is notable in that it introduces the notion of fluence: the observation that for a given mass at a given set of operating parameters, the excitation voltage multiplied by excitation time is constant for ion ejection. Such a relationship had been already been identified in our lab in early 1988, but had not yet been published. The later two papers by this group (24, 25) focused solely on resonance excitation.

The Hyperlon Numerical Integration Program

The BASIC computer program Hyperlon was developed at the University of Florida in order to provide better understanding of the experimental results seen in the quadrupole ion trap mass spectrometer (32, 57, 58). The original code for the fourth-order Runge-Kutta algorithm (63) was provided by William Fies Jr. of Finnigan Corporation. This core code was modified to include the plate capacitor model for dipolar resonance excitation (equation 2.31). A number of user interface elements were added including graphical display of ion trajectories. Essentially, Hyperlon calculates the trajectory for a single ion traveling through the field inside of the quadrupole ion trap via numerical integration of equation 2.31. A functional version of Hyperlon is presented in Appendix 2. Note that this version has been stripped of significant portions of extraneous user interface code in order to minimize its size.

The features of this program include the ability for the user to select a given mass-to-charge ratio, identify an initial set of conditions (position, velocity vector, RF and DC voltages, RF frequency...) with numerical integration of the Mathieu equation for that set of initial conditions. The run-time version of the program allows for user-defined ramp rate of the RF amplitude with keyboard toggle control of RF ramping and toggle control of user-defined resonance excitation voltage and frequency, including automated calculation of theoretical frequency using the algorithm described in chapter 2. With the run-time version of Hyperlon, the user has the capability to instantaneously change any of the following parameters from the keyboard: integration step size, mass-to-charge ratio, RF voltage, DC voltage, position, velocity vectors, Mathieu a and q parameters, and RF phase. The user also has the ability to initiate the calculation and display of a fast Fourier transform of ion trajectory, as well as generate a hardcopy of the current graphic screen to an Epson-compatible printer. An early version of HyperIon included capability of simulating the effects of buffer gas through either a viscous drag model, or a discrete collision model (57).

There are two distinct methods for learning about ion behavior in a quadrupolar field using HyperIon. The most simple and straightforward method is simply to manually simulate an experiment through variation of experimental parameters at run-time via the keyboard (i.e. manually toggle resonance excitation voltage on and off, toggle DC voltage on and off...) The graphical display provides instantaneous feedback, allowing for intuitive visualization of experimental phenomena. A more detailed analysis of experimental phenomena can be effected through modification and recompilation of the HyperIon source code to automate the keystroke sequences.

By simple modification of the source code, simulated experiments can be performed including scheduled variation of various parameters (i.e. enable resonance excitation after twenty microseconds, pulse DC on after forty microseconds...). Through addition of a simple for-next loop, a series of experiments can be modeled within a single program (i.e. variation of initial RF phase for electron injection experiments modeled in Chapter 4). Through judicious placement of print statements, any experimental parameter may be logged to disk as a function of time. Almost any single-ion experiment imaginable can be modeled through simple adjustment of the source code.

Experimental Conditions for HyperIon Numerical Integration

The application of a Runge-Kutta numerical integration routine to a second order differential equation is relatively straightforward. There is a minor challenge in scaling the magnitudes of the various parameters to maintain physical significance of the results. In Hyperlon, all units are maintained in, or are readily convertible to MKS units (meters, kilograms, seconds). This section summarizes the conversions performed to transform from laboratory units into the MKS units utilized in the Hyperlon program.

The conversion from time in microseconds to the fraction of an RF cycle integration step size (fraction of a radian) was effected through the following identity:

$$\Omega \text{ (radians)} = 2\pi f \text{ (Hertz)} \tag{3.1}$$

The conversion from energy in eV to velocity in meters per second was effected using equations 2.67, 2.71 and 2.72.

Velocities are represented internally in Hyperlon in units of meters per radian, and are converted to meters per second via equation 3.1 prior to display or storage to disk.

Unless otherwise noted, all simulations were performed using the Finnigan ITMS as a model, assuming a stretched trap geometry. The experimental parameters assumed are thus: $r_0 = 0.01$ meters, $z_0 = 0.007825$ meters, RF frequency = 1.1 MHz, with DC and zero-to-peak RF voltage calculated using equations 2.42 and 2.43 (41). Resonance excitation voltages are scaled as peak-to-peak voltages to maintain compatibility with Finnigan MAT ITMS software Revision B, with the resonance excitation field calculated using equation 2.33. Resonance excitation frequencies are transformed from the user units of Hertz to the internal representation of radians^{-1} via equation 3.1.

Hyperlon Simulation Example: Simulation of the Trajectory of Wuerker's Stored Microparticle.

In Chapter 2, the erroneous conclusion of Wuerker et al. concerning the source and frequency of the low amplitude ripple seen in the classic photograph of the stored microparticle shown on page 346 in reference 6 (also reproduced on page 139 of reference 22, and on page 200 of reference 3) was corrected through simple analysis of the analytical solution of the Mathieu equation, attributing this ripple to ion motion at harmonic frequencies. In this section, results from the Hyperlon computer simulation of the q-a conditions identified in the caption of the photograph in question is shown, which further corroborates the explanation given in Chapter 2. Figure 3-1 contains a projection in the r-z plane of the trajectory of an ion with Mathieu a and q parameters of 0 and 0.232 respectively. The 2:1 Lissajous appears to closely match the shape of the trajectory shown in the Wuerker photograph; however, the Wuerker photograph contains the equivalent of four cycles of ion motion at the fundamental frequency in the z direction, whereas the simulated trajectory contains only two cycles. The high frequency ripple in the overlaid Lissajous figures in the Wuerker photograph appear to be out of phase with each other, but the relationship between the fundamental frequency and the harmonic frequencies is clearly comparable between the simulated trajectory and the Wuerker photograph.

When the z coordinate of this trajectory is plotted as a function of time (as shown in Figure 3-2), the periodicity of the fundamental and harmonic frequencies is apparent. When such a z coordinate versus time data set is apodized and subjected to fast Fourier transform algorithm as described in Chapter 2, the result is a power spectrum of intensity versus frequency, also shown in Figure 3-2. The relative

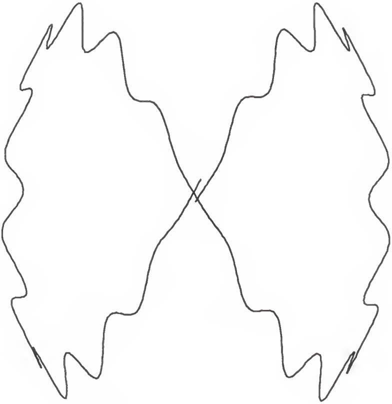

Figure 3-1: Two-to-one Lissajous figure representing the a projection into the r-z plane of the trajectory of an ion stored in the ion trap with a=0 and q=0.232, corresponding to those noted in the figure caption of Figure 7 of reference 4.

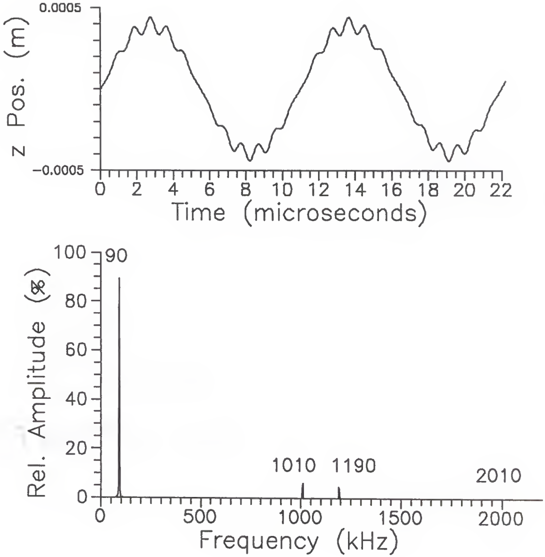

Figure 3-2: z trajectory plotted as a function of time with fast Fourier transform corresponding to the ion trajectory shown in Figure 3-1. Fundamental frequency is calculated to be 90 kHz from the fast Fourier transform.

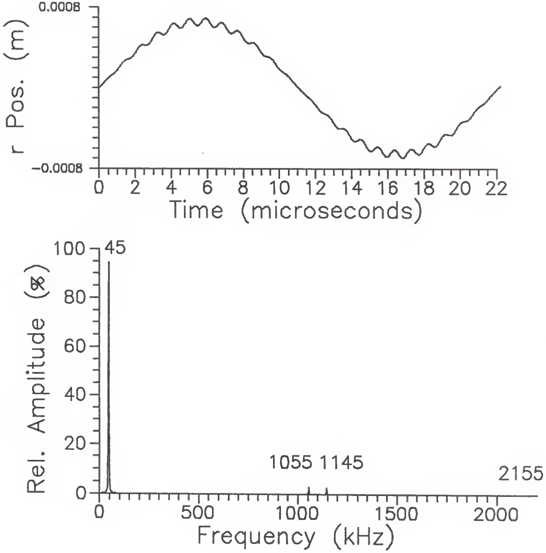

Figure 3-3: r trajectory plotted as a function of time with fast Fourier transform corresponding to the ion trajectory shown in Figure 3-1. Fundamental frequency is calculated to be 45 kHz from the fast Fourier transform.

amplitudes from this figure match well with those calculated via the analytical solution of the Mathieu equation (see Table 3-1). Note that the average of the first two harmonic frequencies corresponds to the RF drive frequency. It is quite reasonable therefore, that the oscillations could be confused with the drive frequency, which may have led to the aforementioned erroneous conclusion of Wuerker.

Table 3-1: Comparison between normalized coefficients (C_{2n}) calculated using equation 2.48, and frequencies calculated through solution of equation 2.47 with coefficients and frequencies calculated using Hyperlon.

Normalized C_{2n} (equation 2.48) (%)	Normalized C_{2n} Hyperlon (%)	ω_n (equation 2.47) (kHz)	ω_n Hyperlon (kHz)
89.262	89.321	91.205	90
6.162	6.161	1008.795	1010
4.418	4.422	1191.205	1190
0.097	0.096	2108.795	2010

When the r coordinate of Figure 3-1 is plotted as a function of time, as shown in Figure 3-3, the result is similar to Figure 3-2: a large amplitude, low frequency fundamental superimposed with high frequency low amplitude harmonics. Comparing the frequencies from the Fourier transforms in Figures 3-2 and 3-3, it is clear that the z direction fundamental frequency shown in Figure 3-2 is twice that of the r direction fundamental frequency shown in Figure 3-3, as can be inferred from the fact that a plot of x coordinate versus z coordinate (Figure 3-1) represents a two-to-one Lissajous figure. Thus it is with great confidence that this researcher refutes the claim of Wuerker that the low frequency ripple seen in ion trajectories at low values of q can be attributed to superposition of the RF drive frequency. In this presentation, it has been demonstrated that this high frequency ripple is due to motion at harmonic frequencies, whose presence was verified experimentally as shown in the next section.

Hyperlon Modeling of Resonance Excitation

The resonance excitation perturbation term of equation 2.36 approximates the acceleration due to the dipolar field which is present when a sinusoidal potential is applied between the endcaps of the quadrupole ion trap with a 180^0 phase differential. From equation 2.10, it can be seen that this field is constant along the z axis independent of the distance from the center of the ion trap. Since the field strength is constant along the z axis, it would be predicted that the perturbation of ion trajectories in the z direction due to this excitation field will be independent of distance from the center of the quadrupole ion trap. The net effect of the resonance excitation field would be to force the oscillations of all ions stored in the quadrupole ion trap into phase with the resonance excitation voltage. For ions which have resonant frequencies widely different from the resonance excitation frequency, this perturbation will result in the superposition of a low amplitude beating pattern on the natural frequencies of oscillation, with the ion motion coming into and out of phase with the resonance excitation voltage, and with little net increase in amplitude of oscillations, and hence ion energetics.

For ions which are exactly in resonance with the resonance excitation frequency, the ion trajectory is seen to first adjust its phase to match that of the resonance excitation voltage, followed by a linear increase in maximum amplitude of oscillation with time. Such a resonance condition can be likened to that of a parent pushing a child on a swing. With small accelerations (pushes) matched to the frequency of the swinging of the child, the parent is able to either decelerate the child (if the parent pushes out of phase with the oscillations, the amplitude of the child's oscillations can gradually be damped to zero) or accelerate the child to larger velocities (with concurrent increase in the maximum excursion from the point of rest). In the child's swing model, the magnitude of the accelerations due to the parent's pushes is small relative to the accelerations due to earth's gravity. Similarly, the magnitude of the acceleration due to resonance excitation is small compared to the magnitude of the acceleration due to the trapping field (corresponding applied potentials are fractions of a volt for resonance excitation compared to thousands of volts for the trapping potential).

The data shown in Figure 3-4 were calculated using Hyperlon, and represent the trajectory of an ion stored in a quadrupole ion trap, with z coordinate plotted as a function of time. Experimental conditions were m/z 134, 553.5 $\text{Volts}_{0\text{-}p}$ RF (i.e. q_z = 0.300), no DC voltage. A 500 $\text{mV}_{p\text{-}p}$ resonance excitation voltage was applied with a resonance excitation frequency of 118.8 kHz. The theoretical fundamental frequency under these conditions is 118.807 kHz (from Table 2-2). The initial position and velocity were chosen such that the fundamental frequency of ion motion was significantly out of phase with the resonance excitation frequency. It is interesting to note that under the conditions modeled, the ion was damped to the center of the quadrupole ion trap before it was accelerated ultimately to exit the confines of the electrode structure. Resonance excitation can decelerate as well as accelerate, depending on the phase coherence of the ion motion relative to the excitation voltage. Also interesting is the fact that the maximum excursion of the ion increases linearly as

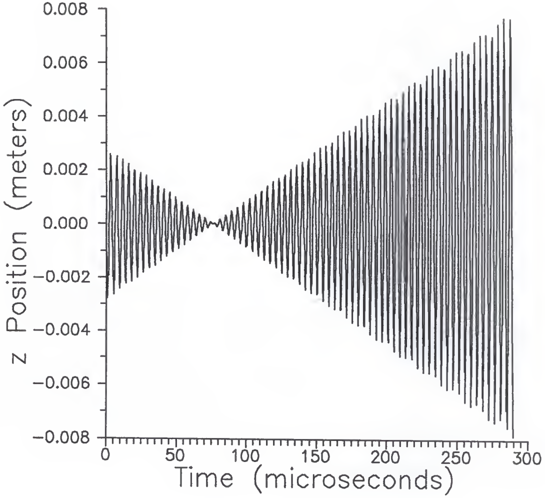

Figure 3-4: Simulated resonance excitation trajectory of m/z 134 in the z direction as a function of time. q_z=0.3, resonance excitation voltage and frequency were 1000 mV_{p-p} at 118.8 kHz.

a function of time, hence the 'fluence' originally proposed by March et al. (23) can be demonstrated using this model. For the case of q=0.3 shown in this example, the fluence for ejection is calculated to be approximately 106 $mV_{p\text{-}p}ms$. The excitation time was taken as the time interval that it took the resonance damped ion to have its trajectory amplitude exceed the confines of the ion trap.

This method was used to estimate the fluence under the conditions outlined by March et al. in reference 25. A summary of the results of the calculation of fluence through the two methods is presented in Table 3-2. It is apparent that the Hyperlon results are approximately a factor of two lower than those reported by March et al., which represents a stronger field in the Hyperlon model compared to the model proposed by March et al. The cause for this discrepancy is currently unknown. Regardless of the source of the discrepancy, discussion of relative fluences within one model is meaningful.

Table 3-2: Fluences required for ejection of m/z 134 calculated as a function of q. March data were taken from Table 2 of reference 25; Resonance excitation voltage was 1 $V_{0\text{-}p}$.

q_z	Hyperion Fluence ($mV_{0\text{-}p}ms$)	March Fluence ($mV_{0\text{-}p}ms$)
0.2502	35	80.5
0.3750	50	111.5
0.4997	60	140.4

Experimental conditions:
RF Frequency: 1 MHz
m/z 134
r_0=0.01 m
z_0=0.00707 m

When the calculated fluence is plotted as a function of the Mathieu parameter q for ion m/z 134 using the typical operating conditions of the Finnigan quadrupole ion trap (1.1 MHz drive frequency, 0.007825 m z_0...) (see Figure 3-5), it is evident that the required fluence is smallest at low values of q and high values of q. At the first approximation (assuming all motion is at the fundamental frequency), it would be reasonable to predict that since the trapping potential (maximum kinetic energy tolerated) increases as a function of q, so should the fluence required for ejection. The fluence would be thus expected to scale with pseudopotential well depth. At low values of q, this assumption is reasonable, since the relative amplitude of the fundamental frequency indeed dominates the ion trajectory (see Table 2-2). As q increases, the relative amplitudes of the harmonic frequencies becomes significant, thus the fluence required to eject an ion could be predicted to fall off slightly since the relative contribution of the fundamental frequency to the ion trajectory falls off at higher values of q. Indeed, a plot of fluence as a function of column 3 of Table 2-3 ($AC_0\omega_0$) is linear up to the points corresponding to q_z=0.5 (i.e. fluence does seem to have a linear relationship with calculated maximum velocity).

As q approaches 0.908, the beating pattern of the fundamental and the first harmonic frequency becomes dominant (see Figure 3-6), and resonance excitation at the fundamental frequency effectively excites to some extent at the first harmonic frequency. The result is an effective increase in the effective amplitude of ion oscillation, resulting in an effective decrease in the fluence required for ejection. Thus it would be predicted that as q approaches 0.908, the required fluence would approximately halve due to its effectiveness at two frequencies. There is apparently a more complex relationship between q and fluence than has been discussed here.

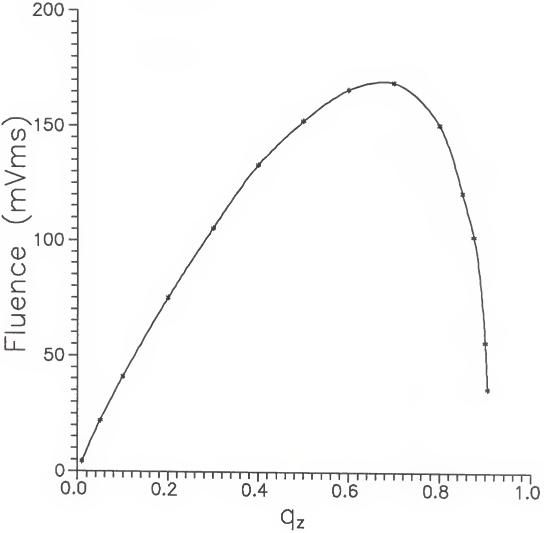

Figure 3-5: Fluence calculated via Hyperlon for m/z 134 plotted as a function of the Mathieu parameter q_z.

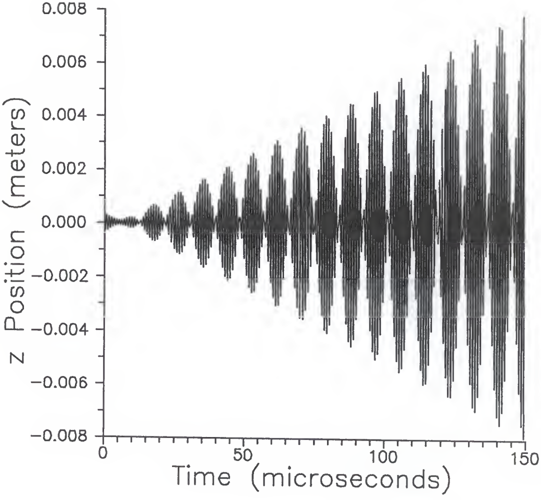

Figure 3-6: Simulated Hyperlon resonance excitation experiment for m/z 134 at a q_z of 0.905.

Perhaps the fluence required for ejection is related to the relationship between the maximum distance from the center of the ion trap that an ion can have at any phase of RF (i.e. the positional limit of the acceptance ellipse at the center of a phase space diagram) and the maximum distance from the center of the trap that an ion can have (i.e. the radius of the hyperbolic electrode). From the phase space diagrams presented later in this chapter, it is evident that as q approaches 0.908, the radius of the acceptance ellipse (the maximum positional distance from the center of the center acceptance ellipse which contains points common to all of the individual phase space ellipses) appears to shrink, similar to the required fluence for ejection as shown in Figure 3-5. Perhaps the fluence required for ejection can be predicted based on a combination of pseudopotential well depth and the ratio of the radius of the phase space acceptance ellipse to the radius of the electrode.

Some simple experiments were performed on the Finnigan ITMS to verify the relative effect of resonance excitation at harmonic frequencies (57) wherein a resonance excitation daughter experiment was performed on m/z 134 of n-butylbenzene through resonance at the fundamental (119 kHz) and at each of the first two harmonic frequencies (979 kHz and 1217 kHz) at a value of q_z of 0.3. The fluence required for the appearance of the m/z 91 fragment of the molecular ion m/z 134 was measured in separate experiments for each of the resonance frequencies with a 5 ms excitation time. It was demonstrated that the appearance of m/z 91 required 14.5 times as much fluence for the first harmonic as the fundamental, and 32.3 times as much fluence for the second harmonic as the fundamental. By simply scaling the relative coefficients from Table 2-1 to each other, it would be predicted that the fluence ratios would be 6.4 to 1 and 16.2 to 1 for the first and second harmonic to the fundamental respectively. The voltages used in the calculation of fluence are uncalibrated, and uncorrected for the rise time of the frequency synthesizer which can be significant at the large amplitudes used in this study. Although the absolute magnitude of the relative fluences differed from theory by approximately a factor of two, resonance excitation was demonstrated at harmonic frequencies. Thus the predictions of multiple frequencies of ion motion from analytical theory were demonstrated experimentally.

Another issue which must be considered in a discussion of resonance excitation is the energetics of ion motion. Since resonance excitation is generally performed for either ion activation or ion ejection, it is helpful to consider the implications of maximum ion energy as a function of the Mathieu q parameter. Table 2-5 identifies the maximum ion kinetic energies for an ion for various values of q_z. The maximum kinetic energies of m/z 134, as calculated through the expanded analytical solution of the Mathieu equation, are plotted in Figure 3-7 with dual x axes to emphasize the relationship between m_{cutoff} and q_z as shown in Figure 2-14. This figure can be interpreted to indicate that the maximum amount of kinetic energy without ejection for a given ion undergoing resonance excitation increases dramatically with increase in q_z. Since the collision-induced dissociation experiment is based upon the transference of kinetic energy into internal energy through collisions of ions with neutral molecules, capacity for more kinetic energy would be predicted to be accompanied by the potential for more energetic dissociation spectra as has been demonstrated (29, 64). This figure can also be interpreted to indicate that there is a sacrifice made in selecting high values of q_z (higher m_{cutoff}) to obtain high internal energy fragmentation, namely a decreased range in daughter ion masses which can be stored.

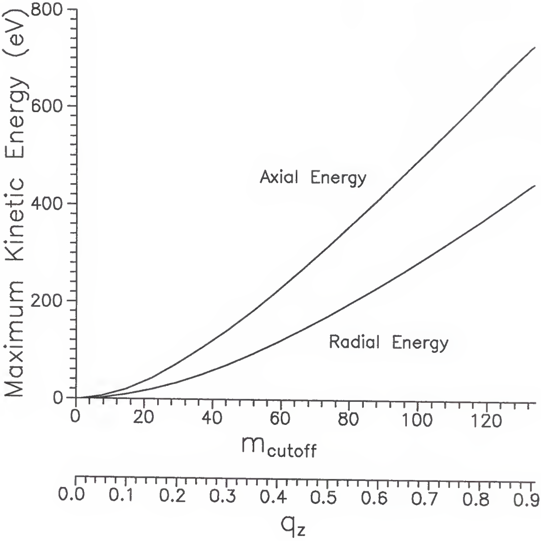

Figure 3-7: Maximum axial and radial energies for m/z 134 as a function of q_z and m_{cutoff}. Energies were calculated using the expanded analytical solution model of ion energetics, presented in Chapter 2.

The competition between resonance ejection and collision-induced dissociation can be analyzed based on the results presented in this section. Since at low values of q (<0.2), the trapping field is such that there is a relatively small energy barrier which contains the ion trajectory, even relatively small fluences will result in ejection. Since collision-induced dissociation requires a certain amount of kinetic energy to be internalized within a reasonable period, the barrier for ion containment may be effectively lower than the energy barrier for fragmentation. At medium values of q_z, ($0.2<q_z<0.85$) the energy barrier for ejection is typically much higher than the effective energy barrier for fragmentation, and fragmentation is seen to dominate. As the fundamental and first harmonic frequencies approach each other in both frequency and relative amplitude, the fluence required for ejection is seen to diminish dramatically, resulting in the increased probability of ion ejection over dissociation, in spite of the extremely large energy barrier for ion ejection. The axial modulation technique of Weber-Grabau et al. (26) is predicted to be most effective for values of q_z where the fluence required for ejection is relatively small (i.e. $q_z<0.2$ or $q_z>0.85$).

Theoretical Aspects of Ion Injection

A fair amount of theoretical work has been presented in the past concerning the theoretical probability of collection and storage of ions injected into the quadrupole ion trap from an external source (52, 53, 54, 55). This section will serve as a review of the issues to be considered in determining the relative probability of collection and storage of ions injected into the quadrupole ion trap.

Phase Space Dynamics

It has been observed that for a given set of initial conditions, the trajectory of an ion stored within a quadrupole ion trap can be analyzed by plotting its instantaneous velocity as a function of its instantaneous position in Cartesian coordinates (3, 22). If the data points are sampled from a simulated trajectory at a rate which is an integer fraction of the drive frequency, the resulting plot appears to consist of a number (one over the integer fraction) of ellipses centered around the origin, with each ellipse corresponding to a given phase of the RF drive frequency (see Figures 3-8, 3-9, and 3-10). It has been observed that such a set of ellipses describes the trajectory of that ion completely under that set of initial conditions (barring any external forces or change in conditions)(3). Thus the use of phase space diagrams is a convenient method of characterizing ion trajectories and energetics. A detailed review of phase-space dynamics is presented in Chapter 2 of reference 22.

The method used in this work for the calculation of the data points for a phase-space diagram is straightforward. The source code for HyperIon was modified to allow the position and velocity every one-fourth cycle of the RF drive frequency to be written to disk. The Mathieu equation was integrated with a phase increment (step size) of one sixteenth of the RF cycle (22.5°). After a suitable number of data points were acquired, these data were plotted in position-velocity space as shown in Figures 3-8, 3-9, and 3-10). From equation 2.70, the maximum velocity of an ion stored in a quadrupole ion trap scales linearly with the maximum excursion (the A term in equation 2.70). Since a phase-space diagram is bounded in the position direction by the largest excursion (i.e. the maximum amplitude A of the trajectory), and is bounded in the velocity direction by the maximum velocity of the ion trajectory, the phase-space

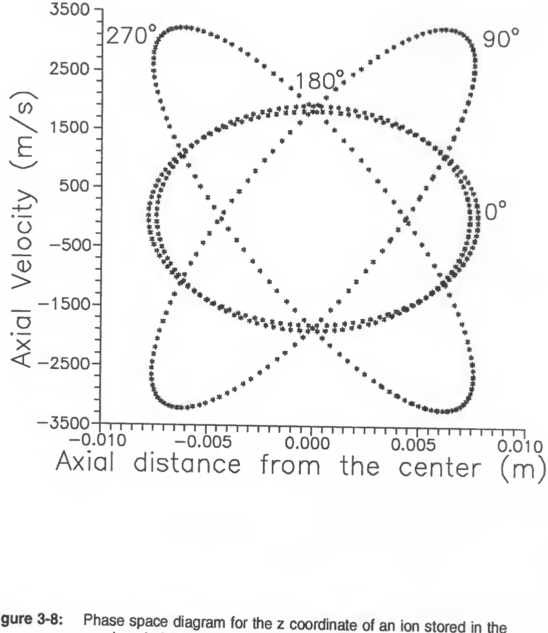

Figure 3-8: Phase space diagram for the z coordinate of an ion stored in the quadrupole ion trap with q_z=0.05. Each ellipse is labeled with the RF phase angle at which its data points were sampled.

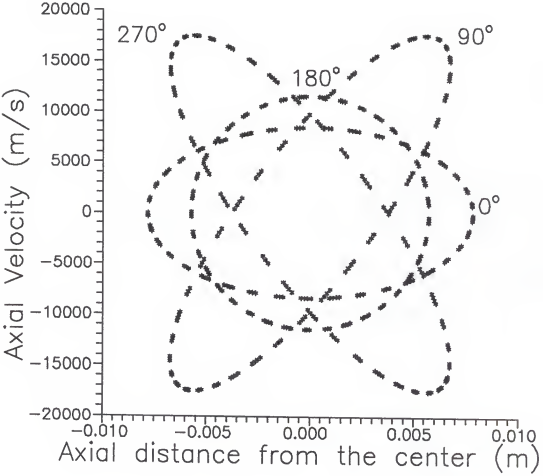

Figure 3-9: Phase space diagram for the z coordinate of an ion stored in the quadrupole ion trap with q_z=0.3. Each ellipse is labeled with the RF phase angle at which its data points were sampled.

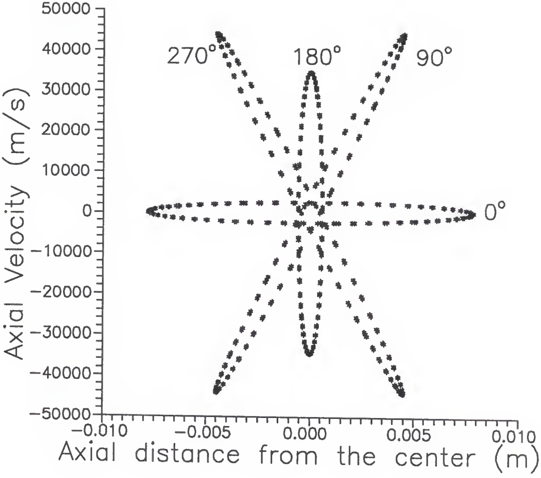

Figure 3-10: Phase space diagram for the z coordinate of an ion stored in the quadrupole ion trap with q_z=0.9. Each ellipse is labeled with the RF phase angle at which its data points were sampled.

diagram inherently contains the information in the relationship described by equation 2.70, that is, the relationship between maximum amplitude and maximum velocity for a given set of conditions. Using this assumption, a phase-space diagram may be scaled linearly to represent any maximum amplitude of excursion (conveniently selected here to correspond with the electrode limits of the ion trap).

The interpretation of a phase-space diagram is also straightforward. If one were to view a phase-space diagram which has been scaled such that its maximum positional excursion corresponds with the electrode radius of the quadrupole ion trap, the area within each ellipse corresponds to the range of positions and velocities which correspond to a stable trajectory within the quadrupole ion trap. Points which are very near the origin of the phase-space diagram (small velocity and small axial displacement) are predicted to have stable trajectories regardless of the initial RF phase. Thus ions generated very near the center of the quadrupole ion trap have a very high probability of being trapped so long as they have minimal initial velocity (which is typical for electron ionization). Ions which are generated either with significant velocity, or are generated at a large displacement from the center of the ion trap will have an RF-phase-dependent acceptance. Thus the elliptical area near the origin of the phase-space diagram which is contained within all of the phase-space ellipses is commonly called the acceptance of the quadrupole device. An analysis of Figures 3-8, 3-9, and 3-10 would indicate that the positional acceptance of the quadrupole ion trap is largest at low values of q, and the velocity acceptance of the quadrupole ion trap increases with increasing values of q.

When one considers the acceptance criteria for an ion injected into the quadrupole ion trap from an endcap electrode, the following conclusions surface. Only at a very narrow range of RF phases centered around an RF phase angle of 0^0 (and at low values of q, 180^0) do the phase-space ellipses indicate acceptance of an ion whose maximum excursion from the center of the ion trap coincides with the endcap electrode radius, and then only if such an ion has negligible axial velocity. Since an injected ion by definition has a maximum excursion which is larger than the axial radius (i.e. its trajectory follows a set of phase-space ellipses which envelope the maximum phase-space ellipses for acceptance), an ion injected into the quadrupole ion trap has enough velocity to escape the trapping field. Only some decelerating force such as a collision with neutral molecules, or some resonance damping as shown in the previous section, can allow for the shrinking of the an ion's set of phase-space ellipses to be enveloped by the maximum phase-space acceptance ellipse of the ion trap. It is therefore predicted that the collection efficiency of ions injected into the quadrupole ion trap will be much smaller than the collection efficiency of ions generated near the geometric center of the quadrupole ion trap, since ions generated near the center of the quadrupole ion trap are predicted to be collected at all phases of RF drive frequency, but ions injected into the ion trap are predicted to be accepted only at a very narrow range of phases of the RF drive frequency.

Having identified the trend in the relative shapes of the phase-space acceptance ellipses, and having identified the relationship between the maximum velocities predicted by equation 2.70 and the maximum velocities in a phase-space ellipse, it is interesting to consider the maximum acceptable velocity (calculated through solution of equation 2.70) as a function of mass for a given magnitude of RF trapping potential as shown in Figure 3-11. A low mass cutoff (m_{cutoff}) of ten amu was modeled, which is representative of the lower range of ionization RF voltages typically

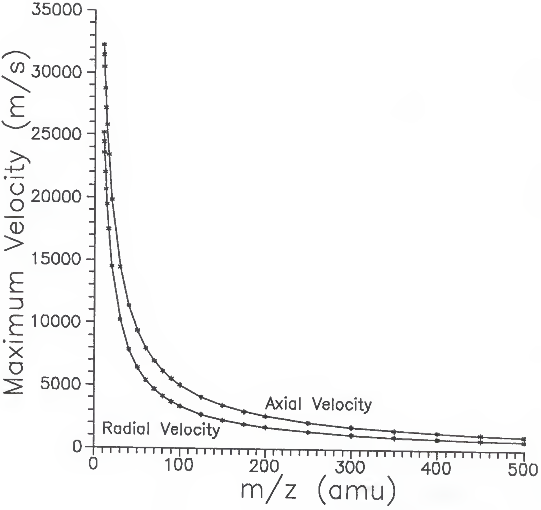

Figure 3-11: Maximum ion velocities as a function of mass for ions stored in a quadrupole ion trap with RF voltage set to correspond with m_{cutoff} of 10 amu.

used in electron injection as well as ion injection experiments. From this figure it can be inferred that light ions can have much larger velocities than heavy ions and still be trapped within the quadrupole ion trap. Similarly, much larger ion energies are tolerated for low mass ions than for high mass ions, as shown in Figure 3-12. Note that the maximum kinetic energy for high mass ions, is in the range of a few eV. It is therefore predicted that maximum collection efficiency of ions injected into the quadrupole ion trap will occur for ions injected with very low ion kinetic energies (a few eV).

The collection and storage of ions generated within the quadrupole ion trap through laser desorption (with the sample held at or near the ring electrode surface) would be expected to correlate well with the behavior described for ion injection. It is interesting to review the experimental observations made by Vargas et al. (65) that there is an RF-phase-dependence for ions desorbed with high values of q, which is less apparent at low values of q. From Figure 3-10 it is apparent that only for a very narrow range of RF phases will an ion generated near an electrode be collected and stored within the quadrupole ion trap, whereas at lower values of q (Figures 3-8, 3-9) the positional acceptance of the quadrupole ion trap increases, thereby increasing the probability that an injected ion may have enough energy removed through collisions and resonance damping that its phase-space ellipse will be enveloped by that calculated based on the limits of the quadrupole ion trap electrodes. Note that the shapes of the phase space ellipses for the r and z direction are identical as a function of q_u, the maximum velocities are scaled by the radius of the hyperbolic surface of the electrode.

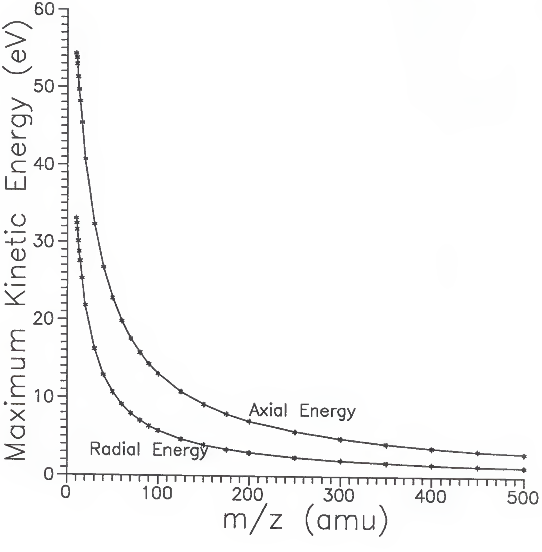

Figure 3-12: Maximum ion kinetic energies as a function of mass for ions stored in a quadrupole ion trap with RF voltage set to correspond with m_{cutoff} of 10 amu.

Conclusions

The utility of computer simulations was demonstrated in this chapter. A summary of the Hyperlon program was presented, including a list of features and some notes on converting the data which are available from that program into information which has physical significance. It is hoped that there is enough information presented in this chapter to allow future researchers to use the methods available through the Hyperlon program to further characterize the operation of the quadrupole ion trap.

Data extracted from Wuerker's classic photograph of an aluminum microparticle were modeled via numerical integration of the Mathieu equation, providing further evidence that the statement attributing high frequency ripple seen in the photograph to superposition of the RF drive frequency is in error. The evidence provided in this chapter combined with the simple analysis of analytical solution of the Mathieu equation gives this author great confidence in correcting this erroneous statement which continues to be cited in the literature.

The plate capacitor model for resonance excitation was modeled via Hyperlon, and was validated via comparison with results published in the literature. The fluence required for ion ejection and maximum kinetic energy were calculated for m/z 134 as a function of the Mathieu parameter q. Using these results, the competition between ion ejection and collision-induced dissociation was explained, and axial modulation was predicted to be most effective at very low and very high values of q ($0.2 < q$ and $q > 0.85$). Additional work is required to help further rationalize the cause for the much reduced fluence at very large values of q, perhaps in the verification of the proposal that it is the radius of the phase space center acceptance ellipse that is important in the estimation of fluence.

The ability of resonance excitation to decelerate ions, effectively damping ion motion into the center of the ion trap, was identified. Such an effect may be quite useful for improving collection efficiency for injected ions. Unfortunately, once an ion is damped to the center of the quadrupole ion trap by resonance excitation, subsequent application of the excitation voltage will result in increasing the magnitude of the ion excursions and hence increase its kinetic energy. A recent paper demonstrated the effects of using dipolar resonance excitation during ion injection (66). It is interesting to note that hexapolar and octopolar resonances could exhibit similar deceleration capabilities, with the added advantage that the magnitude of the excitation field decreases dramatically as the ion is damped to the center of the ion trap. Thus it may be predicted that nonlinear resonances due to higher order fields may increase the probability of trapping certain ions which are injected such that their trajectories are out of phase with the nonlinear resonance field. One could also envision a system in which the phase of the applied dipolar resonance excitation voltage is reversed at a period calculated from the fluence required for ejection. In such a system, it may be possible to increase the probability of internalizing ion kinetic energy by allowing for much longer residence times. Such a system would be invaluable if it would allow for more energetic fragmentation pathways at lower values of q, which have an inherent advantage in daughter ion mass range.

Methodology for the calculation of and interpretation of phase-space diagrams was presented, and it was predicted that ion injection collection efficiency will be maximum for low kinetic energy of injected ions (a few eV). Collection of injected ions is dependent upon the ability of some decelerating force (either resonant deceleration, or scattering due to collisions with neutral molecules) to reduce either ion axial kinetic energy or ion axial position to scale that ion's phase-space ellipses such that they are enveloped by the theoretical phase-space acceptance ellipse assuming a maximum excursion corresponding to the electrode radius. The RF phase dependence of ion injection and laser desorption is predicted, with the phase dependence predicted to be greatest at high values of q.

CHAPTER 4
SIMULATION AND EXPERIMENTAL CHARACTERIZATION OF ELECTRON ENERGY IN A QUADRUPOLE ION TRAP

Introduction

In this chapter, results from the calculations of the trajectories of electrons injected into the quadrupole ion trap are presented. Trajectory calculations were performed for a variety of experimental conditions with such parameters as residence time, distance traveled, and electron kinetic energy recorded as a function of initial RF phase. Model results are presented which demonstrate maximum and average electron kinetic energy, electron transit time and electron path length as a function of RF phase angle. The effect of initial angle of incidence on electron energy is presented, and the lifetime and path length of injected low-energy electrons is explored. Some generalizations are presented which allow for rapid calculation of electron energy as a function of RF and DC voltage and RF phase angle. Experimental results are presented which support the conclusions predicted through theory and simulation of electron injection. The contribution of charge exchange reactions to ionization energetics is explored experimentally and through simulations.

Electron Ionization

Electron ionization (EI) of a gaseous sample with electrons having a nominal 70 eV of kinetic energy results in a 'classical' EI mass spectrum with reproducible fragmentation patterns. Indeed, the reproducibility of these fragmentation patterns allows comparison of mass spectra from widely varying instrument types in the form of a library. By comparing the spectrum of an unknown compound with a library of spectra of known compounds, such as the NIST library (67), one can often positively identify an unknown compound.

It is generally held that for most organic compounds, fragmentation patterns are similar for ionization with electron energies greater than 30 - 35 eV (68). With electron energy less than 30 eV, the relative abundance of the molecular ion $M^{+\cdot}$ tends to be enhanced as are the abundances of fragment ions arising from less energetic fragmentation pathways.

Electron-Capture Negative Chemical Ionization

Mass analysis of negative ions has been demonstrated as an extremely sensitive technique under electron-capture negative chemical ionization (ECNCI) conditions (69). A number of different types of reactions of neutral molecules with thermal electrons are possible, including ion pair formation, electron attachment, and dissociative electron attachment (69). Electron attachment (or electron-capture) ionization can be an especially sensitive ionization technique for molecules with high electron affinities (69).

In a conventional ECNCI ion source, a high pressure (fraction of a torr to torr range) of a bath gas is used to slow high energy electrons, resulting in electrons with near-thermal energies (a few eV or less). These near-thermal electrons react either with analyte molecules or with the bath gas, which generally has a partial pressure orders of magnitude greater than that of the analyte. If the electron reacts with the analyte directly through electron attachment, there is generally little excess energy and thus little fragmentation; the ion signal is concentrated into the molecular ion (typically $M^{-\cdot}$). Negatively charged reagent ions formed from the bath gas can give rise to analyte ions (typically by proton abstraction to form $[M-H]^-$ ions by a variety of pathways (69).

Negative chemical ionization has been demonstrated using the quadrupole ion trap (70, 71, 72, 73, 74). However, sensitivities have not proven comparable to sensitivities for the same compounds analyzed using conventional ion sources. There are a few explanations for this poor sensitivity. First, it has been thought that there is a lack of thermal electrons to be captured. While dissociative electron-capture occurs readily under quadrupole ion trap conditions, the number of reagent ions formed is significantly smaller than the number of reagent ions for positive chemical ionization. There is also the issue of positive ion / negative ion recombination reactions which pose problems since the number of positive ions is generally so much larger than the number of negative ions. Under ionization conditions where negative ions are stored exclusive of positive ions, the phase space acceptance conditions are predicted to be so restrictive as to severely limit the probability of storage of any negative ions formed (low pseudopotential well depth in either the r or z direction). The work of Mather and Todd (70) is significant in that it demonstrates simultaneous detection of both positive and negative ions using Dawson's pulse-out ejection technique.

Electron Energy

The calculation of electron energy for electrons travelling from a heated filament into a conventional ion source is straightforward. Electron energy is taken as the potential difference between the filament and the ionizing volume. Errors common to such a calculation include the potential drop across a heated filament, and the field gradient inside an ionizing volume caused by a repeller or extraction voltage. For most purposes these errors can be neglected for electron energies above 30-35 eV.

The calculation of electron energy for electrons traveling from a heated filament into an electrodynamic (RF and DC) ionizing region such as a quadrupole ion trap is not as simple. In the ion trap, only ions above a certain RF- and DC-dependent threshold low-mass cutoff have stable trajectories. Ions lighter than this low-mass cutoff have small but finite residence times within the ion trap before they are ejected. These residence times can range from multiple RF cycles for ions of mass slightly below the cutoff level, to fractions of an RF cycle for ions of significantly lower mass. Electrons, with a mass 2000 times lower than that of a proton, clearly fall below the low-mass cutoff, and should have very short residence times. As such, there is a range of electron kinetic energies which is dependent upon the phase angle of the RF field during the time of electron transit (73, 50, 58). Harden and Wagner (75) demonstrated experimentally with an electrodynamic quadrupole trapping field operated using Dawson's pulse-out detection, that electron ionization of analyte molecules occurs only during a narrow range of RF phase angles centered around a phase angle of zero.

Simulation Studies

Experimental Conditions for Simulation Studies

The BASIC computer program Hyperlon was used to calculate the trajectories for electrons injected into a quadrupole ion trap. Minor modifications to the program were made to account for the various initial conditions for these electron trajectory calculations. The mass-to-charge ratio of an electron was taken as 0.0005 amu with a negative charge. Injected electrons were modeled as electrons spontaneously created at a position on the surface of an endcap electrode, starting at the radial center. Electrons were assumed to have initial kinetic energy of 12.5 eV (the typical filament to endcap potential difference in the Finnigan ITMS) directed into the ion trap with an initial angle of divergence of 20^0 from perpendicular. The Mathieu equation of motion was solved for this very light ion using a fourth-order Runge-Kutta algorithm with a constant phase increment of 0.001^0 of RF phase angle. Ion trap dimensions and operating conditions were taken as that of a Finnigan MAT ITMS: r_0=1.0 cm, 1.1 MHz drive frequency, all voltages applied to the ring electrode, with grounded endcaps. An ideal ratio of ring radius to endcaps radius was assumed in the model; however, the energy results may be scaled by a factor of 1.11 to correct for the recently disclosed stretched electrode geometry (5).

Note that this model includes the assumption that the electron is able to pass through the holes in the endcap into the trap at all RF phase angles. This neglects any penetration of the RF field into the electron gun assembly which may prevent electrons from making it into the ion trap at certain phases of RF voltage. Thus electrons which are calculated to penetrate only slightly into the trap have little significance, and should be ignored (where the electrons have both low average kinetic energies and short residence times), since such electrons are not expected to result in significant ionization; furthermore, ions formed so close to the endcap electrodes are unlikely to be efficiently stored (see phase-space acceptance ellipse discussion in Chapter 3). For cases where calculated residence times are long, it is assumed that such electrons may contribute significantly to ionization in the ion trap.

Figure 4-1 is an overlay of two Mathieu stability diagrams plotted as a function of RF and DC voltages (V-U space) for positive and negative ions of mass 17. Electron injection was modeled for three operating points in these two stability diagrams. Point

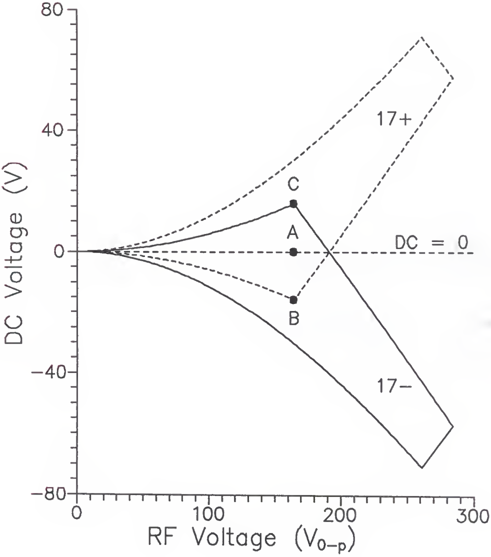

Figure 4-1: Mathieu stability diagrams for the positive and negative ions of m/z 17 plotted in RF-DC space. Point A corresponds to 164.1 volts RF, and 0 volts DC. Points B and C correspond to 164.1 volts RF with -/+ 15.8 volts DC.

A represents RF-only operation of an ion trap with a low-mass cutoff of 14.6 amu. This operating point is typical for operation of the ion trap during electron ionization with good sensitivity. In addition, this RF voltage corresponds to the operating points B and C (in which a DC potential is applied in addition to the RF potential). Point B represents selective mass storage operation of the ion trap at the a=0.15, q=0.78 tip of the stability diagram for a positive ion of m/z 17. Using a DC voltage more negative than this value results in exclusive storage of negative ions, with all positive ions having unstable trajectories. Using a DC voltage slightly less negative than this value results in selected mass storage of a narrow range of positive masses, in this case centered around the m/z 17 positive ion. Point C represents selective mass storage operation of the ion trap at the same a,q point on the stability diagram as in Point B, but for m/z 17 negative ions.

Simulation Studies Results and Discussion

Based on simulations, typical electron transit times through the quadrupole ion trap are on the order of nanoseconds to tens of nanoseconds, as will be demonstrated in a later section. With a drive frequency of 1.1 MHz, and thus a period of 909 nanoseconds, a given electron will only survive a fraction of a complete RF cycle. As such, it is interesting to examine electron trajectories as a function of RF phase angle at the time of injection. The results from a series of simulated RF phase-synchronized electron injection experiments is presented below.

Figure 4-2 is an example of three calculated electron trajectories for electrons with initial RF phase angles of 0^0, 90^0, and 180^0. Experimental conditions are RF-only operation with a low-mass cutoff of 20 amu, and an initial electron energy of 12.5 eV. Initial angle of incidence is 20^0 relative to a perpendicular. As noted previously, at an RF

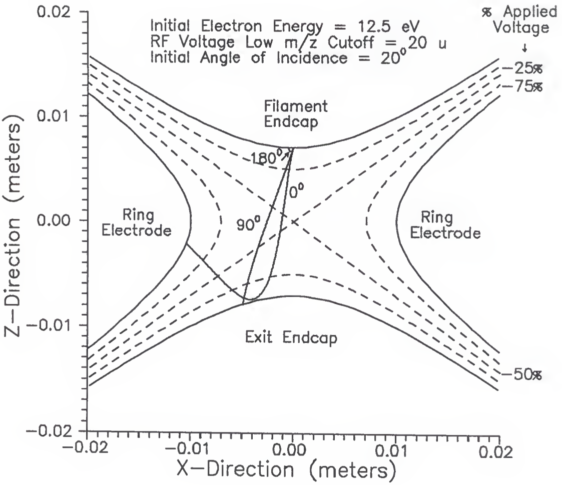

Figure 4-2: Electron trajectories corresponding to initial RF phases of 0, 90, and 180 degrees.

phase angle of 180^0, it is doubtful that a 12.5 eV electron would travel even the short distance demonstrated in this figure. Equipotential contours included in this figure may be interpreted to represent the ring electrode potential contribution to instantaneous kinetic energy of the electron. Instantaneous electron kinetic energy equals initial electron kinetic energy plus instantaneous ring electrode potential.

The physics of the quadrupole ion trap is based on a quadrupolar field gradient between three electrodes. For the case of grounded endcap electrodes (as in the Finnigan ITMS), the RF voltage applied to the ring electrode must be doubled to achieve the same electric field as the case where equal voltages of opposite polarity are applied to the ring and endcap electrodes. For the grounded endcap case, the absolute center of the ion trap is at a potential exactly half the potential of the ring electrode as shown by the equipotential contours in Figure 4-2. Thus an electron passing from one endcap through the exact center of the ion trap to the other endcap will have its kinetic energy increase to its maximum value at the center of the ion trap. After passing through the center of the ion trap, the electron kinetic energy will decrease back to its entrance value. The maximum kinetic energy for such an electron will be its initial kinetic energy added to one half of the instantaneous potential applied to the ring electrode. For the case where electrons have a non-zero angle of incidence (i.e. electrons are injected towards the ring), and either an extremely small initial kinetic energy, or an extremely large ring potential (thousands of volts), the electron will travel from the entrance endcap to strike the ring, with a maximum kinetic energy equal to the potential difference between the two electrodes. With grounded endcap electrodes, this potential difference is equal to the applied ring potential. Assuming that maximum kinetic energy corresponds to an electron striking the ring electrode, the phase-dependent maximum kinetic energy can be approximated by the equation:

$$E_{e,max}=(V_{DC}+V_{0\text{-}p}\cos\Theta)+E_{e,init} \tag{4.1}$$

Figure 4-3 demonstrates the effect of entrance angle on trajectory path for 12.5 eV electrons injected into an RF-only ion trap with a low-mass cutoff of 20 amu. Even with an entrance angle tangential to the endcap (90^0), electrons are directed by the strong electric field toward the center of the ion trap.

As noted in the introductory paragraphs of this chapter, the kinetic energy of ionizing electrons is an important factor for controlling ion fragmentation. Figure 4-4 presents plots of the RF phase-dependence of the maximum instantaneous energy and the average kinetic energy of an electron injected into a quadrupole ion trap under the same conditions as in Figure 4-2. Electrons injected during RF phase angles which correspond to negative potentials applied to the ring are decelerated and reflected back into the entrance endcap, as shown in Figure 4-2. Electrons which are injected at RF phase angles which correspond to positive potentials applied to the ring electrode are accelerated to an energy which is a fraction of the applied potential. For positive voltage RF phase angles (-90^0 to $+90^0$), the data in Figure 4-4 suggest that average kinetic energy for electrons injected at a given RF phase angle can be approximated as one third of the maximum kinetic energy. For the RF phase angle of zero (maximum RF potential) the fraction of average electron energy due to the ring electrode potential corresponds to 31.66 % of the instantaneous applied voltage (with the initial kinetic energy of 12.5 ev subtracted from each value prior to division). Note that maximum kinetic energy for those RF phases centered around 0^0 represent electrons striking the ring electrode (see Figure

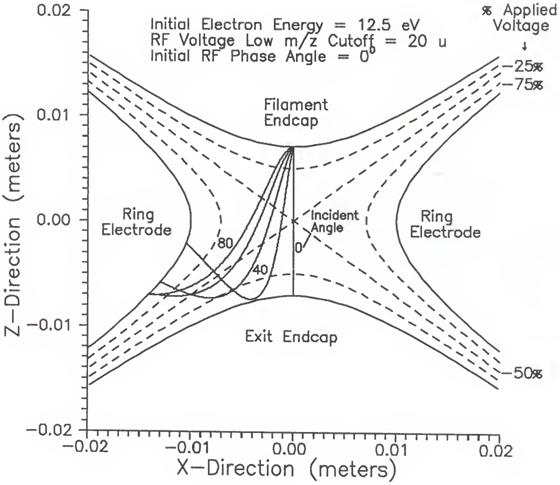

Figure 4-3: Electron trajectories for electrons with initial incidence angles of 0, 20, 40, 60, and 80 degrees.

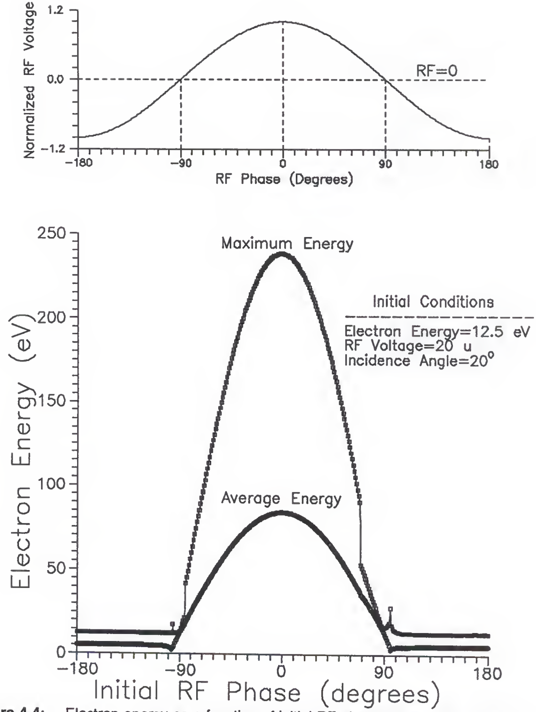

Figure 4-4: Electron energy as a function of initial RF phase angle. Initial electron energy is 12.5 eV. The inset identifies normalized RF voltage as a function of RF phase.

4-2). As most of the distance traveled is between the two endcaps, the average electron energy is strongly weighted by the trajectory through these lower-potential volumes of the quadrupole ion trap. Because ions generated very near the ring electrode will not be effectively stored due to poor phase space acceptance, the maximum effective energy corresponds to electrons traveling through or near the center of the ion trap, with a maximum energy of fifty to sixty percent of the applied ring potential. Since the electron spends significant time traveling through lower potential fields near the endcaps, the average electron energy is expected to be much smaller than the maximum electron energy.

Maximum kinetic energies for electrons injected with RF-only, RF with negative DC, and RF with positive DC voltages applied to the ring are plotted as a function of initial RF phase angle in Figure 4-5. The are labeled as A, B, and C respectively, with the labels corresponding to the operating points on the stability diagrams in figure 4-1. Curve A is the same curve shown in Figure 4-4. Note that the general shape of these curves remains the same; they are only scaled differently based on the magnitude of the RF and DC voltages. Note that the transitions in each of the curves is due to the ions hitting either the endcap electrodes or the ring electrode. The indicated kinetic energies for these transition step jumps correspond to the electrode reaching either one-half or the full ring potential.

Electron energies were calculated as a function of RF and DC potentials, for electrons injected at zero degree RF phase angle and 20 degree incident injection angle, with ring RF and DC voltages corresponding to operating lines passing through points A, B, and C (no DC, -DC, and +DC, respectively) shown in Figure 4-1. These maximum kinetic energies are shown in Figure 4-6. It is interesting to note that these plots

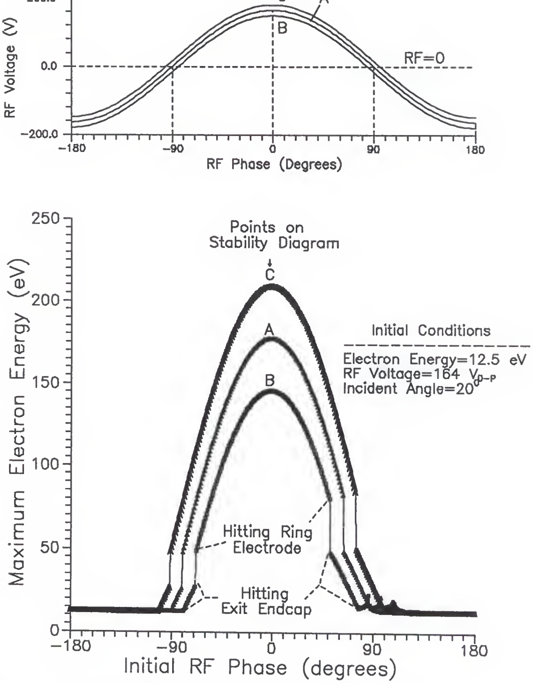

Figure 4-5: Maximum electron energy as a function of initial RF phase angle for electrons injected at RF and DC voltages for points A, B, and C in Figure 4-1. The inset identifies normalized RF voltage as a function of RF phase.

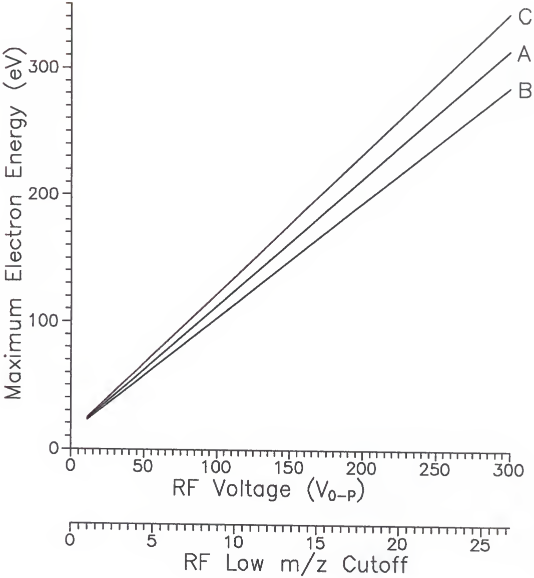

Figure 4-6: Electron energy as a function of RF voltage low-mass cutoff for scan lines which pass through the origin of Figure 4-1 and through each of points A, B, and C. Initial electron energy is 12.5 eV.

approximate straight lines. Since the maximum kinetic energy corresponds to an RF phase angle of zero, equation 4.1 reduces to:

$$E_{e,max}=k(V_{DC}+V_{0\text{-}p})+E_{e,init} \quad \textbf{(4.2)}$$

where k is a constant which represents the maximum fraction of the ring potential which an ion sees during its trajectory, typically 0.5 to 0.6. It is comforting to observe that as the applied DC voltage is made more positive the maximum electron energy increases accordingly.

The effect of initial RF phase angle on path length for electrons injected into the quadrupole ion trap under RF-only conditions (point A of Figure 4-1) is plotted in Figure 4-7. Electrons injected at an initial incident angle of 20^0 from perpendicular which are attributed to striking an endcap electrode under positive ring RF phase angles travel a 1.7 cm arc from the center of one endcap to the edge of the other. The distance from endcap to endcap of a quadrupole ion trap in these simulations was taken as 1.414 cm. Longer trajectory distances observed at the incident RF phase angles of -95^0 and $+95^0$ correspond to electrons which travel through the ion trap when the RF potential approximates the filament potential. These electrons travel through the trap with very low (near thermal) kinetic energy, and exit the ion trap volume between the ring electrode and exit endcap electrode. The path lengths for those electrons injected under RF phases which correspond to negative instantaneous RF voltages are small because they are reflected back to the entrance endcap by the strong negative electric field.

Also plotted in Figure 4-7 are electron transit times as a function of initial RF phase. For negative voltage RF phase angles, low-energy electrons are simply decelerated and deflected back to the entrance endcap. For positive voltage RF phase

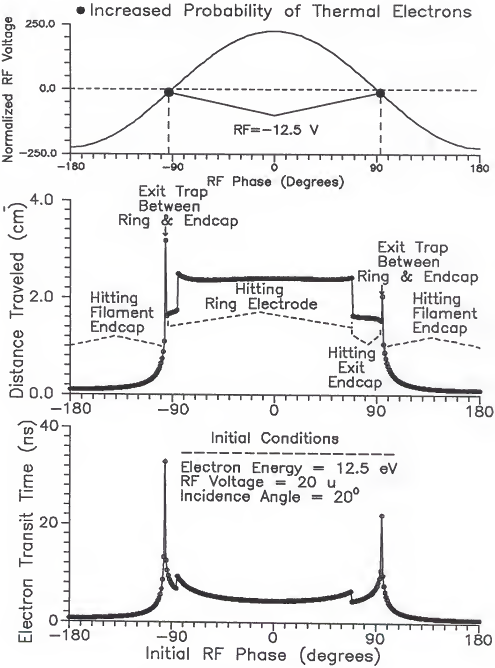

Figure 4-7: Electron transit time and distance traveled as a function of the initial RF phase angle. Inset identifies normalized RF voltage as a function of RF phase.

angles, high-energy electrons are transferred through the hyperbolic field to the ring or the opposite endcap. Division of distance traveled by transit time yields average electron kinetic energy (as shown in Figure 4-4). For electrons injected near the zero crossings of the cosine function (more specifically, at applied RF voltage equal to the filament potential of -12.5 Volts), electron transit times are especially long, as nominally 12.5 eV electrons are decelerated to near-thermal energies and travel through an essentially field-free region. It is at these "field-free" RF phases where the possibility may exist for injection and transmission of near-thermal electrons into a quadrupole ion trap. Note that the RF voltage does change slightly during the course of these long electron transit times (tens of nanoseconds). The phase angles which exhibit long transit times (near -90^0 and $+90^0$) have differing path lengths due to the fact that as the RF voltage goes from negative to positive, electrons are accelerated slightly toward the ring electrode, and strike the endcap electrode further from the center of the endcap electrode than the case when the RF voltage goes from positive to negative (effectively pushing the electron beam closer to the center of the trap, away from the ring electrode).

It is therefore predicted that low-energy electrons can exist within the ion trap, thus providing the potential for electron capture chemical ionization.

Calculated Residence Time of Helium Ions

Ionization RF levels are generally set in the ion trap with a low mass cutoff high enough that helium ions have unstable trajectories. Although trajectories of helium ions generated within the quadrupole ion trap are unbounded, helium ions do have a finite lifetime within the quadrupole ion trap between formation and ejection in the 'z' direction. At typical ionization RF potentials, helium ions have stable trajectories in the 'r' direction.

A typical trajectory for a helium ion generated near the geometric center of the ion trap is shown in Figure 4-8. In this example, the helium ion residence time is 1.61 μs, from ion formation to ion ejection. Initial RF phase angle was 0^0. For all initial phase angles, the helium residence time ranged from 1 to 2 ns. Experimental conditions for these simulations were: m/z 4 , RF phase increment 0.2^0, initial 'z' position 0.000001 m from center, zero initial 'z' velocity, RF voltage corresponded to a low mass cut-off of 10 amu (assuming stretched trap geometry).

It would be expected that at the extremely high partial pressures of helium used in normal operation of a quadrupole ion trap (approximately one millitorr) helium charge exchange should contribute significantly to ionization in addition to electron ionization. The net effect of helium charge exchange would be an increase in the total number of ions formed with the additional charge exchange reaction product ions representing more energetic fragmentation pathways due to the large ionization potential of helium, 24.587 eV (76). Since helium charge exchange reactions supplement the results of reactions from electron ionization, the net result of helium charge is a net increase in total number of ions, with a net increase in the extent of fragmentation and therefore in apparent electron energy.

Laboratory Studies

Experimental Conditions for Laboratory Experiments

All laboratory experiments were performed using a Finnigan MAT ITMS quadrupole ion trap mass spectrometer. Reagents (perfluorotributylamine (PCR Chemicals, Gainesville, FL) and n-butylbenzene (Eastman Kodak, Rochester, NY)) and buffer gas (ultra high purity grade helium) were introduced into the ion trap chamber via Granville-

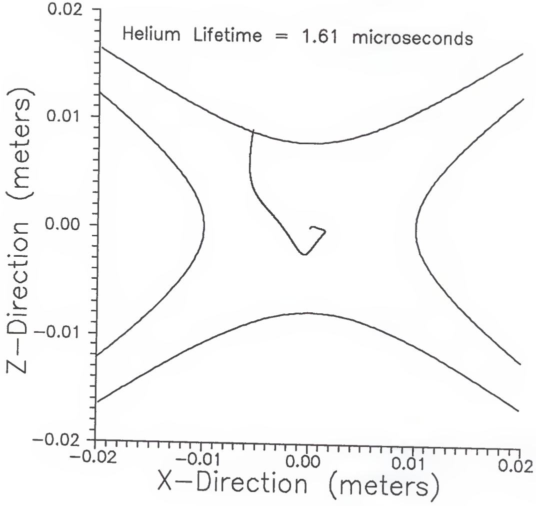

Figure 4-8: Helium ion (m/z 4) trajectory for an ion created near the geometric center of the ion trap. Initial conditions: 'x'= 0.000001 m, 'z'=0.00001 m, RF phase angle = 0°, RF voltage: 10 amu low mass cutoff.

Phillips variable leak valves. Reagent gas partial pressures were measured using a Bayard-Alpert type ionization gauge with nominal pressures presented uncorrected for ionization probabilities. FORTH user programs were used for automated sequential acquisition of spectra with the ionization RF voltage incremented between acquisitions.

Experimental Correlation of RF Voltage with Effective Electron Energy

The efficiency sensitivity of electron ionization as a function of electron energy is well characterized (77). A plot of EI cross section as a function of electron energy (Figure 9) for acetylene (77) exhibits a global maximum at around 100 eV with cross section rapidly approaching zero as electron energy approaches zero, and with a gradual decrease in cross section at higher electron energies. This curve shape with global maximum circa 80-100 eV is characteristic of most molecular gases ionized through electron ionization (77). As such, if the EI ion intensity for a given compound were measured as a function of ionization RF potential, the effective electron energy could be calibrated by overlaying this curve with the classical EI cross section curve, and matching the global maxima.

Figure 4-9 shows such a calibration (78). A plot of relative intensity of selected ions from n-butylbenzene as a function of applied RF potential is overlaid on a plot of ionization cross section as a function of electron energy (77).

Simulation results presented earlier in this chapter predict an average electron energy in eV which is approximately the initial electron energy in eV added to 31% of the applied ring potential. For a low mass cutoff of 16 amu, the simulation would predict an energy of (0.31 * 16 amu * 12.5 V_{0-p}/amu + 12.5 eV = 74.5 eV).

Based on the fit between the data in Figure 4-9, the relationship between effective electron energy and RF voltage applied during ionization is approximately 5-eV per amu

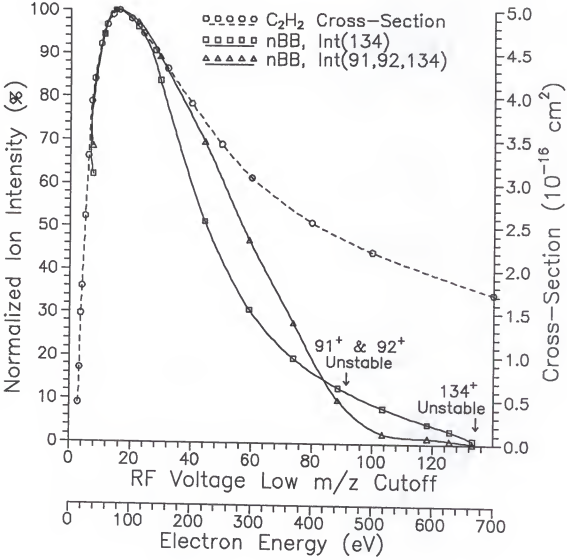

Figure 4-9: Normalized ion intensities of selected fragment ions of n-butylbenzene plotted along with ionization cross section data for a typical organic molecule (C_2H_2) (4-13).

of RF. For the case of 16 amu low mass cutoff, this model would predict an electron energy of (5 eV/amu * 16 amu = 80 eV), which correlates well with the simulation calculation.

Since laboratory experiments do not generally allow differentiation of RF phase angles, laboratory data represent the effective electron energy averaged across all RF phases. Since electrons are injected only during RF phase angles corresponding to positive potentials applied to the ring electrode, the shape of the curve of average kinetic energy as a function of RF phase (Figure 4-4) has the shape of a haversine. The average of a haversine function is $2/\pi$ * maximum (79).

Depending on initial angle of incidence, an electron injected into the quadrupole ion trap will strike either an endcap electrode or the ring electrode. The maximum electron kinetic energy will therefore be either half or equal to the potential applied to the ring electrode plus the initial electron kinetic energy.

Ions formed near the center of the ion trap have a higher likelihood of being stored than ions formed far from the center of the trap due to phase space acceptance. Electrons whose trajectories result in their ultimately striking the ring electrode spend a significant fraction of their transit time traveling through the center of the ion trap with kinetic energy just larger than initial energy plus half of the applied ring potential, as do electrons which ultimately strike an endcap electrode.

Assuming that the haversine is a reasonable approximation of the curve of maximum kinetic energy as a function of RF phase, the effective electron energy is predicted to be slightly larger than initial kinetic energy plus one half of the applied ring potential * $2/\pi$:

$$E_{effective}=\frac{(V_{DC}+\frac{2}{\pi}V_{0\text{-}p})}{2}+E_{e,init} \qquad (4.3)$$

Taking the example given earlier of a 12.5 eV electron injected into a quadrupole ion trap with RF voltage corresponding to a low mass cutoff of 16 amu:

$$E_{effective}=\frac{(0+\frac{2}{\pi}(16*12.5)}{2}+12.5=76eV \qquad (4.4)$$

The empirical fit of laboratory ion trap data to EI cross section data places the effective electron energy with an RF voltage set to a low mass cutoff of 16 amu at approximately 80 eV. The difference between these theoretically and empirically determined values can be attributed to the fact that the typical electron has a non-zero angle of incidence, and therefore does not travel through the geometric center of the trap (the 0.5 factor in equation 4.2). Rather, the typical electron will travel through the RF field with a maximum energy between 0.5 and 1 times the potential applied to the ring electrode. Another consideration is an assumption inherent in the use of the haversine average approximation; clearly ionization efficiency varies as a function of electron energy, yet electron energies which may not yield ionization are included in the average of the haversine, resulting in an underestimation of the effective energy. Regardless of the source of the underestimation, from the fit of the curves in Figure 4-9, the empirically determined maximum electron energy factor is slightly more than the predicted 0.5. Note that the cross section data are representative of the trend in cross section as a function of electron energy, but were measured using a different organic molecule. The conclusions made here can therefore only infer an approximate relationship between the two data sets.

Recent work by J. R. Simms and R. J. Strife (80) demonstrates that ion trap sensitivity reduces dramatically for ionization RF voltages below 8 amu cutoff. Using equation 4.4, this corresponds to an effective electron energy of 43.5 eV. From the curve in Figure 4-9, it is predicted that as electron energy tends toward zero, so does sensitivity. The experimental results presented in Figure 4-9 may help explain the results reported by Simms and Strife. Additional effects which may explain the loss in sensitivity at low RF trapping voltages are the shallow pseudo-potential wells and corresponding inefficient ion storage which accompany low voltage operation of the ion trap, compounded by the one amu pre-scan built into the analytical scan segment of the Finnigan ITMS software. The ring RF voltage is set to a voltage corresponding to one amu smaller than the first mass selected for the scan immediately prior to the analytical scan.

Experimental Evidence for Electron-Capture Negative Chemical Ionization

From simulation studies, it is predicted that under EI conditions, a certain small percentage of RF phase corresponds to conditions in which low-energy electrons exist within the ion trap. With the possibility of low-energy electrons comes the possibility of negative ions. Under certain conditions of RF and DC voltages, these negative ions could theoretically co-exist with positive ions, however the potential for their co-existence is generally dismissed due to the large rate constants associated with positive ion negative ion recombination reactions. In contrast, work by Mather and Todd (70) previously demonstrated simultaneous detection of both positive and negative ions extracted from a quadrupole ion trap.

Work in our lab has confirmed this earlier work of Mather and Todd, demonstrating that using typical ionization conditions it is indeed possible to store and subsequently detect positive and negative ions simultaneously in the same scan (32, 45). The laboratory data which demonstrate simultaneous acquisition of positive and negative ions of perfluorotributylamine are shown in Figures 4-10 thru 4-12.

Figure 4-10 contains sections of stability diagrams for positive ions m/z 414, 614, and negative ions m/z 452, and 633 (78). In this set of experiments, the RF voltage was set to a low mass cutoff of 10 amu during ionization, and subsequently ramped to 270 amu. A series of scans was acquired with various DC voltage pulses applied to the ring electrode with an RF voltage set to a voltage which corresponds to a 270 amu low mass cutoff. The stability diagrams in this figure are scaled to theoretical ion trap dimensions, and are not corrected for the recently revealed stretched trap geometry.

The experimentally determined stability limits are identified in Figure 10 using uncalibrated DC voltages. The deviation from the theoretical stability diagram boundaries is attributed to stretched geometry trap which would result in an 11% increase in DC potential over the theoretical geometry, and the calibration of the DC power supply (which has a non-unity slope on a plot of requested versus actual voltage).

Figure 4-11 shows the measured intensities of the ions identified in Figure 4-10 plotted as a function of DC voltage, corresponding to the scan line noted in the previous figure. Notable in this figure is the demonstration of a range of voltages in which positive and negative ions coexist in the ion trap. Individual spectra are presented in Figure 4-12; these spectra correspond to the DC voltage positions indicated in Figure 4-11. Positive

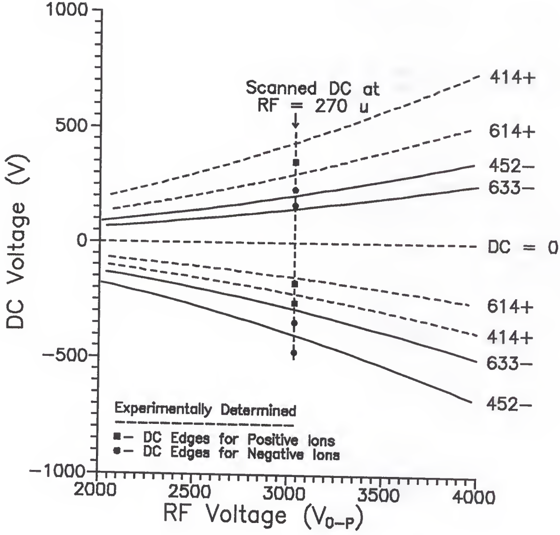

Figure 4-10: Theoretical stability diagrams for positive and negative ions of perfluorotributylamine with experimentally determined boundaries.

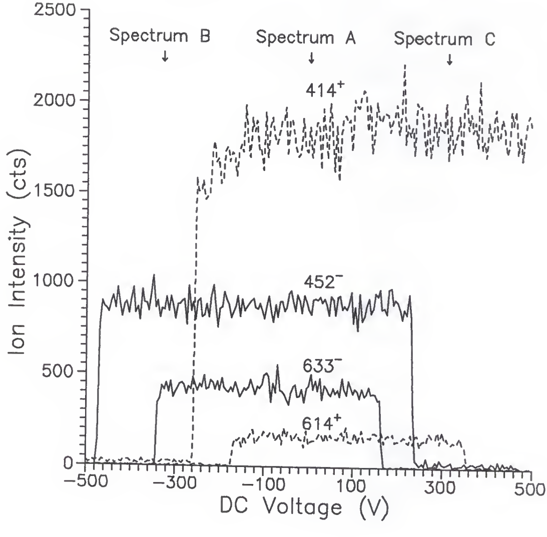

Figure 4-11: Positive and negative ions of perfluorotributylamine plotted as a function of DC voltage applied to the ring electrode just prior to the analytical scan, with RF voltage set to a low mass cutoff of 270 amu.

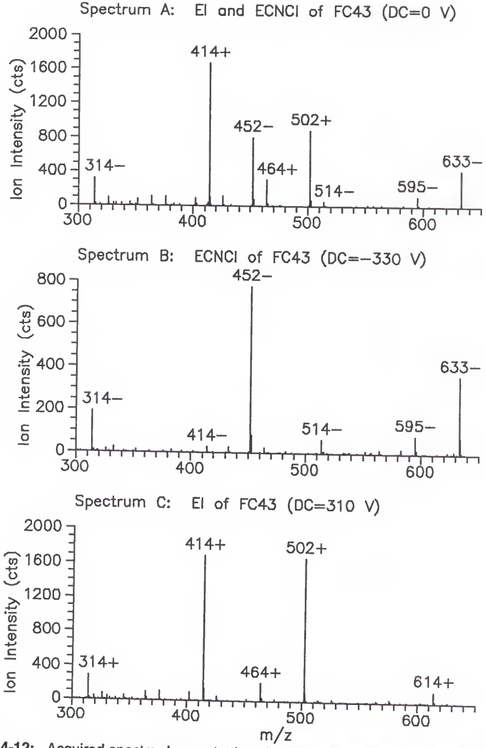

Figure 4-12: Acquired spectra demonstrating simultaneous storage and detection of positive and negative ions of perfluorotributylamine. Spectra correspond to points indicated in Figure 4-11.

ions can be differentiated from negative ions through analysis of Figure 4-11. The stability boundaries demonstrated through measurement of intensity with various DC voltages applied to the ring electrode have characteristic cutoffs. If the negative DC cutoff voltage is larger than the positive DC cutoff voltage, then that ion is identified as negative.

These results suggest the existence of low-energy electrons in the quadrupole ion trap. Note that perfluorotributylamine is a sensitive compound for electron capture negative chemical ionization owing to the large number, 27, of fluorine atoms in the molecule. The spectra in Figure 4-12 correspond to points A, B and C in Figure 4-1. Spectrum A in Figure 4-12 corresponds to RF-only operation, and contains both positive and negative ions. Spectrum B corresponds to exclusive storage of negative ions effected through the application of -330 volts DC to the ring electrode. Spectrum C corresponds to exclusive storage of positive ions, effected through application of a large positive DC voltage (+310 volts) during the DC isolation step of the scan function. Note that ions exiting the ion trap through mass selective instability mode ejection have ion energies measured in thousands of electron volts (kinetic energies must be larger than the pseudopotential well depth to escape the trapping field, see Chapter 2). Ion energies this large allow negative ions to strike the detector in spite of the large negative bias (typically 1000 to 2000 volts) applied to the front of the detector.

Contributions of Charge Exchange to Electron Ionization in a Quadrupole Ion Trap

As stated previously, although helium ions are theoretically unstable under normal operating conditions of the quadrupole trap, simulations indicate that they do have a finite residence time (1 to 2 μs). In addition, the high ionization potential of helium relative to the nominal 12.5 V filament potential suggests that helium will not be ionized except by electrons accelerated by the trapping field inside the quadrupole ion trap. It is predicted that at low partial pressures of helium, charge exchange reactions of these few, rapidly ejected helium ions with sample molecules would have negligible effects on electron ionization mass spectra. However, under normal ion trap operating conditions, the partial pressure of helium is maintained at approximately a millitorr, typically a 10,000 to 100,000-fold excess over the partial pressure of analyte molecules. With such a large excess of helium in the trap, it is likely that far more helium ions than analyte ions will initially be formed by EI, even with their short residence times. The contributions of helium charge exchange to electron ionization spectra are expected to be appreciable. N-butylbenzene was used as a probe molecule to characterize the contributions of charge exchange reactions to the energetics of electron ionization spectra (32). N-butylbenzene was chosen because its energetics and fragmentation pathways are well characterized.(81, 82, 83).

Fragmentation of the molecular ion of n-butylbenzene (m/z 134) can occur through a number of competitive pathways, most notably to form the tropylium ion ($C_7H_7^+$, m/z 91) and the tolulyl ion ($C_6H_5CH_2^+$, m/z 92). While the tropylium ion is more stable, it has a higher energy barrier for formation than the benzyl ion. The ratio of the intensities of these two ions is often used as a measure of the energetics of the reaction that led to fragmentation. A large ratio of m/z 91 to m/z 92 indicates a high energy dissociation reaction (82, 83).

The ratio of the intensities of m/z 91 to m/z 92 of n-butylbenzene under EI conditions in a quadrupole mass filter is approximately 1.5 with electron energy in the 40-70 eV range (32). Figure 4-13 contains plots of the m/z 91 to m/z 92 ratio measured at various helium buffer gas pressures, with and without the ejection of the positive molecular

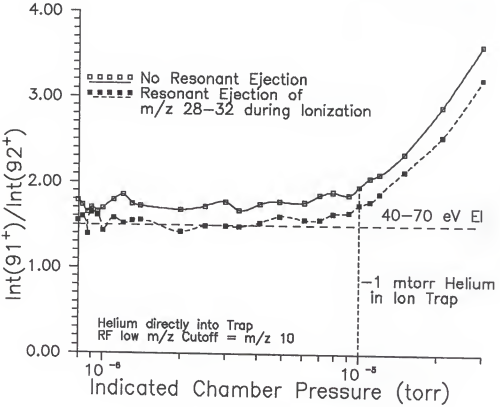

Figure 4-13: Effect of helium, nitrogen, and oxygen charge exchange on apparent energetics of electron ionization of n-butylbenzene.

ions of nitrogen and oxygen (m/z 28 and 32). The ring RF voltage in these experiments was set such that the lowest mass stably stored was 10 amu. No DC voltages were applied in these experiments.

The exclusion of m/z's 28 and 32 was effected through resonance ejection during ionization, using a 6000 mV 130 kHz sine wave which was applied across the endcap electrodes. Note that at the experimental RF voltage, this frequency corresponds to m/z 30. With a large amplitude excitation voltage, the mass resolution of resonance ejection is such that ions as far as two amu away from the selected ion (i.e. m/z's 28 and 32) are ejected. Note that helium pressure is reported as indicated chamber pressure. Since helium was leaked directly in to the quadrupole ion trap, this indicated pressure is approximately a factor of 10 low, as calibrated in our lab (64). In addition, the ionization probability of helium is approximately one seventh that of nitrogen (76)(the gas for which the ionization gauge was calibrated).

It is apparent from this figure that at the typical helium pressure of one millitorr there is some reaction of analyte molecules or ions with helium, including helium charge exchange. This effect is seen to slightly increase the apparent energy imparted to the neutral molecule. At pressures much larger than one millitorr this enhancement in apparent energy is dramatic.

A more important conclusion which can be extracted from Figure 4-13 is the fact that charge exchange ionization of neutrals by ubiquitous air gases (nitrogen and oxygen) also significantly affects the apparent energy of ionization. Nitrogen and oxygen have ionization energies of 15.576 and 12.063 eV respectively (76). This small increase in energy available for ionization should not significantly affect qualitative or quantitative operation of the quadrupole ion trap. For cases where these contributions may be significant, the ions can be ejected through resonance ejection, as has been employed in obtaining the data in Figure 4-13. Note that an alternative method of excluding these charge exchange by increasing the ionization RF voltage to a low mass cutoff above m/z 32 would adversely affect sensitivity, as shown in the previous section.

Conclusions and Future Work

In this chapter, the energetics of ionization through electron injection into the quadrupole ion trap were examined under a variety of simulated and experimental conditions. Results predicted through simulation and basic theory were correlated with results of laboratory experiments.

Electrons are injected into the quadrupole ion trap only during a range of RF voltages centered around a phase angle of zero (assuming a cosine function). Typical electron transit times range from a few nanoseconds to tens of nanoseconds.

Maximum electron kinetic energy can be calculated as a function of RF phase using equation 4.1. Inherent in this equation is the assumption that the magnitude of the applied voltage does not change through the course of the electron transit time. This is a reasonable assumption since the transit times represent small fractions of the RF period.

If the kinetic energies due to the electron striking the ring electrode are neglected due to poor phase space acceptance of newly formed ions, and instead the assumption is made that the maximum effective kinetic energy is associated with the electrons traveling near the geometric center of the quadrupole ion trap, equation 4.1 is converted to:

$$E_{e,max}=0.5\cdot(V_{DC}+V_{0\text{-}p}\cos\Theta)+E_{e,init} \qquad (4.5)$$

When one considers the fact that experimental results from the injection of electrons into the quadrupole ion trap do not differentiate the RF phase of injected electrons, and therefore represents the average of electron energies across all RF phases. The effective electron kinetic energy can be calculated as the average of the a haversine function using equation 4.4.

Note that these simplistic calculations assume that all electrons have equal probabilities of forming ions. Clearly this is not the case, as shown in Figure 4-9, which demonstrates the dependence of ionization cross section on electron energy. Regardless, this first-order approximation has been demonstrated to estimate effective electron energy, with a minor adjustment in the scaling of the applied potential. Knowing this relationship, the relative effects of RF and DC voltages on electron energy can be predicted a priori.

The occurrence of low-energy electrons and the formation of negative ions during EI ionization were predicted based on computer simulations. These predictions were confirmed experimentally using perfluorotributylamine as a probe molecule. Solving equation 4.5 for RF phase angle θ, given a set of RF and DC voltages, one could predict the optimum phase for injection of thermal ions. One could envision an experimental system optimized for RF phase synchronized injection of electrons. With suitable selection of phase angle, electrons could be gated into the ion trap for exclusive formation of negative ions, with electron energies never exceeding the threshold required for electron ionization. In such a system, it may be possible to store electrons emitted from the heated filament in the gate electrode region, with pulse injection of one RF cycle (900 ns) of electrons into the ion trap in a small fraction of an RF cycle. Such an integrating electron pulse should dramatically increase the sensitivity for electron-capture reactions.

The effect of charge exchange reactions on apparent electron energy was demonstrated experimentally, and simulations were performed to help explain the results. Based on the calculated residence time of helium ions of one to two microseconds, helium ions could be expected to contribute to charge exchange reactions during electron ionization. Charge exchange reactions were also attributed to the presence of nitrogen and oxygen ions during ionization. This work demonstrated that ionization energetics in the quadrupole ion trap can be significantly higher than would be expected based on calculations of electron kinetic energy. Note that spectra acquired using a GC/MS system equipped with a conventional EI ion source, operated with helium as a carrier gas, would be expected to exhibit similar increases in ionization energetics, due to charge-exchange with helium ions.

Future work in the characterization of electron energy in the quadrupole ion trap could include experiments using RF-phase-synchronized injection of thermal electrons to create negative ions by electron-capture ionization, and verification of electron energies as a function of RF phase for high-energy electron injection. Experimental verification of the calculated energies presented in this chapter would require an RF-phase triggered pulsing circuit similar to the one described by Dawson and Lambert (84). Using such a circuit, electrons could be gated through the Finnigan MAT ITD/ITMS electron gun assembly by applying a narrow (few nanoseconds) pulsed gating voltage to the gating lens. The experiments which could be performed using such a circuit include demonstration of electron-capture ionization, reproduction of the work of Harden (73) showing phase-dependence of electron injection, and electron ionization experiments showing RF-phase-angle-dependence of ion energy. Interpretation of results from the latter experiments may be complicated by variations in phase space acceptance of newly formed ions.

It would be interesting to perform some reaction rate calculations on helium charge exchange reactions in order to predict the number of charge exchange reactions which would occur at various helium pressures. Other future development ideas include correlation of phase-specific electron energies with phase space ellipses of newly formed ions. Other than some crude assumptions, the work in this chapter does not consider the probability of storage of any ion formed. It would be interesting to consider the energy of electrons only during the parts of trajectories which correspond to a high probability of forming an ion with a stable trajectory. Such a study would in effect focus on energy of electrons close to the geometric center of the ion trap, and neglect electrons with energies below some threshold energy level.

CHAPTER 5
OFF-AXIS ION INJECTION INTO A QUADRUPOLE ION TRAP WITH A QUADRUPOLE DEFLECTOR

Introduction

There are several options for sample introduction and ionization currently available for use with a quadrupole ion trap mass spectrometer (ITMS). Early sample introduction techniques include gas chromatography (GC), direct insertion probe, direct exposure probe, and direct leak. More recently, quadrupole ion traps have been coupled with liquid chromatography (LC) via particle beam, thermospray, and electrospray (85, 39, 86).

Ionization techniques for quadrupole ion traps can be divided into two separate groups: internal ionization and external ionization. Internal ionization in the ITMS generally consists of electron injection into the ion trap with electron ionization (EI), possibly followed by low pressure (10^{-5} torr) chemical ionization (CI). With internal ionization, ions are created within the trapping RF field, with a certain percentage of ions having suitable kinetic energies and positions to be trapped by the RF storage field. While great utility has been demonstrated using these internal ionization techniques in the ITMS, there are limitations to having only these techniques available. These limitations include poor compatibility with combined liquid chromatography/mass spectrometry (LC/MS), incompatibility with high-pressure electron-capture negative CI, atmospheric sampling ionization and desorption ionization methods such as fast atom bombardment (FAB).

There are many compounds which are too thermally labile to survive gas chromatographic sample introduction; liquid chromatography (LC) coupled with mass spectrometry has emerged as a common separation/detection technique for such compounds. The interfacing of a liquid chromatograph to the ITMS has generally required that ions be formed external to the ITMS analyzer, because the high flows of solvent exiting the LC/MS interface would typically be incompatible with ion trap operation. Particle beam is one LC interface which allows for sample enrichment without requiring significant gas loads, and thus has been successfully coupled directly with the quadrupole ion trap using an end cap electrode as a heated target with internal ionization (85, 87).

For certain compounds (those with high electron affinities), electron-capture negative chemical ionization (ECNCI) offers enormous increases in sensitivity compared to either EI or positive chemical ionization (PCI). High-pressure ECNCI is not compatible with electron injection into an ion trap; ECNCI requires thermal energy electrons, which represent only a small fraction of the electrons injected into the quadrupole ion trap, as shown in Chapter 4 of this work. With a conventional CI ion source, a relatively high gas pressure (1 torr) can be used to thermalize electrons which are then captured by sample molecules. The resulting negative ions can then be extracted through a small hole in the CI source and injected into an ion trap analyzer (37).

Direct atmospheric sampling devices create ions at or near the interface between atmosphere and high vacuum. Since these devices are by their nature external ion sources, their use with an ITMS requires some means of injecting ions into the trap instead of injecting electrons as is currently done.

Previous Work in Injection of Ions into a Quadrupole Ion Trap

At the 1987 meeting of the American Society of Mass Spectrometry and Allied Topics (1987 ASMS), John Louris and Graham Cooks of Purdue University presented the first spectra obtained by the injection of ions from an external EI source into a quadrupole ion trap analyzer (33). At the 1988 ASMS meeting, Jae Schwartz and Graham Cooks presented further results of their work (34), based on a three-month collaborative project at Finnigan Corporation in San Jose. Their injection system consisted of a line-of-sight three-tube Einzel lens to transfer ions from a Finnigan 3200 EI source through the filament endcap of a quadrupole ion trap analyzer. Ion gating was effected by pulsing the voltage applied to the center element of the Einzel lens injection system. They demonstrated the injection of both positive and negative ions from an EI source. Early problems of large amounts of baseline noise, presumably due to electrons or ions reaching the detector from outside the ion trap, were solved by using a magnet to collimate the electron beam inside the source. The kinetic energy of injected ions was varied from 10 to 60 eV. They observed a large amount of fragmentation in their spectra, presumably due to collision-induced dissociation (CID) of the ions during injection. They also determined that the presence of helium buffer gas inside the ion trap analyzer was essential for the collection of injected ions.

Keiji Asano, Scott McLuckey, and Gary Glish of Oak Ridge National Labs also presented ion injection results at the 1988 ASMS conference (35). This work included the combination of an atmospheric sampling glow discharge source, operating at conventional CI source pressures of about one torr, with an ion trap. A three-element lens system was used to inject ions through the filament endcap of the ion trap analyzer. The center element of this lens system consisted of two half plates; voltages were pulsed to these half plates to control the gating of ion injection. They demonstrated the injection of both positive and negative ions (anions) from this glow discharge source. One major problem which they mentioned in their presentations was the following: "Electrons are injected under the same conditions as anions, resulting in electron ionization within the trap. The positive ions formed in the trap can rapidly neutralize injected anions if they are allowed to accumulate."(35) The use of direct current (DC) voltages in conjunction with higher RF trapping levels during ionization helped alleviate this problem of positive ion/negative ion recombination. More recently, they have found that a magnet can be mounted within the ion source to prevent electron injection. They also noted that negative ion sensitivity was three orders of magnitude lower than positive ion sensitivity for nitro compounds for which negative ion sensitivity should have been much higher. Also presented was the observation that the trapping efficiency of injected positive ions increased dramatically with increased buffer gas pressure.

Earlier work by physicists Chun-Sing O and Hans A. Schuessler (88) of Texas A&M University demonstrated the injection of ions resulting from nuclear reactions into a quadrupole ion trap. Extremely high energy (20 to 60 keV) ions of unstable isotopes were collected into a quadrupole ion trap from a nuclear reactor, passing ions through a thin metal foil to slow the ions prior to injection through an endcap of a quadrupole ion trap . These ions were then laser-cooled and analyzed by laser-induced fluorescence; no buffer gas was used to damp the ion motion. They also characterized ion injection using computer simulations, and determined that the optimum conditions for ion injection and collection include small ion energies with large incidence angles. Simulations indicated that injection of ions through an endcap resulted in more efficient collection than injection through the ring electrode; injection of ions diagonally (through the gap between the ring and endcap electrodes) appeared to preclude their being trapped. Finally, they determined through simulations that axially-injected ions are only collected during a very narrow range of RF phases centered around 270° for quadrupole ion traps with RF voltage applied to the ring. It may be noted that these simulations did not address the damping of ion motion through collisions with a buffer gas.

J.E. Curtis, A. Kamar, and R.E. March of Kent University in Ontario also presented at the 1987 ASMS conference (89), the use of a quadrupole ion trap as a collision cell in a hybrid tandem mass spectrometer. In this system, "collisionally thick helium" (presumably a fairly high pressure in the millitorr range) was used as a damping and CID gas, with ions stored temporarily, prior to ejection into a quadrupole mass filter. Ions with 4 keV ion energy were injected from an AEI electrostatic analyzer diagonally into the trap through the gap between an endcap and the ring electrode. It is assumed that multiple damping collisions with the helium buffer gas resulted in trapping and some CID of the injected ions. The success of their experiments, in contrast to the predicted failure (88), can presumably be attributed to neglect of collisions with a buffer gas in the modeling performed by C.-S. O and H.A. Schuessler.

Most recently, Ray Kaiser at Purdue University demonstrated injection of ions from a thermospray ion source (39) using a line-of-sight ion injection system. Note that in this work poor mass spectral quality was attributed to the high pressures associated with the thermospray interface.

The Ideal Ion Injection System

An ideal ITMS injection system would include the pulsed and exclusive injection of positive or negative ions with no injection of electrons. When the ion pulse is gated off, neither ions (of either polarity) nor electrons should be injected. The exclusion of electrons is relatively simple from a conventional source by superposition of a magnetic field across the filament and the ionizer, collimating the electrons inside the ion source. Selective injection of only one polarity of ions poses more of a problem; with a simple Einzel lens system, during the DC pulse cycle, when negative ions are gated in, positive ions are excluded, but when negative ions are gated out, positive ions may be injected.

The detector should not be in line-of-sight with the ion source. With a high pressure source, there can be problems caused by having neutral molecules with high kinetic energies. These fast neutrals are not affected by magnetic or electric fields and could strike the dynodes or multiplier, giving rise to background noise. More recent developments in axial modulation have made it possible to reduce the kinetic energy of ions exiting the quadrupole ion trap, affording the location of the detector off-axis from the end cap (90).

The ion injection system should allow for the separation of ions from neutral gas streams, to minimize the total pressure inside the ion trap analyzer. A high pressure stream of gas directed into the ion trap analyzer could cause resolution and sensitivity problems. Helium serves especially well as a buffer gas in the ion trap because of its low mass, which allows for minimal scattering following collisions. The ITMS is much less tolerant of high pressures of heavier buffer gases. In addition, collisions of sample ions with a heavier gas between the source and trap, or inside the trap, would lead to a greater amount of collision-induced dissociation (CID) (57). The minimization of flow of neutral molecules from the ion source into the ion trap may be even more critical when the molecules are not CI reagent gases (e.g. CH_4), but rather are mobile phase molecules in LC/MS, air and water from an atmospheric sampling source, or glycerol in FAB.

The use of a non-differentially pumped vacuum system yields a simpler, smaller, and lower cost MS system. Differential pumping is commonly used in mass spectrometers which employ a high pressure ion source to keep the analyzer under adequate vacuum. Since the ITMS analyzer is much more tolerant of higher pressures than a quadrupole mass filter or a magnetic or electric sector, an off-axis ion injection system should make it unnecessary to pump differentially, especially if the ion source has a low gas conductance (small apertures).

The ion injection system should minimize the possibilities of the ions hitting any surface, as such collisions could result in neutralization or fragmentation. Just as maintaining lower pressure in the ion injection optics is important to prevent CID of the ions, this surface-induced dissociation (SID) is to be avoided if possible in the injection system. The exception to this premise is the case where one wishes to perform surface-induced dissociation as a means of reducing kinetic energy when a quadrupole ion trap is used as a secondary analyzer in a tandem instrument.

Ions should enter the ion trap analyzer with as low a kinetic energy as possible. In the absence of buffer gas, ions which are injected into an ion trap are theoretically unstorable, although they can have a finite storage time (88). As identified in Chapter 3, an ion which has enough kinetic energy to enter the trapping field has enough kinetic energy to exit that field unless its trajectory is damped by some method such as collisional cooling. The use of helium as a buffer gas reduces the kinetic energy of injected ions through collisions, and theoretically, should permit the trapping of ions. It is therefore essential that there be a buffer gas inside the ion trap analyzer to damp the motion of injected ions. Helium has also been demonstrated as a useful target gas for CID in the ITMS (8). In an MS/MS experiment, ions are selectively energized, resulting in fragmentation due to multiple collisions with helium buffer gas. The extent of CID increases with the kinetic energy of the excited ion. Ions which have been injected into the ion trap have similar kinetic energies to ions which have been excited through resonant excitation; maximum possible ion kinetic energy coincides with ion excursions which approach the dimensions of the ion trap electrodes. The kinetic energy of injected ions should be as small as possible both to increase the probability that a given ion will be captured by the RF field, and to minimize CID effects attributable to those ions which had too much energy to be captured, yet fragmented into lower energy daughter ions which were trap-able.

Injection Optics Options

The initial task of this project was the selection of ion source, ion transfer optics, and mass analyzer. Although the mass analyzer in this case is a quadrupole ion trap mass spectrometer with an electron multiplier detector, it may be noted that the source and transfer optics which were developed should work equally well with other mass analyzers such as a quadrupole mass filter.

As previously mentioned, the ionization technique was chosen to be positive and negative chemical ionization (CI). Several models of ionization sources were considered; a Finnigan model 5100 SP chemical ionization source was chosen because it was designed to be used in a non-differentially pumped quadrupole mass spectrometer system. The requirement for differentially pumping has been reduced by using a low conductance ion source which has a small ionizing volume and very small holes for the introduction of electrons and extraction of ions.

The most difficult choice was that of the transfer optics. Indeed, almost a month was spent modeling and evaluating the various options before one was chosen and optimized. As stated before, the ion transfer optics should: allow the electron multiplier to have no line-of-sight with the ion source; allow the selective and exclusive gating of positive, negative or no ions; be open to gas flow to minimize CID effects; have no surface in-line with the ion beam to minimize SID effects; and finally, allow simple and complete control of ion energy.

The transfer optics devices considered were (see Figure 5-1) (a) a Bessel box, (b) a split tubular lens, (c) a Balzers off-axis lens system, (d) a DC quadrupole deflector, (e) a tandem DC quadrupole deflector, and (f) a DC monopole deflector. Trajectories of focused ions are indicated by small arrows. Neutrals which enter along with ions travel line-of-sight, and therefore are separated from the ion beam in all designs except (b). In (b) and (c), the center electrode is split so that the potential on each side can be independently set. All of these devices are electrostatic devices, and are thus kinetic energy analyzers of one form or another. With this in mind, the ideal transport device would be one which transports ions of a range of kinetic energies, with good transmission, and minimal discrimination against initial positions and angles.

The split tubular lens (Figure 1b), and Balzers off-axis lens system (Figure 1c) were removed from consideration early on based on the expected chromatic aberrations resulting from asymmetry. In addition, the split tubular lens leaves the source in line-of-sight with the detector. The two most promising devices were simulated: the Bessel box, because it has been applied to similar problems; and the DC quadrupole deflector and

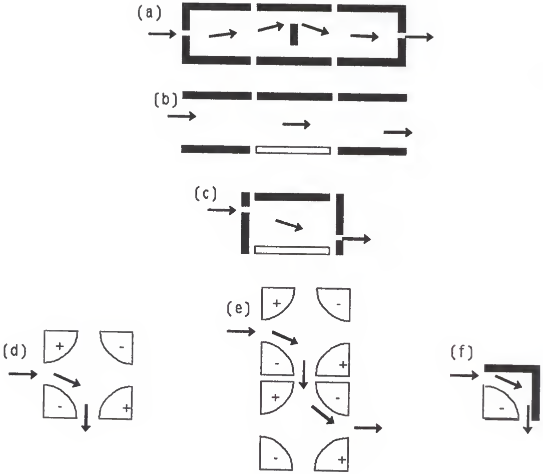

Figure 5-1: Ion optical devices considered for this system. The devices shown are: (a) Bessel box, (b) split tubular lens, (c) Balzers off-axis lens system, (d) quadrupole deflector, (e) tandem quadrupole deflector, (f) monopole deflector

its derivatives, because it is open to gas flow, and has the potential for the use with multiple sources or multiple analyzers.

Bessel Box

A Bessel box is an ion optical device which is often used to prevent line-of-sight between an ion source and detector while allowing transmission of ions. A Bessel box contains a beam stop in the line-of-sight of the incoming ion beam. A typical Bessel box (Figure 1a) consists of three successive tube lenses with identical inner diameters and similar lengths. At the entrance of the first tube lens, and at the exit of the third tube lens, are small apertures which define the line-of-sight and narrow the acceptance area of the device. Centered inside the second tube lens is a round disc (beam stop) which has an area slightly larger than that of the entrance and exit apertures. This disc is held at a potential such that ions are directed around it by the electrostatic field. Since neutrals and photons are not affected by the electrostatic field, they are not redirected and are stopped or scattered by collisions with the surface.

One potential problem with the Bessel box is that there is a chance for surface-induced dissociation (SID) since energetic ions may collide with the beam stop. There is also the potential for ionizing neutrals and sputtering ions from the surface by collisions. Another drawback is the fact that the ion transfer optics should be open to gas flow, while a Bessel box is inherently closed to gas flow.

SIMION was used to simulate a Bessel box using a design based on an experimentally optimized Bessel box provided by M. Schmidt of Finnigan MAT in Bremen, Germany. These simulations demonstrated a poor transmission of ions, with transmission severely dependent upon the entrance angle into the Bessel box. Another detracting feature discovered through simulations was that small variations in the potential applied to the center tube lens resulted in drastic change in transmission efficiency. One important impression obtained from SIMION simulations is that this device would be difficult to manually tune (that is, to experimentally determine the voltages for optimum transmission). It was ultimately decided that a Bessel box would be a usable but inappropriate solution for this application.

Different Uses of Quadrupole Fields

A quadrupole is a mechanically simple device consisting of four symmetrical hyperbolic rod electrodes which are arranged in parallel such that a two-dimensional hyperbolic field is maintained between them. Typically, opposite pairs of rods are electrically connected, and potentials (RF and/or DC) of opposite polarity are applied to these pairs. While hyperbolic quadrupoles allow for more perfect hyperbolic fields, it is common to replace the hyperbolic rods with round rods with a suitable alteration of the distance between adjacent rods to approximate a hyperbolic field. The ideal ratio of rod radius to the inscribed radius (half the distance between diagonally opposed rods) is 1.148 (91). Round rods are easier to fabricate, and offer comparable performance if ions are kept to the center of the quadrupole where the field is essentially hyperbolic. Depending upon the types of voltages applied to the quadrupole (RF and/or DC) and the orientation of the ions' path through the device, the quadrupole can provide various ion optical functions.

Quadrupole mass filter. The most celebrated use of a quadrupole is as a mass filter, which transmits ions of only a narrow mass range, typically a single mass-to-charge ratio (m/z). Ion trajectory is parallel to the axis of the rods, which have a combination of

RF and DC voltages applied to them. If only RF voltages are employed, then a wide range of m/z's are transmitted; thus, an RF-only quadrupole is often used as an ion pipe or collision cell in an MS/MS instrument.

DC quadrupole lens. One or more short sections of quadrupoles can be used as a quadrupole lens. Ion trajectory is again parallel to the axis of the rods, and DC voltages are applied to opposite pairs of rods. Used as such, a quadrupole lens serves as a beam shaper, defocusing ions in one direction by rods of one polarity, while focusing ions in the other direction by rods of the opposite polarity. Pairs of successive complementary DC quadrupole lenses are commonly used to focus (in both directions), ion beams in accelerators and sector mass spectrometers. An ion injection system utilizing three sequential quadrupole lenses to transport ions from a particle beam ion source into a quadrupole ion trap has been reported by Mark Bier of Finnigan Corporation (85).

Quadrupole deflector. The application of the quadrupole which is most important to this work is as a 90° deflector. In this case, ions enter the quadrupole perpendicular to the parallel rods (between two adjacent rods), and have trajectories which bend 90° around one of the rods. DC voltages are applied to the rods, resulting in a low resolution electrostatic energy analyzer. The DC quadrupole as a 90° deflector was characterized by H.D. Zeman of Stanford Research Institute (92). This paper reported theoretical calculations of the deflection properties of the DC quadrupole, as well as an application of this device. One notable limitation of the DC quadrupole deflector is the absence of focusing in the plane perpendicular to the quadrupole field plane. More specifically, if the plane defined by the quadrupole field (which is perpendicular to the rods) is considered the x-y plane, there is focusing only in the x- and y-directions, not in the z-direction parallel to the rods. A mass spectrometer designed at Stanford Research Institute for

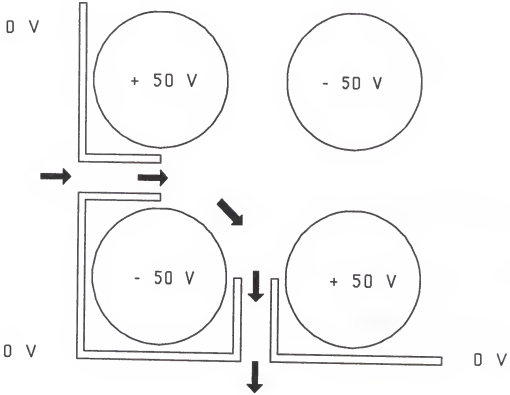

Figure 5-2: Schematic of a quadrupole deflector built from round rods. The grounded shield lenses are used to create a field free region for transmission of ions into and out of the hyperbolic field.

studies of photodissociation of ions (93) employed two DC quadrupole deflectors to make the ion and laser beam coaxial through the reaction region. A preliminary design of a time-of-flight - Fourier transform mass spectrometer (TOF-FTMS) employing a DC quadrupole deflector for beam steering was reported at the 1987 ASMS meeting by C.D. Hanson, M.E. Castro, and D.H. Russell, of Texas A&M University (94). The DC quadrupole deflector has been extensively modeled in this project as an integral part of the complete injection system, as discussed in the following section.

Simion Modeling of Quadrupole Deflector Injection System

SIMION, an ion optics modeling program (95), was used to characterize potential ion optics systems. SIMION allows the user to create a two-dimensional schematic of an ion optics device. It then calculates the electrostatic fields between ion optical elements, and the trajectory of ions through this device. The user has complete control of the design of the ion optics elements and the voltages applied, as well as the charge, mass, kinetic energy, and initial velocity vectors of ions which are modeled. This program allows the computer modeling of virtually any ion optics design, limited only by the finite resolution of the calculated field. This remarkably powerful program, which runs on IBM compatible personal computers, is distributed freely by David A. Dahl of EG&G Idaho, Idaho National Engineering Lab. It has its origins at LaTrobe University in Melbourne Australia, at the hands of Jim Morrison and Don McGilvery.

SIMION modeling was used to numerically calculate the fields inside the DC quadrupole deflector, to study its function and, ultimately, to aid in the design of an optimized quadrupole deflection system. Initial simulations of the DC quadrupole deflector with round rods demonstrated that some shielding was necessary to minimize the effects of fringing fields present in the gap between adjacent rods. Round rods can be used to approximate a hyperbolic field; however, this approximation is ideal only near the center of the field created by four rods. This field is less ideal very near the rods themselves. The field is defocusing outside of the quadrupole deflector. For this reason, it was necessary to have rather deep parallel plates prior to the DC quadrupole deflector to create a field free region, allowing the ions to be injected into the center of the gap between two adjacent rods (see Figure 5-2). Such an arrangement could help to minimize the effects of fringing fields, but the device would be difficult to machine and assemble.

The use of quarter round rods was observed by simulation to eliminate the need for these complicated electrodes if the ion beam was well collimated before transmission into the quadrupole field. Fringing field problems were minimized by proper selection of potentials on the entrance and exit lenses to the DC quad. A system using quarter round rods was studied and ultimately integrated into the final ion injection transfer optics system.

Simulations were made of DC quadrupole deflectors made from round (or quarter round) rods which, due to the non-ideal spacing between opposite rods, produced non-hyperbolic fields. From these simulations, it was evident that DC quadrupole deflectors with wider than ideal distances between diagonally opposed rods have lower energy resolution (and thus less energy discrimination) than those with ideal inscribed radii, but require much larger voltages for operation. Such devices may be useful in applications requiring less discrimination of ion energies, for example, the transfer of ions from a non-mono-energetic ion source. Since this project uses a nearly mono-energetic source, the ideal ratio of rod radius to inscribed radius was used.

Because there is no focusing of the ion beam in the plane parallel to the rods ('z' direction), the quadrupole deflector requires a well collimated entrance beam, both to minimize divergence in the 'z' direction, and to keep the ion beam near the center of the device, where the field is most nearly hyperbolic. This is best accomplished by maintaining long focal lengths in the entrance and exit ion optics. These long focal lengths have an added benefit of separating the ionizer and analyzer in space, a requirement in this system driven by the desire to have minimum changes in the analyzer design from a standard system. Tube lenses are used to allow for long focal lengths both upon entrance to, and exit from, the DC quadrupole deflector. In order to obtain long focal lengths during extraction from the source, an extraction lens is placed a distance from the source. In this way, thermal (low energy) ions are pulled from the exit aperture of the ion source and are gently collimated and transported through the tube lens to the DC quadrupole deflector. Fairly high lens voltages and hence high ion energies (50 to 100 eV) were modeled based on the supposition that large energies would have minimal problems due to charging of insulators. No mass discrimination of the injection system was predicted based on SIMION results, nor was mass discrimination observed experimentally.

Energy Dependence of Quadrupole Deflector

The energy-dependence of ion trajectories through the DC quadrupole deflector is shown in Figure 5-3. Trajectories are shown for positive ions which are started at the exit aperture of the source with a variety of initial energies (15 to 65 eV with an interval of 10 eV). Low energy ions are drawn closer to the negatively biased bottom left rod; higher energy ions are able to overcome the attractive field of this rod and are shown

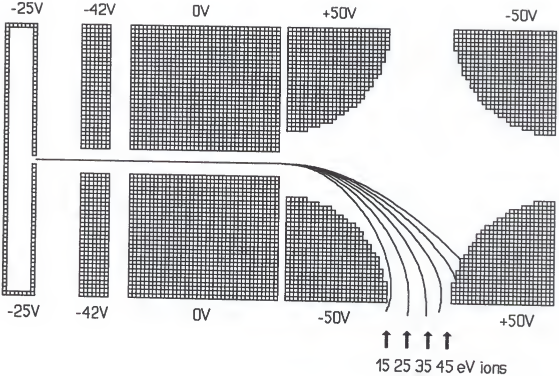

Figure 5-3: SIMION simulation showing the energy dependance of ion transmission through the quadrupole deflector. The trajectories correspond to initial ion energies of 15, 25, 35, 45, 55, and 65 eV from left to right.

hitting the positively biased bottom right rod. The optimum ion energy would be that which allows the ion to exit the DC quadrupole deflector midway between the bottom two rods, in this case 30 to 35 eV. The DC quadrupole deflector is capable of transmitting ions of virtually any energy by proper selection of the rod voltages. This property is especially important for relatively simple control of the energy at which ions are transmitted from an ion source through the DC quadrupole deflector and into the ion trap analyzer. In, addition, with energy discrimination of the DC quadrupole deflector, the probability is reduced that CID product ions (which may be formed between the source and the deflector) would be transmitted, as these product ions would have only a fraction of the kinetic energy of their parent ion, and may be filtered out by the quadrupole deflector.

Angular Acceptance of Quadrupole Deflector Design

Figure 5-4 illustrates the ability of the optics system to collimate ions with the same initial energy (0.25 eV), exiting from the center of the ion source exit aperture with various initial angles (-50° to +50°). In this example there are three focal points, one inside each tube lens, and one at the entrance to the ion trap. Note that in this simulation, the ionizer was maintained at +5 volts, with the potentials applied to pairs of rods in the quadrupole deflector maintained at 0 and -100 volts, yielding an effective ion energy of -55 volts for ions transferring through the quadrupole deflector.

Positional Acceptance of Quadrupole Deflector Design

Figure 5-5 illustrates the ability of the optics system to collimate ions exiting from the ion source with the same initial energy and angle (0.25 eV at 0°) but various initial positions. In this case, the focal points are seen before the entrance to each of the tube

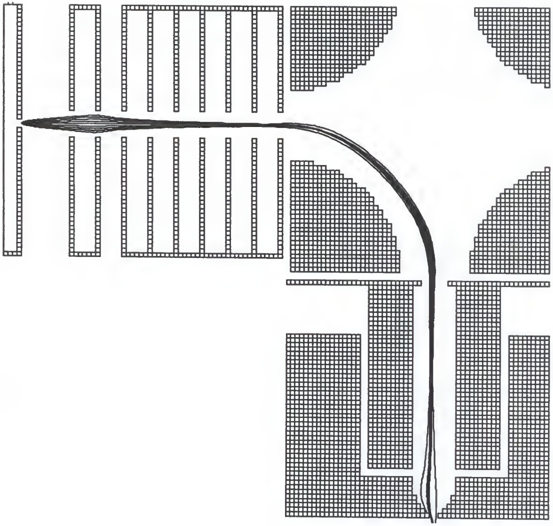

Figure 5-4: Angular acceptance of ion injection optics. Initial angles ranged from -50° to +50°.

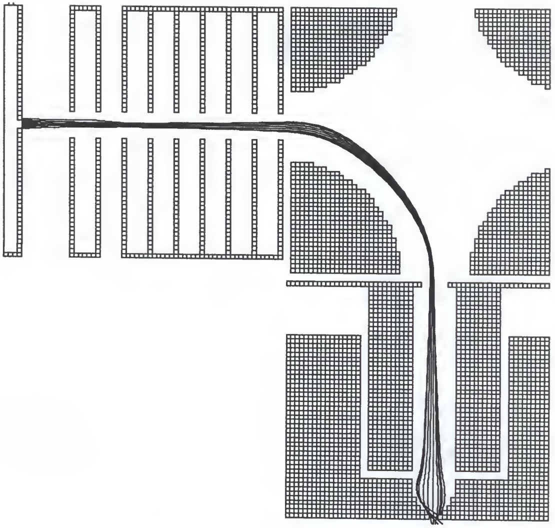

Figure 5-5: Positional acceptance of ion injection optics. The trajectories are shown starting at various initial positions at the exit aperture of the ion source.

lenses and the ion trap endcap. The actual ion beam will have a range of initial ion positions, energies, and directions, and thus more complicated trajectories than these simple examples, but the principle that a collimated beam travels through the DC quadrupole deflector with minimal loss is demonstrated. Figure 5-6 is an enlarged portion of Figure 5-5 showing the defocusing of ions at the entrance to the ion trap analyzer. This effect is beneficial since it allows for large initial angles during ion injection into the ion trap which theoretically increases the probability for collection (88).

Variations of the Quadrupole Deflector

Other derivatives of the DC quadrupole deflector are the monopole deflector and a tandem DC quadrupole deflector (Figures 5-1f and 5-1e). A monopole can be constructed from a hyperbolic (or round) rod and a plate which has been bent at a 90° angle. The angled plate is placed such that a hyperbolic field is created between the rod and the plate. This field corresponds to that of one quadrant of a DC quadrupole deflector, and could be used as a simple 90° deflector, but would have problems due to asymmetry; the trajectory of ions traversing the hyperbolic field may travel through more than one quadrant, and would be lost. There is also the possibility for collisions with the plate electrode surface leading to undesirable surface-induced dissociation. The trajectory of an ion through a single quadrupole deflector is slightly asymmetric, and thus a single DC quadrupole deflector has some slight chromatic aberrations, which might be eliminated by using two DC quadrupole deflectors in tandem (93). In addition, a tandem DC quadrupole deflector would allow the ion source to be parallel with the analyzer without line-of-sight between source and detector. Figure 5-7 illustrates the trajectories of ions traversing through a tandem DC quadrupole deflector. Note that in this simulation the

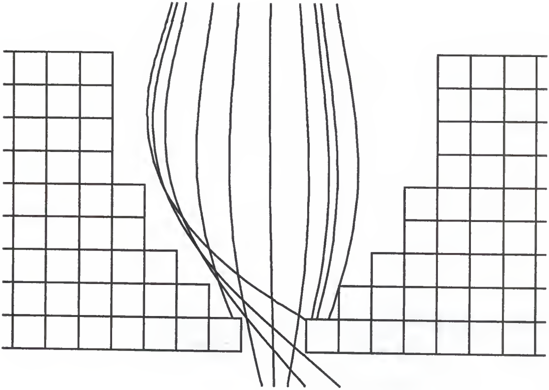

Figure 5-6: Enlarged view of trajectory shown in Figure 5-5 which shows the defocusing effect of the entrance endcap of the ion trap analyzer.

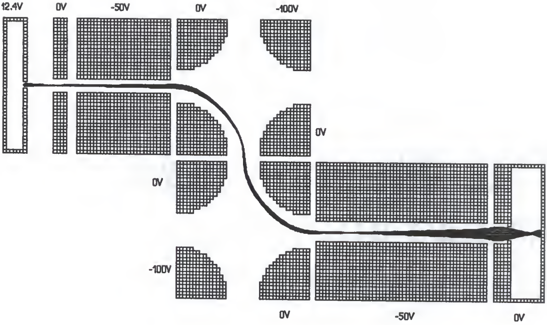

Figure 5-7: SIMION simulation of tandem quadrupole deflectors. Initial conditions were 0.25 eV initial energy with various initial angles.

initial kinetic energy is slightly larger than that in the single deflector simulations. This figure demonstrates an alternative to a 90° DC quadrupole deflector with similarly excellent transmission.

Experimental Design

After final modeling with SIMION was completed, a single design was chosen. A schematic of this design with typical operating voltages is shown in Figure 5-8. Four quarter round rods with radius 0.5 inches and length 3.25 inches were machined out of stainless steel. These rods were bolted to two anodized aluminum (non-conducting) mounting blocks. A magnet yoke was fashioned from cold rolled steel, fitted with two permanent magnets, and mounted with electrical isolation to one of the faces of the anodized aluminum blocks such that a magnetic field enveloped the ion source. A single long tube lens was machined out of stainless steel and was mounted to two of the quarter-round rods. This lens serves as the exit lens of the DC quadrupole deflector, and the transport lens into the filament endcap of the quadrupole ion trap.

Lenses. In order to provide for open gas flow out of the ion source, multiple thin lenses were electrically connected to create fields equivalent to those provided by a "thick" or tube lens. Finnigan Incos 50 lenses and one tenth inch ceramic spacers were used to create a "thick" extraction lens from two electrically connected thin lenses. Similarly, seven thin lenses were connected electrically to make one "tube lens". The lenses and source block were stacked and mounted using four 0-80 threaded studs projecting from two of the quadrupole rods. This whole assembly was bolted to a standard Finnigan ITMS ion trap using a modified mounting flange bolted to the anodized aluminum mounting

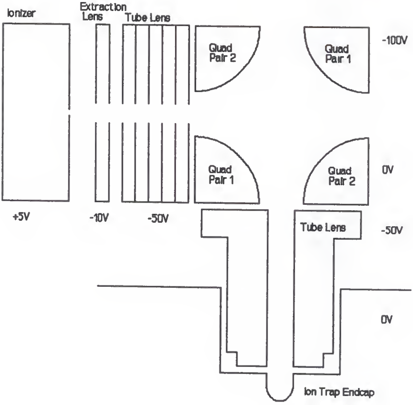

Figure 5-8: Final design of quadrupole deflector ion injection system.

blocks of the DC quadrupole deflector. A Finnigan 3200 EI ion source and a Finnigan 5100 SP CI ion source were used as ion sources in these experiments.

Electronics. The quadrupole ion trap analyzer was operated using standard Finnigan MAT ITMS electronics, including a Selective Mass Storage DC power supply which allowed the application of DC voltages in addition to the RF voltages applied to the ring electrode of the quadrupole ion trap. The only modification to this system was the attachment of an electrical lead to the TTL electron gun gate pulse.

A Finnigan 4000 series ion source controller was used to provide the filament control circuit. A Finnigan 4500 PPINICI lens controller box was modified to provide the ion source and lens voltages. The key modification to the electronics was the optimization of one of the switching lens power supplies to reduce the rise time of the lens driver circuit to 20 μs. These modifications were prescribed by Bill Fies of Finnigan Corporation. Ion gating was effected by applying the TTL gate signal from the ITMS electronics to the input of the modified PPINICI lens controller. The PPINICI lens controller contains a TTL driven electronic switch which alternates the input of two separate drive voltages, allowing the high-speed switching between two voltage levels.

Software. All mass spectra were acquired using ITMS Revision B software with the ITMS Scan Editor, and the FORTH programming option. All data were obtained using the Axial Modulation technique developed by Michael Weber-Grabau and David Tucker of Finnigan Corporation (26), which provides for optimum sensitivity and resolution. A number of FORTH user programs were written for automated data acquisition, including experiments involving the ramping of RF voltage during ion injection, and the multiplier gain calculation. Automated data reduction was performed using programs written in

Turbo BASIC which were customized for each set of data. A modified version of this software is available from the Yost group by written request.

Vacuum hardware. The injection system was contained in a glass-topped vacuum cradle equipped with eight ISO-K flanges. Quartz heaters powered by a Variac were used to maintain a chamber temperature at approximately 100°C. The ion source and ion trap analyzer were not heated except by radiation from the quartz heater. A 330 Liter per second turbomolecular vacuum pump was used to maintain a base pressure of roughly 2×10^{-7} torr. Chamber pressure measurements were made using a Bayard-Alpert type ionization gauge and are reported uncorrected unless otherwise noted.

Gases and reagents. Ultra high purity (UHP) helium was plumbed directly to the ion trap analyzer maintaining a helium pressure inside the analyzer of approximately one millitorr, and a vacuum chamber of 10^{-5} torr. CI reagent gases (helium, methane, and argon, UHP grade) and sample vapor were plumbed directly into the CI ion source through a combination of quarter inch diameter stainless steel tubing and quarter inch diameter teflon sleeves. Source pressure measurements were made using a thermocouple gauge in the CI gas stream external to the vacuum chamber. Source pressures were typically 0.2 to 1 torr during chemical ionization experiments, yielding a vacuum chamber pressure of 2×10^{-4} torr. Analyte compounds were bromobenzene (Aldrich Chemical) and perfluorotributylamine (PCR Chemicals, Gainesville, FL).

Typical operating voltages. Typical voltages applied to the lenses were similar to those modeled using SIMION (see Figure 5-7). For positive ions, the ion source (the potential of which determines the kinetic energy of the injected ions) was maintained at +5 to +10 volts. The extraction lens was typically maintained at -10 volts; however, extraction voltages as large as -314 volts were used to obtain high sensitivity for low pressure operation of the ion source. The tube lenses were maintained at a potential midway between the potentials applied to the quadrupole rod pairs (typically -50 to -75 volts). Rod pair 1 was used as the gate pair, and had a potential -100 to -150 when ions were gated into the ion trap analyzer, and +100 to +150 when ions were deflected away from the ion trap analyzer. Rod pair 2 was typically connected to earth ground, although voltages were applied to this pair when high energy ions (20 to 80 eV) were transmitted into the ion trap analyzer. Tuning was a relatively simple process because wide ranges of applied voltages resulted in minimal changes in sensitivity. The most critical voltages were those applied to the DC quadrupole deflector rods; even variations of 10 volts caused minimal changes in signal intensity.

Experimental Results and Discussion

Initial Attempts to Obtain Spectra

Initial attempts to inject ions into the ion trap analyzer using the CI ion source without CI reagent gas, (essentially, using the CI ion source as an EI ion source with a smaller than usual exit aperture), met with no success; the filament burned out after only two hours of operation (due to an inappropriate emission current setting). It was decided to reassemble the injection optics system with an EI source replacing the CI source, since CI ion sources are functional, but not terribly sensitive, when used in EI mode. In addition, the magnetic field provided by the two permanent magnets mounted in the magnet yoke was increased by a factor of 7 by moving the magnets closer together, with their positions held by set screws.

EI mass spectra. Once the EI ion source was installed and tuned to nominal voltages from SIMION simulations, a mass spectrum of argon with the air and water background of the vacuum chamber was obtained. An early EI mass spectra of perfluorotributylamine (PFTBA or FC-43, a common calibration compound for mass spectrometers) with a nominal ion injection energy of 6 eV is shown in Figure 5-9. This spectrum includes the typical positive ion mass peaks of m/z 69, 100, 131, 219, 264, 414, 464, 502, 614, as well as the common ion trap FC-43 peak at m/z 197 which is a product of an ion/molecule reaction of m/z 219 with water: ($C_4F_9^+ + H_2O \rightarrow C_4F_7O^+ + 2HF$). There are also some contaminant peaks in the spectrum, notably the peak at m/z 149 which is indicative of a phthalate impurity (presumably from handling the injection system with rubber gloves). The most notable feature of this spectrum is the presence of m/z 219 and its associated ion/molecule reaction product at m/z 197. Their presence in the spectrum suggests that minimal CID fragmentation is occurring during the transmission of ions from the ion source, through the DC quadrupole deflector, and into the ion trap analyzer. The ion at m/z 219 is known to be easily fragmented through low energy collisions; indeed, in previous work in ion injection from an EI source (35), the absence of this peak was used as evidence for the occurrence of CID in the ion injection process. With the high pressure of helium buffer gas inside the ion trap analyzer, injection of ions into the ion trap with any energy larger than thermal energy may result in some CID. By minimizing ion energy, these CID effects can be minimized.

CI mass spectra. The CI ion source was fitted with two pieces of quarter inch diameter stainless steel tubing (for the plumbing of CI gas), and the ion injection optics system was reassembled with the CI ion source replacing the EI ion source. Initially, helium was used to thermalize electrons for ECNCI; in later experiments, methane was used for positive and negative CI. At source pressures which provide for optimum chemical ionization sensitivity (0.2 to 1 torr), no degradation in the quality of ion trap

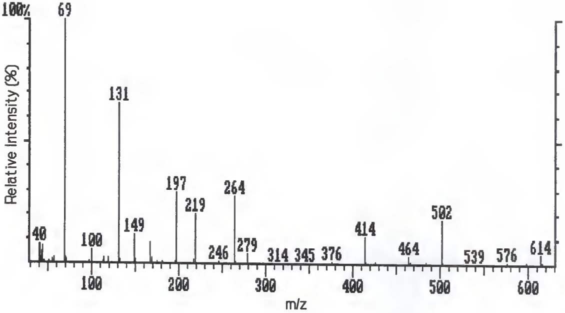

Figure 5-9: Early mass spectrum of perfluorotributylamine ions injected from an EI source. Ion energy is nominally 6 eV.

spectra was seen due to the large resultant pressure of the CI reagent gas in the vacuum chamber. Figure 5-10 is a methane ECNCI mass spectrum of FC-43. The relative abundances of the ion peaks in an ECNCI spectrum of FC-43 are observed to be strongly dependent upon the ion source temperature in conventional mass spectrometers. The relative abundances of negative ions m/z 414, 452, 557, 595, and 633 in this spectrum are indicative of the low ion source temperature during ionization. The chamber was not heated during this experiment, and therefore, the only heat applied to the ion source was the heat from the filament. Note the lack of intense low mass ions; this supports the belief that there are no CID-related fragment ions appearing in ion injection mass spectra. Due to incorrect mass assignment by the data system, the intensity of m/z 595 and 557 are attributed to m/z 596 and 558 respectively.

Mass resolution of injected ions. Figure 5-11 shows a profile spectrum of the base peak in Figure 5-10, illustrating the typical mass resolution obtained for the high mass negative ion (m/z 633) and its $^{13}C_1$ isotope peak (m/z 634) produced by methane ECNCI of FC-43.

Multiplier Noise

Since previous work (35) had noted the problem of baseline lift-off of the detector signal due to stray ions, the baseline signal level was measured with the filament off (Figure 5-12a), and with the filament on and ions deflected 180° from the ion trap (Figure 5-12b). These figures show minimal RF noise (slight rise in the baseline towards higher masses), and very few background ion events (random events in Figure 5-12b). This is proof that the magnetic field is adequate to prevent electrons from straying outside the ion

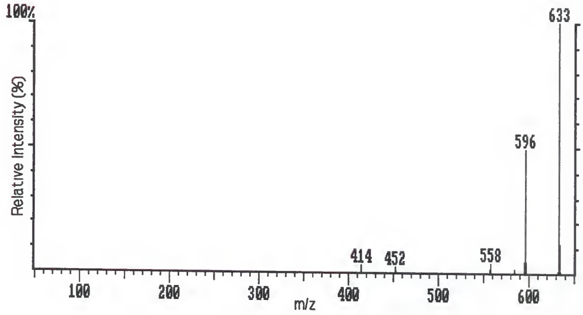

Figure 5-10: Methane ECNCI mass spectrum of injected perfluorotributylamine ions. Ion source pressure was 200 millitorr methane. Note the improper mass assignment of m/z's 557 and 595.

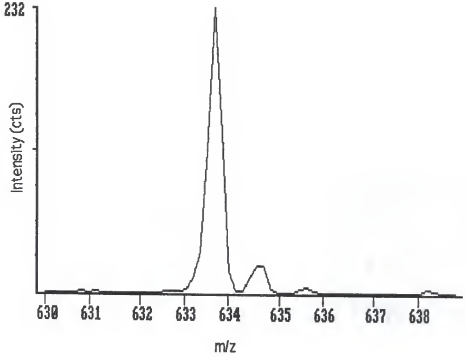

Figure 5-11: Profile mass spectrum of injected perfluorotributylamine negative ion m/z 633.

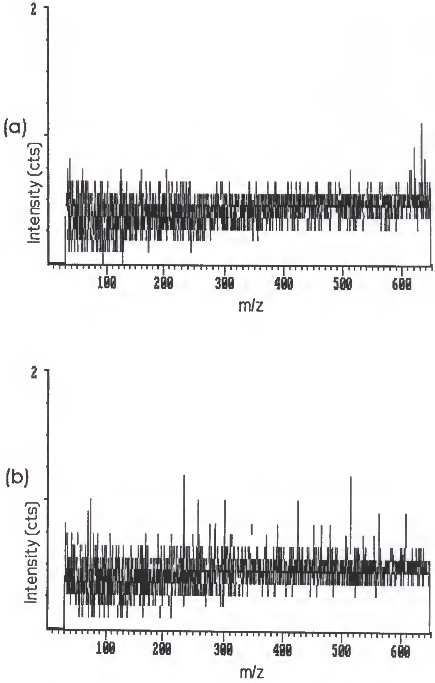

Figure 5-12: Multiplier background noise: (a) Filament off; (b) Filament on, with ions deflected 180° from ion trap analyzer.

source to create ions in the vacuum chamber which can travel around the ion trap to the multiplier and be detected.

Ion Injection Time

Inherent to the trapped ion operation is the necessity for pulsed ionization. For internal ionization of ions in a quadrupole ion trap, electrons are gated into the analyzer during an "ionization time". Similarly, ions are gated from the ion source into the ion trap by means of voltage pulses. Initially, the voltage pulse for the gating of ions into the ion trap during the "ionization time" was applied to the seven-element tube lens between the ion source and the quadrupole deflector. However, when ionization time was varied, only slight variations in the injected ion intensity were observed. This effect was attributed to the integration of ion signal by temporarily storing the ions in the region between the source and tube lens. When the gate pulse is applied to quadrupole rod pair 1 (the lower left and upper right rods in Figure 3), ions are directed into the ion trap, or 180° from the ion trap, depending on whether the gate is "on" or "off". Gating these lenses, a linear relationship between ionization time and collected ion intensity was seen. This relationship is the basis for the technique of automatic gain control which was developed at Finnigan for the electron injection mode of the ion trap.

Collection Efficiency Measurements

Collection efficiency as a function of RF voltage. An interesting phenomenon is apparent when the collection efficiency of ion injection is observed as the RF trapping voltage applied to the ring electrode of the ion trap analyzer during ionization is varied. Figure 5-13 shows the ion intensities for the Br^- isotopes of m/z 79 and 81 produced by

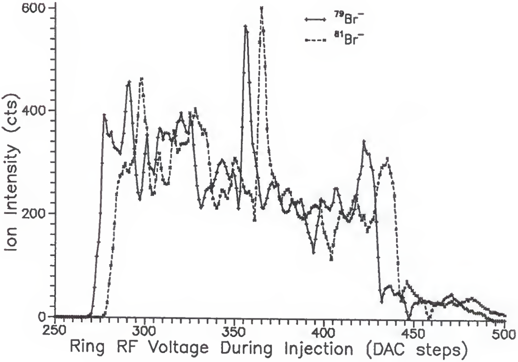

Figure 5-13: Intensities of bromine negative ions m/z 79 and 81 from chemical ionization of bromobenzene plotted as a function of trapping RF voltage during ion injection.

chemical ionization of bromobenzene. The fine structure in these plots is attributed to nonlinear resonances from fourth- and sixth-order distortions of the hyperbolic field inside the ion trap analyzer (32). The relative minima reflect decreased trapping efficiency when the ion is in resonance. Such fine structure is especially problematic when one considers the effect of these nonlinear resonances upon the isotope ratios of collected ions.

When the isotope ratio of the collected ions m/z 79 and 81 in Figure 5-13 is plotted, (Figure 5-14) it is apparent that this ratio varies with ring RF voltage during ion injection, from the theoretical bromine isotopic ratio of 1.03:1. Figure 5-15 shows the same data as in Figure 5-13 plotted with the x axis as the Mathieu parameter q (essentially normalizing RF voltage to the mass of the ion). In this figure, it is apparent that the fine structure is indeed related to the physics of the ion trap, rather than some experimental variation of pressure or voltages. This fine structure is smooth-able by ramping the RF voltage during ion injection, essentially averaging the effects of nonlinear resonances. Data have also been taken at various combinations of RF and DC voltages (essentially mapping the Mathieu stability diagram) for comparison with results discussed by Peter Dawson in reference 91.

Collection efficiency as a function of mass. While no rigorous studies have been made with this system for the collection efficiency of injected ions as a function of mass, mass spectra obtained show ion intensity ratios which are comparable to those obtained through internal ionization. Some data have been obtained relating to the collection efficiency of injected low energy (0 to 10 eV) ions as a function of RF voltage during injection, using a range of masses; however, more work is needed to completely characterize this relationship. One trend observed was that there was a definite variation in the collection efficiency of low mass (m/z < 100 to 150) injected ions as various RF

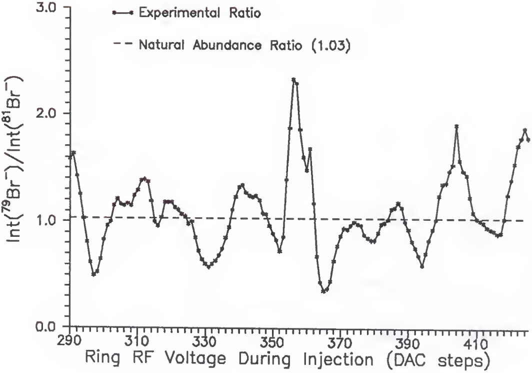

Figure 5-14: Intensity ratio of bromine negative ions m/z 79 over m/z 81, plotted as a function of trapping RF voltage during ion injection.

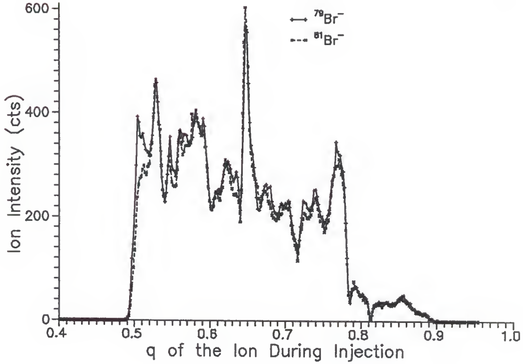

Figure 5-15: The intensities for the two bromine isotopes shown in Figure 5-13, plotted as a function of the Mathieu parameter q.

trapping voltages were used (Figure 13), but the injection of high mass ions resulted in much less variation of ion intensity with RF voltage. This effect is presumably due to the lower velocity and lower resonant frequency of high mass ions inside the hyperbolic field. Another trend observed was that the optimum RF voltage for collection of high mass ions (m/z > 400) was approximately the same as for sensitive collection of lower mass ions (120 to 250 RF dac steps, corresponding to low mass cut-offs of approximately 20 to 40 amu). Ion injection with the trapping RF voltage ramped over a narrow range of voltages should result in good collection efficiency of both light and heavy ions.

Ion collection efficiency as a function of injected ion energy. The collection efficiency of injected ions was measured as a function of injected ion kinetic energy in two separate sets of experiments. In the first set of experiments, the collection efficiency of argon 40^+ ions was measured as a function of ionization RF voltage (parameterized as the Mathieu parameter q) at various injection energies, using the ITMS data system to measure ion intensities. In the second set of experiments, argon 40^+ ion transmission was measured at various ion injection energies at three locations in the injection system: the entrance endcap of the ion trap, the exit endcap of the ion trap, and, after collection and storage, the electron multiplier. In this second set of experiments, the currents at the endcaps were measured using a biased electrometer, and the ion current detected at the multiplier was calculated using results obtained from the ITMS data system. Both sets of experiments indicate that the best collection efficiency occurs for ions with as small an energy during injection as possible.

Ion collection efficiency as a function of ion energy and ionization RF voltage. The potential difference between the ion source and the entrance endcap of the ion trap determines the kinetic energy of injected ions. The DC quadrupole deflector ion injection system is tunable to allow transmission of ions with energies as high as 80 eV.

The effect of the RF voltage level applied to the ring electrode during ionization was measured in ten separate experiments with injection energies ranging from a 3 eV to 70 eV. Argon 40^+ ions were created in the CI ion source under low pressure conditions (low millitorr source pressure), and were injected into the ion trap analyzer using the DC quadrupole deflector injection system. Ion injection time for these experiments was 50 ms. This fairly long injection time was used to allow for maximum ion current using minimal argon sample pressure, minimizing effects of charge exchange of argon ions with argon neutrals within the ion trap. Each data point corresponds to an average of five mass spectra which were acquired sequentially.

The partial pressure of argon introduced into the vacuum chamber was approximately 10^{-5} torr as measured using a Bayard-Alpert type ion gauge. Helium buffer gas pressure in the vacuum chamber was measured to be 2×10^{-5} torr, corresponding to a pressure inside the analyzer of approximately 1.4 millitorr. All experiments were performed under the same general pressure conditions, but minor pressure fluctuations were seen during these long experiments (20 minutes of acquired data per plot).

Figures 5-16 through 5-18 show the intensity of collected argon ions plotted as a function of the Mathieu parameter q (RF voltage divided by mass, multiplied by some instrument constants) from three of these ten experiments. Figure 5-16 shows the collection efficiency of argon 40^+ ions as a function of q with a source voltage of +5 volts relative to ground; this voltage was within a few volts of the optimum voltage for collection efficiency for this ion injection system. The cause for the fine structure in this plot is discussed in an earlier section of this chapter.

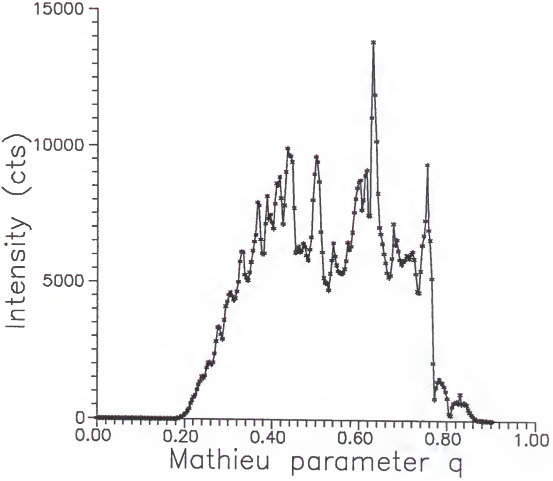

Figure 5-16: Intensity of the argon positive ion m/z 40 plotted as a function of the Mathieu parameter q. Nominal injected ion energy is 5 eV.

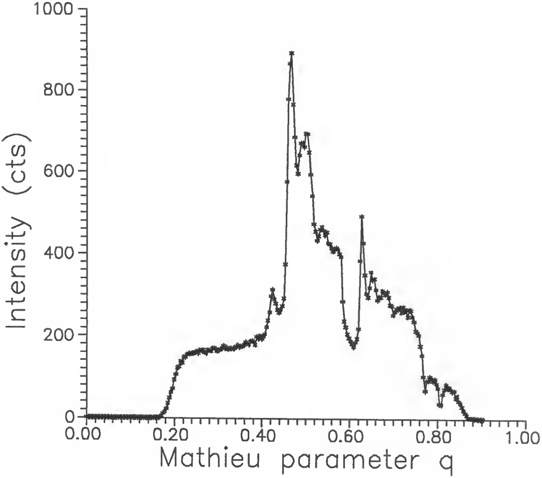

Figure 5-17: Intensity of the argon positive ion m/z 40 plotted as a function of the Mathieu parameter q. Nominal injected ion energy is 40 eV.

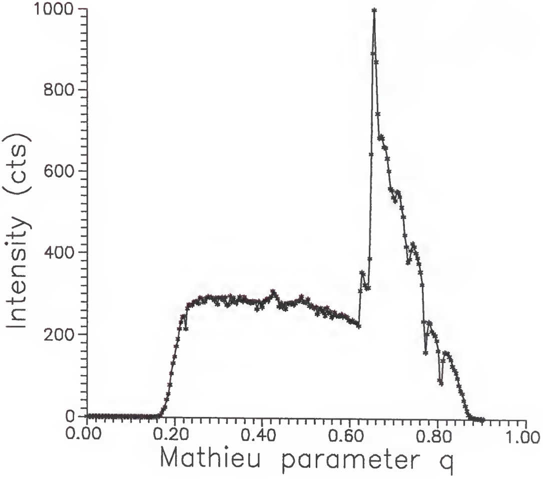

Figure 5-18: Intensity of the argon positive ion m/z 40 plotted as a function of the Mathieu parameter q. Nominal injected ion energy is 70 eV.

Figures 5-17 and 5-18 show the collection efficiency of argon 40^+ ions as a function of q for source voltages of +40 and +70 volts relative to ground. All of these experiments were performed under approximately the same experimental conditions, with the exception of source and lens voltages. The most notable difference between these figures, and Figure 5-16 is the much lower intensity of collected ions. Indeed, from these ten experiments (not all data shown), it can be inferred that, for optimum collection and detection of ions using this ion injection system, injected ion energy should be between five and ten eV. At lower ion energies, it is hypothesized that ions don't have enough energy to pass through the grounded entrance endcap; at higher ion energies, ions aren't efficiently trapped.

Analysis of the plots of higher injection energy (Figures 5-17 and 5-18) suggests that there are two phenomena occurring: collection of the high-energy injected argon ions, and charge exchange of injected argon ions with argon neutrals inside the ion trap analyzer, with the collection of the resulting low-energy ions. The relatively flat smooth baseline seen for low q values in Figure 3 is attributed to charge exchange product ions which are created inside the trap with low kinetic energies; this baseline is observed to span a range of q=0.2 to q=0.8 for argon 40^+ ions. The collection efficiency of product ions formed by charge exchange inside the trap as a function of ring RF voltage is expected to be similar to the collection efficiency of ions created by electron injection (internal ionization), that is, without fine structure. The fine structure seen at higher q values (RF voltages) is attributed to high-energy ions which are caught by the trapping RF field. At low RF voltages and high injection energies, the injected ions have too high an energy to be caught in the potential energy well created by the weak trapping RF field, even with kinetic energy losses due to collisions with buffer gas. The only ions detected are those created through charge exchange collisions inside the trap. Evidence to support this hypothesis includes the fact that in Figure 5-17, the fine structure starts lifting from the charge exchange baseline at lower q values (RF voltage) than in Figure 5-18, indicating that lower injection energies permit trapping with a shallower potential well (lower RF voltages). When higher pressures of argon were introduced into the vacuum chamber, the smooth charge exchange baseline spanning from q=0.2 to q=0.8 was observed to increase in intensity relative to the fine structure of collected high-energy ions.

Energy Acceptance of Quadrupole Deflector Ion Injection System

Characterization of energy spread of ions extracted from the ion source. The ion kinetic energy of ions extracted from the CI ion source into the quadrupole ion trap is determined from the potential difference between the ion source and the grounded entrance endcap of the ion trap analyzer. In most experiments, the source potential was maintained at +5 to +10 volts resulting in a nominal ion energy of 5 to 10 eV. However, due to field penetration of the extraction lens potential into the source, this nominal ion energy can be assumed to correspond to the maximum of a range of ion energies. The actual range of energies was determined experimentally by monitoring the ion current which reached a biased stopping plate. The bias voltage of the stopping plate was varied, and the ion current was measured at each stopping voltage, resulting in a stopping potential curve. The bias voltage at which half of the ions from the ion source are deflected and so hit the plate is the average energy of the ion beam. The first derivative of the stopping potential curve shows the distribution of ion energies in the ion beam.

A crude stopping potential experiment was set up by blocking the ion beam transmitted from the CI ion source into the "seven-lens tube lens" with a piece of steel foil

(Figure 5-19). The final three thin lenses of the seven-lens tube lens set were isolated from the other four, and a folded piece of steel foil was placed across the center lens. A biased electrometer was attached to this simple beam stop to allow measurement of ion current which was stopped by this crude collector. The first four thin lenses of the tube lens set were maintained at -75 volts, a typical voltage for operation of the tube lens in ion injection experiments. The source voltage was maintained at +10 volts for both stopping potential experiments. In the first stopping potential experiment, the extraction lens was held at -10 volts. In the second experiment -314 volts was applied to the extraction lens. Argon at 240 millitorr was used to provide the position ion beam from the ion source.

Figure 5-20 shows the argon ion currents (primarily 40^+) measured at the stopping plate with a source voltage of +10.6 volts, and an extraction voltage of -10 volts. The smooth curve represents the measured ion currents; half of the ion current is stopped by a +9 volt stopping potential, signifying an average ion energy of 9 eV. The maximum ion energy is 10.6 eV. Note that the energy stopping curve is not a symmetrical sigmoid curve as one might expect for a symmetrical distribution of ion energies. Instead, there is a sharp maximum in the first derivative at the nominal ion energy of 10.6 eV , with no ions of higher energy, but a low energy tail of ions with energies less than the nominal value. This behavior is easily understood by examining the equipotential contours shown in Figure 5-21. An extreme extraction voltage is used to emphasize the presence of the extraction potential inside the ion source. For the case presented in Figure 5-20, ions formed within the ion source by electron ionization will originate at potentials ranging from +10.6 V to 0 volts relative to ground, depending upon the ion initial position. Argon ions can also be produced by charge exchange in the region between the ion source and the extraction lens (and even beyond). There ions will have lower kinetic energies (than the

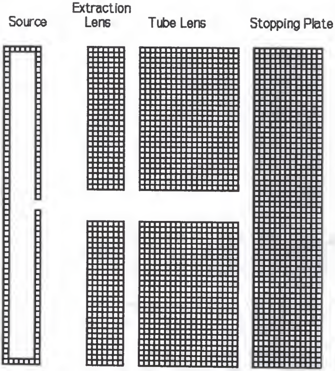

Figure 5-19: A schematic representation of the stopping potential experiment. The source voltage, extraction voltage, and tube lens voltage were kept constant while the stopping voltage was varied.

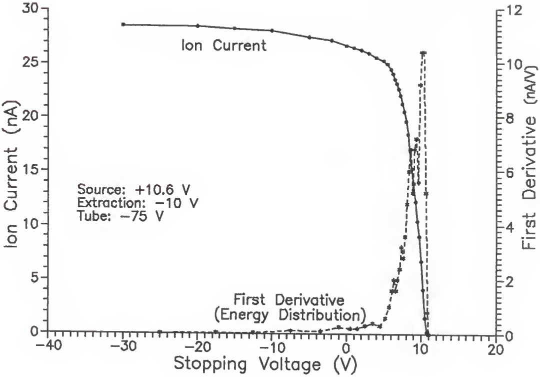

Figure 5-20: Results from the stopping potential experiment with a -10 volt extraction voltage. Measured ion current is plotted as a function of stopping plate voltage. The first derivative of this trace represents a histogram of energy distributions.

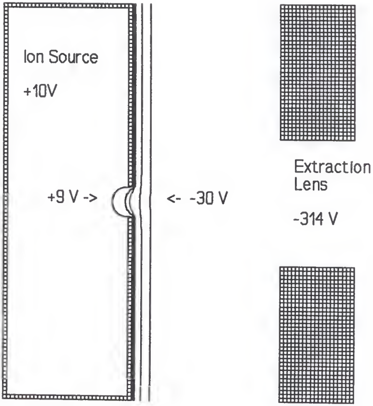

Figure 5-21: SIMION plot showing the field penetration of the extraction voltage into the ion source. Equipotential contours correspond to +9, +6, +3, -10, and -30 volts (from left to right).

nominal +10.6 eV) corresponding to the equipotential contour at which they are formed. This is the origin of the low energy tail observed in Figure 5-20. Also plotted in Figure 5-20 is the calculated first derivative of the stopping potential curve, which demonstrates a fairly narrow distribution of ion energies, 6 eV wide at 10% of full height. Note that this energy distribution is not a symmetrical (Gaussian) curve, due to the asymmetrical nature of the energy distribution of the ions produced within and outside of the source. In this case the average energy of the ion beam is within a few volts of the source voltage. These results show that almost all ions extracted from the ion source would have enough energy to be injected through the grounded endcap of a quadrupole ion trap analyzer (i.e., inspection of Figure 5-20 shows that > 95% of the ions are not stopped by the stopping plate at ground potential).

Figure 5-22 shows the argon ion currents measured at the stopping plate with a source voltage of +10.0 volts, and a much more negative extraction voltage of -314 volts. In this case, the average energy is about 0.5 eV. Approximately half of the ions which are extracted from the ion source would therefore not have enough energy to pass through the entrance aperture of a grounded endcap. The first derivative plot shows a much broader range of kinetic energies, with an energy range an estimated 20 eV wide at 10% of full height. The difference in widths of the energy distributions is due to greater field penetration of the large extraction lens voltage into the ion source aperture (Figure 5-21). With such large field penetration, ions are created with a wide range of different potentials; the first derivative of the stopping potential curve represents the distribution of initial energies, combined with the sampling efficiency of the extraction lens.

Characterization of energy acceptance of the DC quadrupole deflector. The energy acceptance of the DC quadrupole deflector was characterized through some

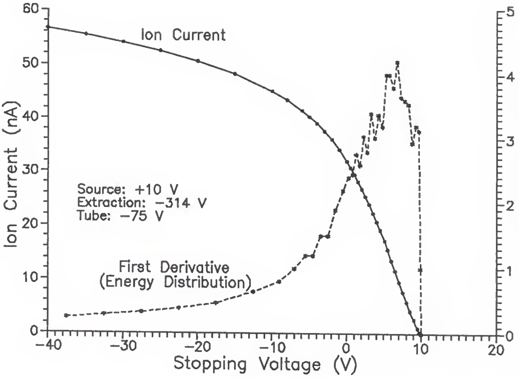

Figure 5-22: Results from the stopping potential experiment with a -314 volt extraction voltage. Measured ion current is plotted as a function of stopping plate voltage. The first derivative of this trace represents a histogram of energy distributions.

simple experiments in which the potential applied to the ion source was varied (while a constant potential difference of 70 volts was maintained between the ionizing filament and source) , and the transmitted ion current was measured at various surfaces throughout the injection system with a biased electrometer. An aluminum plate was mounted to the DC quadrupole deflector 180° from the ion trap analyzer, and was biased at -60 volts. The extraction lens was maintained at -10 volts (for a source of ions with a narrow energy distribution). Both tube lenses were maintained at -55 volts, and opposite pairs of rods were maintained at ground and -150 volts depending on which direction ions were deflected. The top trace (Trace A) in Figure 5-23 shows the ion current detected when the DC quadrupole deflector was biased such that it sent ions to this crude Faraday collector. Notable in this plot is the very wide energy transmission of the quadrupole deflector (60 eV energy range). The maximum at relatively high energies (on the right shoulder of this trace) is attributed to fringing fields between the quarter round rods and the collector. The hyperbolic field of a round rod quadrupole is only ideal very near the center of the field, far from the electrodes.

The ion current which was transmitted through the DC quadrupole deflector and the second tube lens to the entrance endcap of the ion trap analyzer was monitored in a similar fashion. The polarities of the quadrupole rods were reversed, and the entrance endcap of the ion trap analyzer was biased at -60 volts. The detected ion current is shown in Trace B of Figure 5-23. This is a narrower, more symmetric trace since the quadrupole deflector followed by the tube lens serves as an energy selector, allowing transmission of only those ions which exit near the center of the gap between adjacent quadrupole rods. The energy acceptance of the quadrupole is shown in this case to be around 20 eV.

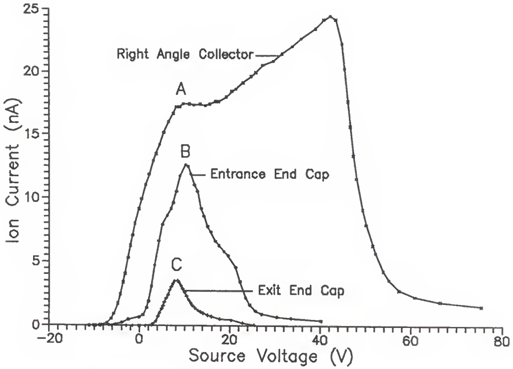

Figure 5-23: Ion current plotted as a function of source potential, measured at various places in the quadrupole deflector system. The source voltage was varied, with a constant potential applied to the extraction and tube lenses.

The ion current which was transmitted through the DC quadrupole deflector, the second tube lens, and into the ion trap through the entrance aperture of the grounded entrance endcap was measured by an electrometer connected to the exit endcap of the ion trap analyzer which was biased to -60 V. In this experiment, there is yet another small aperture to narrow the energy transmission of the DC quadrupole deflector system. Trace C of Figure 5-20 shows the energy transmission of the DC quadrupole deflector system through to this point. The width of transmitted energies is around 18 volts at the base, still a fairly wide energy acceptance.

Transmission and Detection Efficiencies

Characterization of transmission efficiencies throughout the system. The ability of the DC quadrupole deflector to efficiently deflect ions 90° was evaluated by first measuring the ion current that was collected on a biased aluminum plate attached to the quadrupole block assembly 180° from the ion source, when the quadrupole rods were all at the same potential (essentially a field-free region), and then comparing that value to the ion current measured when ions were deflected 90° to a similar aluminum Faraday plate. A remarkable 98% of the ions were bent 90° by the DC quadrupole deflector.

From Figure 5-23, it can be seen that at an ion source voltage of 8 volts, 60 to 70% of the ion current exiting the DC quadrupole deflector is transmitted through the tube lens to the entrance endcap. Approximately 20% of the ions exiting the DC quadrupole deflector actually make it through the entrance aperture of the endcap into the quadrupole ion trap analyzer. Figure 5-24 shows a summary of the transmission efficiency through the DC quadrupole deflector injection system. The small lines drawn adjacent to the quadrupole deflector represent the Faraday collectors; the long horizontal line represents the exit endcap of the ion trap.

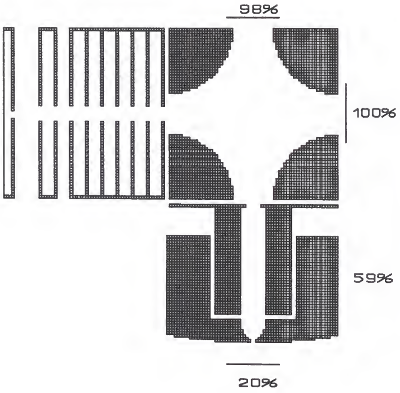

Figure 5-24: Summary of the transmission efficiencies of the quadrupole deflector injection system with an ion source potential of 8 volts.

The loss of ion current upon transmission from the DC quadrupole deflector through the tube lens is expected, since the tube lens does have a fairly small entrance aperture compared to the width of the gap between adjacent quadrupole rods; furthermore, losses may occur since some divergence of the ion beam in the z direction is expected during transmission through the DC quadrupole deflector. The large loss in ion current which occurs upon transmission of ions through the entrance endcap of the quadrupole ion trap is presumably due to the fact that there is only a single small hole to allow the entrance of ions into the analyzer. This loss may be minimized by injecting ions through a multiplier endcap of the ion trap which has seven holes (rather than just one) arranged in a honeycomb pattern through which ions could enter. One disadvantage of injection through the multi-hole endcap is the fact that the ion beam could not be so effectively defocused during injection into the ion trap, as shown in Figure 5-10, using a "filament" endcap. As pointed out earlier, theoretical studies (88) have suggested that ions injected at large angles into the trap are more efficiently trapped.

Detection efficiency measurements. An important concept in the characterization of the injection of ions into a quadrupole ion trap from any external source is that of the detection efficiency. The detection efficiency is defined here as the overall efficiency of detecting ions which are injected into the quadrupole ion trap mass spectrometer. Inherent to detection efficiency are three factors: the efficiency of capturing injected ions; the efficiency of storing the captured ions in the hyperbolic field until they are mass selectively ejected from the trap to be counted by the multiplier; and the efficiency of transferring ions from the hyperbolic field inside the ion trap analyzer to the detector, during mass selective ejection.

Theoretically, the efficiency of capturing injected ions is expected to be very low; ions can be captured only during a narrow range of phases of the RF cycle (88). The fraction of injected ions which can be captured remains to be estimated by simulations. The efficiency of storing the captured ions in quadrupole field until mass selective ejection is presumed to be extremely high (approaching unity) in a quadrupole ion trap mass spectrometer, based on the fact that long ion trapping times result in minimal loss in ion signal (except for losses due to ion-molecule reactions). The efficiency of transferring ions from within the quadrupole ion trap analyzer through the multiplier endcap is known to suffer from some loss, simply because half of the ions which are mass selectively ejected from the ion trap will be ejected through each endcap; since the multiplier is only detecting ions ejected from one of the two endcaps, the efficiency can be no more than 50%.

The overall detection efficiency was experimentally determined by comparison of the ion current which reached the exit endcap of the ion trap analyzer (i.e. the ion current entering the ion trap measured using an electrometer) with the ion current calculated from the intensity of the ion signal detected at the multiplier, normalized to the time period of the ionization gate pulse. An electrometer biased at -60 volts was connected to the exit endcap of the quadrupole ion trap mass analyzer. A current of 10 eV argon ions was continually injected into the ion trap with no RF voltage applied to the ring electrode, and the ion current reaching this biased electrode was measured using an electrometer.

The average number of multiplier counts which constitutes a single ion event was determined by statistical analysis of the detector signal for a series of single ion events. FORTH user programs for data extraction were provided by Gloria Kirchner and John Syka of Finnigan Corporation. For the -1550 Volt multiplier voltage used in these experiments, one ion event was found to correspond to 7 data system counts. Ions were injected into the quadrupole ion trap mass analyzer, collected, and detected as in a typical ion injection experiment. The detected ion intensities were converted into ion currents using the relationship of 7 counts per ion event, and dividing the number of detected ions by the gate pulse time.

Transmission and detection efficiency as a function of ion energy. The effects of ion injection energy on efficiency of transmission of ions into the ion trap analyzer as well as on the ultimate detection efficiency were studied in six separate experiments, with ion injection energy ranging from 5 to 32 eV. Argon 40^+ ions were created in the CI ion source under high pressure conditions (200 millitorr pressure as measured using a thermocouple gauge), and were injected into the ion trap analyzer using the DC quadrupole deflector injection system. Ion injection time consisted of two 500 microsecond pulses, with ionization RF level set at low mass exclusion limit of 17 and then 19 amu, yielding q values of 0.386, and 0.431 for injected argon 40^+ ions. These two ion injection RF levels were used to average out the effects of nonlinear resonances (fine structure in intensity versus q plot) in the measured data. The high pressure of argon gas inside the ion source was used both to maximize ion current, and to minimize the fraction of measured ion current due to helium ions. If helium ions had constituted a large fraction of the ion current measured with the electrometer, the resulting measured efficiencies would be artificially low, since the helium ions would not be stored in the ion trap analyzer under these experimental conditions and hence would not be detected.

Helium was plumbed directly into the ion trap analyzer to yield a pressure of approximately 1.4 millitorr inside the ion trap analyzer. All experiments were performed under the same experimental conditions, with source and lens voltages varied for optimal detection efficiency after storage and ejection. An extraction lens voltage of -314 volts was used in all experiments, which allows for maximum extracted ion current, but does result in an ion beam with a fairly wide energy range (see previous section). All direct current measurements using the electrometer were corrected for a constant leakage current, presumably due to electrically leaky vacuum feed-throughs. The measured ion currents represent the average of 5-13 sequential measurements; the calculated ion currents detected by the electron multiplier represent the average of 30 sequential measurements.

The transmission efficiency of ions through the entrance endcap of the ion trap analyzer was calculated by measuring the current of ions which is detected by applying a biased electrometer (-60 volts) to the entrance endcap of the ion trap analyzer, and comparing that current with the current of ions which is detected when the exit endcap of the ion trap analyzer is biased.

Figure 5-25 shows the percentage of ion current which travels through the entrance endcap of the ion trap analyzer as a function of source potential (injection ion energy relative to ground). Due to the wide range of ion energies (+/-10 eV) transmitted from the ion source, and the fact that the source voltage corresponds to the maximum ion energy and not the average energy of ions traveling through the entrance endcap of the ion trap analyzer, optimum transmission efficiency occurred at source voltages near +5 volts (with 25% of ions transmitted through this endcap), not 0 volts as would be expected. This figure does show the energy dependence of ion transmission through the entrance endcap, which is to be expected, since the grounded endcap will serve as a diverging lens for any positive ions formed at a positive potential relative to ground. For low energy ions, this diverging effect has been modeled (see Figure 5-10), and has been determined to be

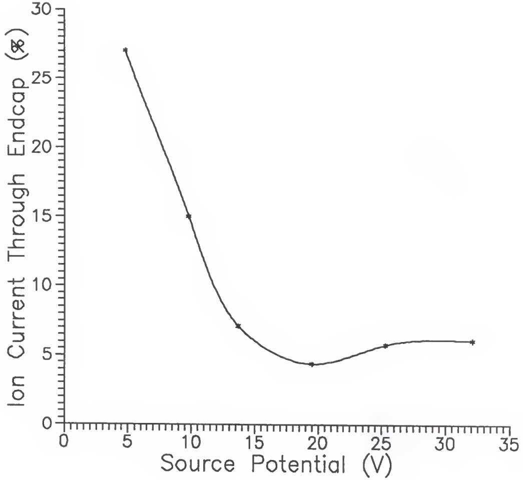

Figure 5-25: Percentage of ion current which travels through the entrance endcap of the ion trap analyzer plotted as a function of source potential.

theoretically beneficial for collection efficiency. Based on SIMION simulations, it is not expected that higher energy ions will be focused through the entrance endcap aperture by this diverging field; rather, it is expected that a larger percentage of higher energy ions will instead strike the entrance endcap itself. Furthermore, the trapping efficiency of ions injected into a quadrupole ion trap is theoretically optimum at low energies (88); as a result, the poor transmission into the trap at high energies is not viewed as a significant problem.

Figure 5-26 includes two plots, one showing the detection efficiency of ion injection as a function of ion energy, and one showing the effects of the transmission efficiency of ions through the entrance endcap of the ion trap analyzer multiplied by the detection efficiency of ions injected into the ion trap analyzer. The detection efficiency of ions injected, stored, and ultimately ejected, is shown to have a definite energy dependence, similar to the energy dependence of transmission through the entrance endcap, highest at low energies (0.1% with +5 volts applied to the source). When one considers the multiplicative effect of the transmission efficiency through the entrance endcap and the detection efficiency of ions which make it through that endcap, that is, when one considers the detection efficiency of ions which have traveled through the quadrupole deflector system (which has been shown to have an excellent transmission efficiency of 60-70%), into the ion trap analyzer, it is evident that lower ion injection energies (a few eV) will yield an order of magnitude better sensitivity than higher ion injection energies (>15 eV). Although these detection efficiency numbers may seem low, it must be considered that the detection efficiency for ions created inside the trap is unknown but may indeed be comparably low. In addition, these measurements make the assumption that every ion

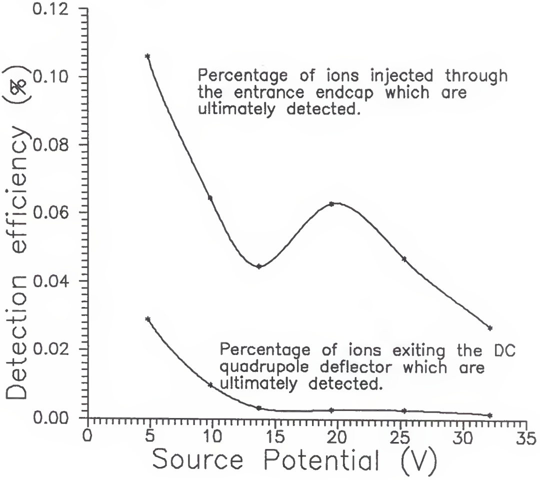

Figure 5-26: Detection efficiencies of ion injection system plotted as a function of ion source potential.

striking the entrance to the detector will be detected; clearly this assumption will lead to an underestimate of the ion current stored and ultimately detected.

Conclusions

The work described in this chapter was the result of a six-month collaborative research effort which successfully achieved the goals we had set: the conceptualization, design, construction, and evaluation of a mass spectrometer system incorporating the selective injection of positive and negative ions from an external high pressure ion source into a quadrupole ion trap analyzer. The concept employed of 90° deflection ion optics is a dramatic departure from previous simple on-axis ion optics designs (33, 34, 35), and offers significant practical advantages.

This work demonstrates the use of the DC quadrupole deflector to extract ions from the stream of neutral molecules flowing from a high pressure CI ion source by diverting them 90° into a quadrupole ion trap mass spectrometer. The DC quadrupole deflection system was used to selectively inject positive or negative ions with energies ranging from a few eV to 80 eV into a quadrupole ion trap mass spectrometer. Collection efficiency, and hence sensitivity, is greatest at lower ion energies, as predicted by previous simulations (88). Both positive and negative ions were injected into the ion trap mass analyzer with no noticeable mass discrimination. While absolute sensitivity measurements remain to be performed, the apparent instrumental sensitivity with the injection of low energy ions is comparable to the traditional ion trap operational mode of internal ionization.

The off-axis orientation of ion source to the mass analyzer, inherent with the use of the DC quadrupole deflector, coupled with excellent transmission efficiency, makes the

DC quadrupole deflector ideal for use in transferring ions from a high pressure ion source to a mass spectrometer. Indeed, the DC quadrupole may be used in a novel approach to reduce the need for differential pumping (and its associated complexity, cost, size and weight) by allowing the diversion of the flow of gas from the source away from the mass analyzer. The coupling of such ion sources as an atmospheric sampling glow discharge source with a quadrupole ion trap mass analyzer would certainly benefit from the use of this off-axis design. In the case where the neutrals exiting the source pose not just a gas-load or pressure problem, but also a chemical reactivity problem (e.g., O_2, H_2O, or glycerol from an atmospheric sampling, LC/MS, or FAB ion source), this is a particularly powerful advantage. One could envision the use of a "cold finger" (liquid nitrogen cooled target) to freeze out such unwanted chemicals. The compact nature of the quadrupole deflector coupled by its non-line-of-sight orientation of the ionizer with the analyzer should make implementation of a "cold finger" very simple indeed.

An additional benefit inherent in the use of a DC quadrupole deflector is its discrimination in the transmission of CID fragments formed external to the ion source. This discrimination is a result of the energy dependence of ion transmission through the DC quadrupole deflector. CID fragment ions retain only a fraction of the energy of their parents, and hence may not have sufficient energy to be transferred through the DC quadrupole deflector. In addition, ions formed external to the ion source by such ion-molecule reactions as proton transfer and charge exchange may not have sufficient energy for transmission through the DC quadrupole deflector because they are formed at lower potentials than those ions created in the source. The exception to this discussion was described in this chapter, namely charge exchange which may occur within the confines of the ion trap.

A final benefit arising from the use of a DC quadrupole for ion injection into a mass analyzer is the opportunity to select ions from multiple ion sources arranged around the quadrupole from injection. The sample DC deflection quadrupole offers positions for mounting three ion sources (two off-axis and one on-axis) onto one mass analyzer; the tandem DC quadrupole deflector (Figure 5-7) would permit selection of ions from five different sources. A three-dimensional quadrupole employing eight quarter-sphere balls mounted on the corners of a cube would also permit the use of as many as five sources.

Experiments with the DC quadrupole deflector ion injection system are continuing in the Yost laboratory at the University of Florida. A duplicate set of ion optics was produced during the project at Finnigan.

CHAPTER 6
CONCLUSIONS AND FUTURE WORK

Conclusions

The primary motivation for performing the work presented in this dissertation was my quest for understanding the cause of experimental phenomena. When I was introduced to quadrupole ion trap mass spectrometry in early 1987, I became fascinated with the white "black box" which symbolizes the Finnigan ion trap. I sought to understand the theory behind resonance excitation, why variation in resonance excitation voltage resulted in a variation in effective collision energy, and why the resonance excitation daughter experiment resulted in poor collection efficiency and low effective collision energy for low values of q. I thus created the HyperIon simulation program to help in the interpretation of experimental results, starting with a kernel graciously provided by William Fies Jr. of Finnigan Corporation.

The derivation of the Mathieu equation which is presented in Chapter 2 was originally pieced together prior to, and without the assistance of, the excellent book of March and Hughes (22), and is presented in such a way that there not be 'leaps of faith' required by a reader who is trying to follow the derivation. The model which was developed to describe dipolar resonance excitation is only an approximation of the true dipolar field, yet this model is useful in that it has provided information which assists in the interpretation of experimental results. In Chapter 3, a correlation between fluence magnitude and the competitive processes of ion ejection and collision-induced dissociation was predicted, with ion ejection favored at values of q_z which are greater than 0.85 or less than 0.2, and collision-induced dissociation generally favored for values of q_z between 0.2 and 0,85. The axial modulation technique for extending the mass range of the quadrupole ion trap is thus predicted to be most efficient (i.e. requiring minimum excitation voltage) for resonance ejection at $q=0.2$ or lower.

The interpretation by Wuerker et al. of the frequency of the low amplitude ripple in the famous photograph of the trajectory of an aluminum microparticle was corrected through analytical theory in Chapter 2, and through Hyperlon simulation in Chapter 3. This high frequency ripple, which was erroneously identified as superposition of the drive frequency, was correctly identified as the superposition of low amplitude harmonic frequencies on the relatively large amplitude fundamental frequency as predicted by analytical solution of the Mathieu equation.

Dehmelt's model of ion kinetic energy was examined in detail, with a key assumption disproved, namely the assumption that for low q, oscillation at the fundamental frequency represents the primary source of ion kinetic energy, and thus harmonic frequencies may be neglected. Through analysis of the analytical solution of the Mathieu equation, it was demonstrated that the first harmonic frequency, while small in relative amplitude, contributes more kinetic energy in ion oscillation than does the fundamental frequency for all values of q (assuming $a=0$, $0 < q < 0.908$). A new model for the calculation of ion velocity and ion kinetic energy was developed and compared with the Dehmelt model, with Bonner's smoothed general solution model, and with Hyperlon numerical integration results. Energies estimated using this new model, dubbed the "Expanded Analytical Solution Model", are typically ten or twenty times as large as energies estimated using the Dehmelt model, opening up opportunities for re-interpretation of experimental results which had previously been interpreted based upon the Dehmelt model.

Methodologies for calculating the critical Mathieu β parameter and the relative magnitudes of the coefficients for the analytical solution of the Mathieu equation are reviewed in Chapter 2, and a BASIC computer program which uses these methods is presented as appendix A. It is demonstrated that the relative magnitude of the coefficients for a given value of β decrease with increasing frequency of ion motion.

The features of the Hyperlon computer simulation program are reviewed in Chapter 3, along with some hints for converting units from their internal representation in Hyperlon into real-world physical units. A method is described for the calculation of phase space diagrams through modification of the Hyperlon source code. Some example phase space diagrams are presented and interpreted from the perspective of ion injection experiments. It is concluded that ion injection and laser desorption experiments should be expected to exhibit some dependence of collection efficiency on RF phase, especially at values of q approaching 0.908. It is also predicted that in the absence of some damping force, an ion injected into the quadrupole ion trap will have a finite lifetime, and will ultimately be ejected from the trap. A damping force can be effected either through collisional cooling, or through resonance deceleration (dipolar, octopolar...). Through analysis of the theoretical maximum ion kinetic energy as a function of mass for a given RF voltage (calculated using the expanded analytical solution model), it was determined that maximum collection efficiency will correspond to ion energies of less than a few eV.

The kinetic energy of electrons injected into the quadrupole ion trap was studied through Hyperlon simulation, and was determined to be dependent upon the

RF phase during injection. The trajectory lifetime of an injected electron was determined to be a few nanoseconds at most phases of RF for the 1.1 MHz Finnigan MAT ion trap system. The effective electron energy was predicted to correspond to the initial electron energy plus half the applied ring potential. By comparison of experimental results of Jodie Johnson with literature data which relates sensitivity to electron energy, the predicted effective electron energy was verified.

The potential for the existence of injected low-energy electrons was identified, and experimental data was reviewed which demonstrates the existence of low energy electrons in the electron injection experiment. The effects of charge exchange on electron ionization mass spectra were reviewed, with increased fragmentation energy attributed to nitrogen and helium charge exchange.

A novel off-axis ion optics system was developed for the injection of ions into the quadrupole ion trap from a high-pressure external ion source. The ion optics modeling program SIMION was used to evaluate various potential systems, with the most suitable system built and evaluated. Collection efficiency of injected ions was observed to be maximum at low ion energies, as was predicted through analysis of theoretical maximum ion kinetic energies.

The effects of nonlinear resonances were observed in ion injection spectra. The problems associated with these nonlinear resonances were illustrated by the dramatic variation of the relative intensities of the negative ions of bromine isotopes m/z 79 and 81, with small changes in trapping RF voltage. Measured ratios varied from 1:3 to 3:1, compared to the naturally occurring isotopic ratio of 1.03:1. These nonlinear resonances are attributed to hexapolar, octopolar and higher order fields in the ion trap which are due to non-ideal electrode geometry, and to the presence of the holes in the endcap electrodes. Note that it was Jae Schwartz who originally demonstrated the dependence of ion injection sensitivity on RF voltage to this researcher, and who recommended further characterization of this phenomenon. The conclusion that these results are due to nonlinear resonances was presented as early as the 1989 ASMS meeting, yet it wasn't until a few years later that other researchers focused on this problem with storage efficiency in the Finnigan ion trap.

The occurrence of a local maximum at an apparent iso-β line corresponding to β_z=1/2 may be attributed to resonance damping of injected ions by the octopolar field induced in the quadrupole ion trap by the stretched trap geometry. An ion injected 180^0 out of phase with this octopolar field would be predicted to have its trajectory damped similar to the resonance damping illustrated in Figure 3-4. Since an octopolar field strength reduces with r^4, once an octopolar field damps the ion away from the endcap, the effects of the octopolar field are reduced; therefore, it is predicted that the ion would never be brought back into resonance with the resonance field, contrary to what is shown in Figure 3-4 with a dipolar field. An ion injected in phase with this octopolar field frequency will be resonance ejected. These experiments should be repeated with careful consideration given to the exact orientation of the relative minima and maxima relative to iso-β lines.

The quadrupole deflector ion injection system has some unique features which make it especially suitable for filtering ions prior to injection into the quadrupole ion trap, or any mass analyzer. The primary feature of the quadrupole deflector is its ability to efficiently transport ions from the ionizer to the analyzer, independent of the potential difference between the ionizer and analyzer. Thus injection ion energy can be varied without loss in transport efficiency. The fact that an ionizer can be placed off-axis from the analyzer allows for the coupling of high pressure or 'noisy' ion sources with the quadrupole ion trap. Ions are deflected to the analyzer exclusive of neutrals and photons. A final benefit of the quadrupole deflector ion injection system is the capability of coupling multiple ion sources with a single analyzer. One may direct ions from a selected ionizer through selection of quadrupole deflector voltages.

Future Work

The recent emergence of the quadrupole ion trap as a high performance mass analyzer has brought a significant amount of focus to investigation of its fundamental operating principles. A number of approaches for the characterization of the fundamental essence of quadrupole ion trap mass spectrometry were reviewed and developed in this dissertation, yet this work barely scratches the surface of this fascinating emerging technology. There are a number of areas for focus which have occurred to this researcher and which were either tentatively explored and subsequently abandoned, or were identified as a result of analysis of this research during the preparation of this dissertation some three years after the last ion trap spectrum was taken by this researcher. This section summarizes some of the more interesting opportunities for research which stem from the research presented in this dissertation.

Analysis of the fundamental equations of motion and of the analytical solution of the Mathieu equation has proved extremely fruitful in both understanding the physics of the quadrupole ion trap, and in learning some of the intricacies of ion trap operation. The development of the expanded series solution model for ion kinetic energy originated with a quest for identifying a reliable method of calculating the relative amplitudes of the coefficients for the Mathieu equation. There are numerous alternatives and variations to the equations presented in Chapter 2 for the calculation of these coefficients presented in reference 42. These equations were utilized with varying degrees of success. For example, equation 2.50 does not seem to yield correct answers for any cases other than for n=1. Other equations found in reference 42 didn't seem to yield correct answers under any conditions. It would be interesting to investigate another method for the calculation of the coefficients to verify the accuracy of the method presented in this dissertation. While the Hyperlon results tracked the calculated relative coefficients, there are discontinuities present in the plot of the relative coefficients calculated via continued fraction equations which are not present in the Hyperlon data. The validity of these discontinuities deserves further exploration.

The analytical solution of the Mathieu equation was explored for RF-only operation of the quadrupole ion trap in this dissertation. When RF-DC operation was modeled through calculation of the relative magnitudes of the coefficients, the results from Hyperlon differed dramatically from the analytical solution method. Since there was a wealth of information to be extracted from RF-only operation, investigations into energetics of RF-DC were abandoned. The study of ion energetics for RF-DC operation of the quadrupole ion trap should be pursued at some later date, accompanied by phase space analysis of the same conditions. Specifically, selective mass storage through application of DC pulses to the ring electrode could be modeled through analytical theory.

The claim that the Dehmelt approximation underestimates ion kinetic energy by a factor of ten to twenty is a bold call indeed. Experimental verification of these calculated energies could help validate the expanded analytical solution method for estimation of maximum ion kinetic energies.

It would be predicted that Hyperlon and the expanded analytical solution method for the calculation of maximum ion kinetic energies would yield identical results, if both methods were equally accurate. Yet there is a discrepancy in the calculated ion kinetic energies for high values of q calculated by the two methods. What is most curious is that both methods result in similar relative magnitudes for the various harmonic frequencies. This discrepancy should be explored further.

Values for calculated fluence required for ion ejection were demonstrated for RF-only operation of the quadrupole ion trap. It would be interesting to calculate the 'fluence stability diagram' using both RF and DC voltages. It is predicted that resonance excitation along iso-β lines corresponding to non-zero values of a may yield significantly different fluences. If the relative fluence can be demonstrated to increase as the value of a is made more negative (i.e. positive DC voltages for positive ions), then there is the potential for increasing the amount of energy which may be internalized for a resonated ion, while simultaneously reducing the low mass cutoff of the quadrupole ion trap, extending the daughter ion mass range.

Early versions of Hyperlon included the provision for the modeling of the effects of damping of ion trajectories through collision of ions with a bath gas (typically helium) (57). Two models were developed based on Langevin collision theory, one implemented as a constant viscous drag, scaled based on the number density of the buffer gas and on the polarizability of the neutral molecule, and a second which used the same parameters to determine the collision frequency, with kinetic energy partitioned into center-of-mass coordinates, effectively transferring some fraction of ion kinetic energy between the slow moving helium atom and the fast moving ion. It was determined that Langevin collision theory was not suitable for calculation of collision frequency for the interaction of fast moving ions with thermal helium molecules, and grossly overestimates the mean time between collisions. Recent discussions with Dr. Stephen Penn of Millipore Extrel confirmed this conclusion; Dr. Penn has recommended that an elastic sphere collision model would be more suitable where ion kinetic energies exceed an eV or so. The development of an accurate model for collisions with buffer gas would allow for powerful predictions concerning the internalization of kinetic energy, and thus energy available for dissociation in resonance excitation experiments.

The fluence calculations presented in this work could be readily validated by experimentally determining the fluence required for ejection of a stored ion. Such experiments were performed by this researcher a number of years ago at the University of Florida, but those data were invalidated by the recent identification of mechanical misalignment of the electrodes of the analyzer used in those experiments.

Simulation and experimental characterization of fluence should allow for a priori prediction of the optimum conditions for a resonance excitation collision-induced dissociation experiment. Some relationships should be established which relate mass, RF voltage and q or β. The hypothesis that fluence required for ejection reduces at high values of q correlates with changes in the radius of the phase-space acceptance ellipse should be explored further.

The Hyperlon simulation program could be modified to include hexapolar, octopolar, and higher order terms. As well, the model for dipolar resonance excitation presented in reference 23 may also be included into the Hyperion program, with a comparison made to the plate capacitor model presented in this work.

Experimental verification of the presence of low-energy electrons in the quadrupole ion trap could be performed as described in Chapter 4. A system which injects electrons into the quadrupole ion trap at specific RF phases could be used to investigate the occurrence of low-energy electrons. A probe molecule should be chosen which has high sensitivity for electron capture ionization to a pseudo-molecular ion , and which also yields some dissociative electron capture fragments (e.g. carbon tetrachloride). The intensity of the dissociative electron capture fragment to the pseudo-molecular ion would be indicative of the effective energy of the injected electrons.

The most obvious use of the quadrupole deflector ion injection system is to couple the quadrupole ion trap mass spectrometer with a liquid chromatography interface such as thermospray or electrospray, or with a fast atom bombardment ion source (FAB). Fast moving neutrals are especially problematic with the FAB source, such neutrals are naturally excluded from injection into the ion trap by the right angle orientation of the ionizer relative to the analyzer and detector.

APPENDIX A
ANALYTIC.BAS SOURCE CODE

The following listing is the source code for Analytic, the Turbo BASIC program which was used to calculate Tables 2-1 to 2-5. The algorithms used in this program are discussed in Chapter 2, and are reviewed briefly here. This listing includes code to perform the calculation of relative amplitudes of characteristic coefficients for the analytical solution of the Mathieu equation and the calculation of β, given a and q. Certain code sections could conceivably extracted from this listing to calculate the q-a values which fall on a given iso-β line, as discussed in Chapter 2.

```
' ----------------------------------------------------------------------
'
'
'     Analytic.BAS                         Version 1.00
'
'
'     Written by     Randall E. Pedder
'                    Univ. of Florida
'                    Gainesville, Florida  32611
'
'        Copyright 1992 by Randall E. Pedder and Richard A. Yost.
'
'-----------------------------------------------------------------------

   CLS

   DEFDBL A-Z                      'All variables are double precision
   DIM COFF(20)                    'temporary storage for coefficient ratios
   DIM CO(20)                      'storage for coefficient results
                                   '  COFF(10) is CO


   KEV=1.602E-19                   'Charge on an electron
   KAMU=1.6605E-27                 'Mass equivalent of an amu in kg
   MASS = 134
   RADIUS = 0.007825               ' set for Finnigan Stretched trap r zero

   OMEGA = 2 * 3.1415926 * 1100000!  ' in radians/second

   OPEN "T2-1.DAT" FOR OUTPUT AS #1
OPEN "T2-2.DAT" FOR OUTPUT AS #2
OPEN "T2-3.DAT" FOR OUTPUT AS #3
OPEN "T2-4.DAT" FOR OUTPUT AS #4
OPEN "T2-5.DAT" FOR OUTPUT AS #5

A=0                         'A - Mathieu Parameter a

FOR I=1 TO 21

  READ Q                    'Q - Mathieu Parameter q

  GOSUB CalcBeta            'Result of CalcBeta is B, for Beta

  IF B>1 THEN GOTO SHORTCUT             ' If couldn't calculate beta.

  FOR R=-6 TO 6
     GOSUB CalcCoefficients             'Calculate C2N/(C2N-2)
     COFF(R+10)=CoefFrac1
  NEXT R

  CO(10+0) = 1                    'Calculate the relative intensities

  CO(10+1) = COFF(10+1)
  CO(10+2) = COFF(10+2) * CO(10+1)
  CO(10+3) = COFF(10+3) * CO(10+2)
  CO(10+4) = COFF(10+4) * CO(10+3)
  CO(10+5) = COFF(10+5) * CO(10+4)

  CO(10-1) = 1 / COFF(10)
  CO(10-2) = COFF(10-2) * CO(10-1)
  CO(10-3) = COFF(10-3) * CO(10-2)
  CO(10-4) = COFF(10-4) * CO(10-3)
  CO(10-5) = COFF(10-5) * CO(10-4)

  SUM=0                                 ' for normalization
  FOR S=-5 TO 5
     SUM= SUM + ABS(CO(10+S))
  NEXT S

  PRINT #1, USING "#.####";Q;  : PRINT #1, CHR$(09);
  PRINT #1, USING "##.####"; ABS(CO(10)/SUM*100);
   PRINT #1, CHR$(09);

  PRINT #2, USING "#.####";Q;  : PRINT #2, CHR$(09);
  PRINT #2, USING "#.######";B;  : PRINT #2, CHR$(09);
  PRINT #2, USING " ####.###"; ABS((B/2)*1100);
   PRINT #2, CHR$(09);

  PRINT #3, USING "#.####";Q;  : PRINT #3, CHR$(09);
  PRINT #3, USING "#.######";B;  : PRINT #3, CHR$(09);
  PRINT #3, USING "#######"; RADIUS*ABS(CO(10)/SUM*B/2*OMEGA);
  PRINT #3, CHR$(09);

  PRINT #4, USING "#.####";Q;  : PRINT #4, CHR$(09);
  PRINT #4, USING "#.######";B;  : PRINT #4, CHR$(09);"  ";CHR$(09);


  PRINT #5, USING "#.#######";Q;  : PRINT #5, CHR$(09);
  PRINT #5, USING "#.######";B;  : PRINT #5, CHR$(09);"  ";CHR$(09);


  FOR R=1 TO 4
```

```
      PRINT #1, USING "##.#######"; ABS(CO(10-R)/SUM*100);
      PRINT #1, CHR$(09);
      PRINT #1, USING "##.#######"; ABS(CO(10+R)/SUM*100);
      PRINT #1, CHR$(09);

      PRINT #2, USING " +####"; (B/2-R)*1100; : PRINT #2, CHR$(09);
      PRINT #2, USING " +####"; (B/2+R)*1100; : PRINT #2, CHR$(09);

      PRINT #3, USING "#######";RADIUS*ABS(CO(10-R)/SUM*(B/2-R)*OMEGA);
      PRINT #3, CHR$(09);
      PRINT #3, USING "#######"; RADIUS*ABS(CO(10+R)/SUM*(B/2+R)*OMEGA);
      PRINT #3, CHR$(09);
     NEXT R

     PRINT #1,
     PRINT #2,
     PRINT #3,

     VELOCITY=0

     FOR R=-5 TO 5
        VELOCITY = VELOCITY + ABS(RADIUS*CO(10+R)*(B/2+R)*OMEGA/SUM)
     NEXT R

     PRINT #4, USING "#####.####"; VELOCITY; : PRINT #4, CHR$(09);
     PRINT #4, USING "#####.####"; RADIUS*B/2*OMEGA;
      PRINT #4, CHR$(09);
     PRINT #4, USING "#####.####"; Q/2/2^0.5*RADIUS*OMEGA

     VOLTAGE = Q*MASS*13.768

     PRINT #5, USING "####.#####"; VELOCITY^2 * (MASS*KAMU)/(KEV*2);
     PRINT #5, CHR$(09);

     ENERGYTEMP= (RADIUS*B/2*OMEGA)^2 * (MASS*KAMU)/(KEV*2)
     PRINT #5, USING "####.#####"; ENERGYTEMP;
     PRINT #5, CHR$(09);

      ENERGYTEMP = (Q/2/2^0.5*RADIUS*OMEGA)^2*(MASS*KAMU)/(KEV*2)
     PRINT #5, USING "####.#####"; ENERGYTEMP
     PRINT #5, CHR$(09);

     PRINT #5, USING "####.#####"; VOLTAGE*Q/8; : PRINT #5, CHR$(09);
     PRINT #5, USING "####.#####"; VOLTAGE


     PRINT USING " #.####" ;Q,
     PRINT USING " ####.####"; VELOCITY^2 * (MASS*KAMU)/(KEV*2),
     PRINT USING " ####.####"; (RADIUS*B/2*OMEGA)^2*MASS*KAMU/KEV/2,
      PRINT USING " ####.####"; VOLTAGE*Q/8

ShortCut:

   NEXT I

   STOP


CalcCoefficients:             'Calculate ratio of C2N/(C2N-2)

     R2B  = (2*R+B)^2
     R22B = (2*R+2+B)^2
     R24B = (2*R+4+B)^2
     R26B = (2*R+6+B)^2
     R28B = (2*R+8+B)^2

     CoefFrac5 = Q^2/(R28B*R26B)/(1-A/(R28B-CoefFrac6))
     CoefFrac4 = Q^2/(R26B*R24B)/(1-A/(R26B-CoefFrac5))
     CoefFrac3 = Q^2/(R24B*R22B)/(1-A/(R24B-CoefFrac4))
     CoefFrac2 = Q^2/(R2B*R22B)/(1-A/(R22B-CoefFrac3))
     CoefFrac1 = -Q/R2B /(1-A/(R2B - CoefFrac2))

     RETURN

     STOP

CalcCoefficientsA:

     R2N2B = (2*R-2+B)^2
     R2N4B = (2*R-4+B)^2
     R2N6B = (2*R-6+B)^2
     R2N8B = (2*R-8+B)^2
     R2N10B = (2*R-10+B)^2

     CoefFrac5a = Q^2/(R2N8B*R2N10B)/(1-A/R2N10B-CoefFrac6a)
     CoefFrac4a = Q^2/(R2N6B*R2N8B)/(1-A/R2N8B-CoefFrac5a)
     CoefFrac3a = Q^2/(R2N4B*R2N6B)/(1-A/R2N6B-CoefFrac4a)
     CoefFrac2a = Q/(R2N4B)/(1-A/R2N4B-CoefFrac3a)
     CoefFrac1a = (-R2N2B+a)/q + CoefFrac2a

   RETURN

CalcBeta:

     B= (abs(A + Q*Q/((2+A+Q*Q/2)^2-A)))^.5

     counter = 0
     R=1

     gosub CalcCoefficients
     gosub CalcCoefficientsA

     WHILE ABS((CoefFrac1-CoefFrac1a)/b)>0.00001
        counter=counter+1

        gosub CalcCoefficients
        gosub CalcCoefficientsA


        b= b +abs(b)^0.5*(coeffrac1a-coeffrac1) /log(counter+10)

            'The choice of scaling factor for adjusting beta is tricky.

            'With too small an increment, the algorithm is inefficient.

            'With too large an increment, the algorithm may oscillate.

            'In this case we are using an adaptive step size.

            'The log factor allows the system to start with big steps,
            '  and decrease the step size with increasing numbers of
            '  iterations.
        if abs(b)>1 then return

     WEND

return

'                 Values of q for table listing

DATA 0.0001, 0.001, 0.005, 0.01, 0.05, 0.1, 0.2, 0.3, 0.4, 0.5
DATA 0.6, 0.7, 0.75, 0.8, 0.85, 0.875, 0.9, 0.9025, 0.905, 0.9075, 0.908
```

APPENDIX B
HYPERION.BAS SOURCE CODE

The following listing is the source code for Hyperlon, a Turbo BASIC program which was used extensively in this dissertation to calculate the trajectories and energetics of ion motion in a quadrupole ion trap. The looping structure which controls the program is a do..while loop, set up to check whether an ion is still within the confines of the ion trap with each increment of RF phase. Time is measured in phase increments as counted using the global parameter I. Since every variable in this program is global in nature, care must be taken when modifying this code to be certain that changes do not have ramifications in other parts of the code. The main differences between this listing and the runtime version are the removal of the fast Fourier transform routines and the removal of the screen dump routine. See Chapter 3 for more details on how to use Hyperlon.

```
' ----------------------------------------------------------------------
'
'
'     HyperIon.BAS                          Version 3.00
'
'
'     Written by     Randall E. Pedder
'                    Univ. of Florida
'                    Gainesville, Florida  32611
'
'        Copyright 1992 by Randall E. Pedder and Richard A. Yost.
'
'
'     This program traces its roots to the basic program QUADRZ.BAS
'     which was written by William J. Fies Jr. of Finnigan MAT Inc.
'
'-----------------------------------------------------------------------

'  Set global environment parameters
     $STACK 4096
     DEFDBL A-Z           '      Double Precision for all variables.
     DEF SEG=0            '      DEFINE MEMORY SEGMENT
     POKE (&H417),64      '      TOGGLE CAPS LOCK KEY ON

'  Initialize physical constants
     QELEC=1.602E-19       'Quantum charge in coulombs  (1/(dynes/eV)
     KAMU=1.6605E-27       'Conversion factor from kilograms to amu
     PI=3.14159

     ZZERO=.007825         'Z radius (from center to endcap in meters
     XZERO=.01             'Radius of the ion trap ring in meters
     YZERO=.01             'Radius of the ion trap ring in meters
     FREQ=1100000!         'Hz
     DELTPH=360/16         'Degrees to advance each iteration


'  Identify initial conditions

     VDC=0                 'Volts DC applied to ring.
     VAC=553.49            'Volts AC peak applied to ring.
     MASS=134              'Mass of the model ion in amu

     X=-.0003              'Initial position in X direction in meters
     Y=.0004               'Initial position in Y direction in meters
     Z=.0005               'Initial position in Z direction in meters

     XDOTEV0=.0269         'Vel. in X direction -thermal velocity in eV
     YDOTEV0=.0269         'Vel. in Y direction -thermal velocity in eV
     ZDOTEV0=.0269         'Vel. in Z direction -thermal velocity in eV

     INITPH=180            'Initial phase (degrees)
     I=0                     'Global time counter with units
                                '               radians/deltph*freq

     SCANRATE=5.55           'Rate of Analytical Scan in amu/ms
     TICKVOLT=1000           'Tickle Voltage in mV
     TICKFREQ=118.822        'Tickle Frequency in KHz

     TICKLETOGGLE=0        'Tickle off.
     HELPTOGGLE=1          'Help list at bottom of screen

'  Initial screen setup values

     PROGRAMNAME$="HyperIon Version 3.00"
     ZOOM=1               'Zoom window coordinates
     TIMEGET=0            'Toggle on-screen display of elapsed time
     LISTGET=1             'Toggle display of list of parameters

     GOSUB InitialCalc       'calculate intial values of a, q, beta...


'  Insert adjustments to initial conditions here.

'//--------------------

     INITPH=180
     DELTPH=10
     Z=0.002
     X=0.002
     Y=0.002

     QZ=.2
     GOSUB CalcRF
'     OPEN "TRAJECT.DAT" FOR OUTPUT AS #1

'\\--------------------

     GOSUB SetupScreen       'initialize screen
     GOSUB PauseContinue     'Pause until user hits <F10>

     PRESET (X,Z)            'display initial value.

     INSIDETRAP=1            'indicates that ion is still inside ion trap

     WHILE INSIDETRAP=1      'Do-while construct for looping.
                               '      Stop when exit trap.

        GOSUB CheckBoundaries

        IF TIMEGET=1 THEN GOSUB DisplayTime

        I=I+1                'Increment time counter

        IF DELTRF<>0 THEN GOSUB CalcRFandQ   'if scanning RF...

        GOSUB RungeKutta  'calculate new position

        LINE -(X,Z)    'draw trajectory

'        pset (z,zdot)  'plot phase space diagram

        'Insert any statements which are to occur with each cycle here.

        '//--------------------
        '       IF ZDOTMAX>ZDOT THEN ZDOTMAX=ZDOT
        '   PRINT #1, USING " #####.##"; I/OMEGA*1000000!
        '   PRINT #1, USING " +#.#######";Z,
        '\\--------------------

     WEND

     GOSUB DisplayTime
     GOSUB DisplayList
     GOSUB PauseContinue      'Wait for a keystroke.

'    CLOSE #1                 'Close the file...

     STOP                     'Stop the program here before subroutines.


'\\-------------------------------------------------------------------

CalcA:       'Given: mass, VDC and a bunch of constants, calculate az,
ax
     AZ=-4*QELEC*VDC/(MASS*KAMU*OMEGA2*(RZERO2 +2 * ZZERO2))*4
     AX=-AZ/2
     AY=-AZ/2
     RETURN

CalcDC:
      VDC = AZ/(-4*QELEC)*(MASS*KAMU*OMEGA2*(RZERO2 +2 * ZZERO2))/4
      AX=-AZ/2
      AY=-AZ/2
```

```
       RETURN

CalcInitVelocity:
      XSGN=SGN(XDOTEV0)
      YSGN=SGN(YDOTEV0)
      ZSGN=SGN(ZDOTEV0)
      XDOT=XSGN*SQR(2*QELEC*ABS(XDOTEV0)/(MASS*KAMU))/(PI*FREQ)
      YDOT=YSGN*SQR(2*QELEC*ABS(YDOTEV0)/(MASS*KAMU))/(PI*FREQ)
      ZDOT=ZSGN*SQR(2*QELEC*ABS(ZDOTEV0)/(MASS*KAMU))/(PI*FREQ)
      UTOT=SQR(XDOT^2+YDOT^2+ZDOT^2)
      UDOTMAX=UTOT
      RETURN

CalcQ:
      QZ= 2*QELEC*VAC/(MASS*KAMU*OMEGA2* (RZERO2 +2*ZZERO2)) * 4
      QX=-QZ/2
      QY=-QZ/2
      RETURN

CalcRF:  'Given qz and mass, calculate VAC
      VAC =  QZ/2/QELEC*(MASS*KAMU*OMEGA2* (RZERO2 +2*ZZERO2))/4
      QX=-QZ/2
      QY=-QZ/2
      RETURN

CalcRFandQ:  'Increment RF and q during RF ramp.
      VAC=VAC+DELTRF
      GOSUB CALCQ
      IF LISTUPDATE=1 THEN GOSUB DisplayList
      RETURN

ChangeA:
      AZ = FNChangeValue("az",AZ)
      AX=-AZ/2
      AY=AX
      GOSUB CalcDC
      GOSUB DisplayList
      RETURN

ChangeDC:
      VDC = FNChangeValue("DC Voltage=",VDC)
      GOSUB CalcA
      GOSUB DisplayList

      RETURN

ChangeRF:
      VAC = FNChangeValue("RF Voltage=",VAC)
      GOSUB CalcQ
      GOSUB DisplayList
      RETURN

ChangeDeltaPhase:
      TEMP=FNChangeValue("Delta Phase",DELTPH)
      IF TEMP <>0 THEN DELTPH=TEMP
      DELTXI=DELTPH*2*PI/360
      GOSUB DisplayList
      RETURN


ChangeMass:
      TEMP=FNChangeValue("Mass",MASS)
```

```
     IF TEMP <>0 THEN MASS=TEMP
     GOSUB CalcA
     GOSUB CalcQ
     GOSUB DisplayList
     RETURN

ChangePhase:
     PHASE=FNChangeValue("Phase",360*(XI/2/PI-INT(XI/2/PI)))
     XI=PHASE*2*PI/360
     RETURN

ChangeQ:
    QZ = FNChangeValue("qz",QZ)
    QX=-QZ/2
    QY=QX
    GOSUB CalcRF
    GOSUB DisplayList
    RETURN

ChangeScanRate:
     SCANRATE=FNChangeValue("Scan Rate (amu/ms)",SCANRATE)
     GOSUB DisplayList
     RETURN

ChangeTIckleVoltage:
     TICKVOLT=FNChangeValue("Tickle Voltage (mV)",TICKVOLT)
     GOSUB DisplayList
     RETURN

ChangeTickleFrequency:
     TICKFREQ=FNChangeValue("Tickle Frequency (kHz)",TICKFREQ)
     GOSUB DisplayList
     RETURN

ChangeX:
     X=FNChangeValue("X",X)
     GOSUB DisplayList
     RETURN

ChangeXdot:
     XDOT=FNChangeValue("X dot",XDOT)
     GOSUB DisplayList
     RETURN

ChangeY:
     Y=FNChangeValue("Y",Y)
     GOSUB DisplayList
     RETURN

ChangeYdot:
     Ydot=FNChangeValue("Y dot",YDOT)
     GOSUB DisplayList
     RETURN

ChangeZ:
     Z=FNChangeValue("Z",Z)
     GOSUB DisplayList
     RETURN

ChangeZdot:
     Zdot=FNChangeValue("Z dot",ZDOT)
     GOSUB DisplayList
     RETURN

CheckBoundaries: '-----------------------------------------------\\

     'See if ion is still inside ion trap

     IF ABS(Z)>2*ZZERO THEN GOTO ZFail
     IF ABS(Z)<ZZERO THEN GOTO CheckrBoundary
     IF ABS(Z) < 0.005*sqr(2) * SQR(1 + (X^2+Y^2)/XZERO^2)  THEN GOTO
CheckrBoundary
  ZFail:
     INSIDETRAP=0
     IF LISTGET=1 THEN GOSUB DisplayList

  CheckrBoundary:
     IF SQR(X^2+Y^2)> 0.02 THEN GOTO RFail
     IF SQR(X*X+Y*Y)< 0.01 THEN RETURN
     IF SQR(X^2+Y^2) < XZERO * SQR(1 + Z^2 / (0.005*sqr(2))^2) THEN
RETURN
  RFail:
     INSIDETRAP=0
     IF LISTGET=1 THEN GOSUB DisplayList
  RETURN  '---------------------------------------------------------//

ClearList:
     SELECT CASE HELPTOGGLE
       CASE 0
         LISTBOTTOM=21
       CASE 1
         LISTBOTTOM=18
       CASE 2
         RETURN
       END SELECT

     FOR JUNK=4 TO LISTBOTTOM
        LOCATE JUNK,1
        PRINT SP20$+" "
        LOCATE 1,1
     NEXT JUNK
     RETURN

ClearScreen:
     CLS
     GOSUB DrawTrap
     GOSUB DISPLAYLIST
     RETURN

DisplayHelp:
     RESTORE
     DATA "Zoom ","Scan ","Tickle ","List ","Time ", "Clear ","Pause "
     LOCATE 25,1
     FOR JUNK=2 TO 10
        COLOR 14
          PRINT "<F";
          IF JUNK=3 THEN JUNK=5
          IF JUNK<10 THEN PRINT USING "#";INT(JUNK);
          IF JUNK=10 THEN PRINT USING "##";INT(JUNK);
          PRINT ">";
        COLOR 15
          READ HELPINPUT$
          PRINT HELPINPUT$;
     NEXT JUNK
     COLOR 14 :  Print "<esc>";
     COLOR 15  :  Print "END";
     RETURN

DisplayList:
     COLOR 15
     Energy=FNCalcEnergy(mass,udotmax)
     LowMass=qz/.908*mass
     BETA=FNCalcBeta(QZ,AZ)
     IF HELPTOGGLE=2 THEN RETURN
     LOCATE 4,1
     PRINT "    Mass (a):"; : PRINT USING "+####.####";MASS
     PRINT " VDC (Volts):"; : PRINT USING "+####.##";VDC
     PRINT "           az:"; : PRINT USING "  +##.####";AZ
     PRINT " VAC (Volts):"; : PRINT USING " ####.##";VAC
     PRINT "           qz:"; : PRINT USING "  +##.####";QZ
     PRINT
     PRINT "Low Mass (a):"; : PRINT USING " ####.##";LowMass
     PRINT "ResFrq (kHz):"; : PRINT USING "#####.###";BETA/2*FREQ/1000
     PRINT
     PRINT " Max KE (eV):  ";:print using "###.###";energy

     PRINT
     IF TICKLETOGGLE=1 THEN PRINT " Tickle (mV):";
     PRINT USING "#####.#";TICKVOLT
     IF TICKLETOGGLE=1 THEN PRINT "  Freq (kHz):";
     PRINT USING "#####.###";TICKFREQ
     IF TICKLETOGGLE=1 THEN PRINT

     IF SCANTOGGLE=1 THEN PRINT   " Scan (a/ms):";
     Print Using "#####.##";SCANRATE
     RETURN

DisplayTime:
     CYCLE=I*DELTPH/360
     TIME=CYCLE/FREQ*1000000!
     LOCATE 1,65
     PRINT "TIME:";
     PRINT USING "####.##";TIME;:PRINT " us"
     RETURN

DisplayZoom:
     LOCATE COMMANDA+1,COMMANDB+20
     IF MONITOR$="E" THEN COLOR 12
     PRINT "ZOOM =";
     PRINT USING "###.##";ZOOM
     IF MONITOR$="E" THEN COLOR 7
     RETURN

DrawTrap:
     TRAPCOLOR=14
     TRAPRLIM=0.02
     TRAPZLIM=TRAPRLIM*0.707
     TRAPRSTART=(XZERO^2+2*TRAPZLIM^2)^0.5

     PSET (TRAPRSTART,TRAPZLIM),TRAPCOLOR
     FOR TRAPZ=-TRAPZLIM TO TRAPZLIM STEP 0.00025
       TRAPR=(XZERO^2+2*TRAPZ^2)^0.5
       LINE-(TRAPR,TRAPZ),TRAPCOLOR
     NEXT TRAPZ

     PSET (-TRAPRSTART,TRAPZLIM),TRAPCOLOR
     FOR TRAPZ=-TRAPZLIM TO TRAPZLIM STEP 0.00025
       TRAPR=-(XZERO^2+2*TRAPZ^2)^0.5
       LINE-(TRAPR,TRAPZ),TRAPCOLOR
     NEXT TRAPZ

     TRAPZSTART=(ZZERO^2+TRAPR^2)^0.5
     PSET (TRAPRLIM,TRAPZSTART),TRAPCOLOR
     FOR TRAPR=-TRAPRLIM TO TRAPRLIM STEP 0.00025
       TRAPZ=(ZZERO^2+TRAPR^2)^0.5
       LINE-(TRAPR,TRAPZ),TRAPCOLOR
     NEXT TRAPR

     PSET (TRAPRLIM,-TRAPZSTART),TRAPCOLOR
     FOR TRAPR=-TRAPRLIM TO TRAPRLIM STEP 0.00025
       TRAPZ=-(ZZERO^2+TRAPR^2)^0.5
       LINE-(TRAPR,TRAPZ),TRAPCOLOR
     NEXT TRAPR

     PRESET (X,Z)
     RETURN

GetInterrupt:
     INTER$=INKEY$  ' ALLOW FOR INTERRUPTIONS
     IF INTER$="" THEN RETURN
     IF LEN(INTER$)=1 THEN GOSUB GetInterruptQWERTY
     IF LEN(INTER$)=2 THEN GOSUB GetInterruptFunction
     RETURN

GetInterruptQWERTY:     '   Check to see if QWERTY key was pressed.
     IF ASC(INTER$)=27 THEN GOSUB Quit           'escape.

     IF INTER$="A" THEN GOSUB ChangeA
     IF INTER$="D" THEN GOSUB ChangeDeltaPhase
     IF INTER$="M" THEN GOSUB ChangeMass
     IF INTER$="P" THEN GOSUB ChangePhase
     IF INTER$="Q" THEN GOSUB ChangeQ
     IF INTER$="S" THEN GOSUB ChangeScanRate
     IF INTER$="T" THEN GOSUB ChangeTickleVoltage
     IF INTER$="t" THEN GOSUB ChangeTickleFrequency
     IF INTER$="U" THEN GOSUB ChangeDC
     IF INTER$="V" THEN GOSUB ChangeRF
     IF INTER$="x" THEN GOSUB ChangeXdot
     IF INTER$="X" THEN GOSUB ChangeX
     IF INTER$="y" THEN GOSUB ChangeYdot
     IF INTER$="Y" THEN GOSUB ChangeY
     IF INTER$="z" THEN GOSUB ChangeZdot
     IF INTER$="Z" THEN GOSUB ChangeZ


     RETURN

GetInterruptFunction:  '   Check to see if a function key was pressed.
     INTER=ASC(RIGHT$(INTER$,1))

     'F1-F10 (59-68)

     IF INTER=60 THEN GOSUB ZoomIn
     IF INTER=63 THEN GOSUB ToggleScan
     IF INTER=64 THEN GOSUB ToggleTickle
     IF INTER=65 THEN GOSUB ToggleList
     IF INTER=66 THEN GOSUB ToggleTime
     IF INTER=67 THEN GOSUB ClearScreen
     IF INTER=68 THEN GOSUB PauseContinue

     'SHIFT F1-F10 (84-93)

     IF INTER=85 THEN GOSUB ZoomOut
     IF INTER=93 THEN GOSUB Quit
     RETURN


InitialCalc:             ' calculate some constants
     ZZERO2=ZZERO*ZZERO
     RZERO2=XZERO*XZERO
     OMEGA=2*PI*FREQ
     OMEGA2=OMEGA*OMEGA
     DELTXI=DELTPH*2*PI/360   '2 PI TO CONVERT FROM HERTZ TO RADIANS
     DELTT=DELTXI/(2*PI*FREQ)
     XI=INITPH*2*PI/360

     GOSUB CalcA
     GOSUB CalcQ
     GOSUB CalcInitVelocity
     RETURN

PauseContinue:
      IF PAUSESTOP=0 THEN PAUSESTOP=1 ELSE PAUSESTOP=0
        IF PAUSESTOP=0 THEN RETURN
           LOCATE 22,1
           IF MONITOR$="E" THEN COLOR 14
           PRINT "Pausing"
           PRINT "Press F10 to continue";
           IF MONITOR$="E" THEN COLOR 7

        WHILE PAUSESTOP=1      'IF PAUSE KEY WAS PRESSED, WAIT FOR INPUT
           GOSUB GetInterrupt
           IF TIMEGET=1 THEN GOSUB DISPLAYTIME
        WEND
        LOCATE 22,1
        PRINT "         "
        PRINT "                      "
      RETURN

Quit:
      TIMEGET=0
      PAUSESTOP=0
      Locate 2,25
      PRINT "PROGRAM TERMINATED BY THE USER";
      STOP
      RETURN


RungeKutta:  '--------------------------------------------------\\

     IF INSTAT=-1 THEN GOSUB GetInterrupt

     ICOS1=-(AX-QX*2*COS(2*XI))*DELTXI
     ICOS2=-(AX-QX*2*COS(2*(XI+0.5*DELTXI)))*DELTXI
     ICOS3=-(AX-QX*2*COS(2*(XI+DELTXI)))*DELTXI

     'start of Runge-Kutta integration routine for X

     A1=XDOT*DELTXI
     B1=ICOS1*X
```

```
A2=(XDOT+.5*B1)*DELTXI
B2=ICOS2*(X+.5*A1)
A3=(XDOT+.5*B2)*DELTXI
B3=ICOS2*(X+.5*A2)
A4=(XDOT+B3)*DELTXI
B4=ICOS3*(X+A3)
DELTX=(A1+2*A2+2*A3+A4)/6
X=X+DELTX
XDOT=XDOT+(B1+2*B2+2*B3+B4)/6

'start of Runge-Kutta integration routine for Y

A1=YDOT*DELTXI
B1=ICOS1*Y
A2=(YDOT+.5*B1)*DELTXI
B2=ICOS2*(Y+.5*A1)
A3=(YDOT+.5*B2)*DELTXI
B3=ICOS2*(Y+.5*A2)
A4=(YDOT+B3)*DELTXI
B4=ICOS3*(Y+A3)
DELTY=(A1+2*A2+2*A3+A4)/6
Y=Y+DELTY
YDOT=YDOT+(B1+2*B2+2*B3+B4)/6

SELECT CASE TICKLETOGGLE

  CASE 0
    A1=ZDOT*DELTXI
    B1=-2*ICOS1*Z
    A2=(ZDOT+.5*B1)*DELTXI
    B2=-2*ICOS2*(Z+.5*A1)
    A3=(ZDOT+.5*B2)*DELTXI
    B3=-2*ICOS2*(Z+.5*A2)
    A4=(ZDOT+B3)*DELTXI
    B4=-2*ICOS3*(Z+A3)

 CASE 1
    TICKQ=-QELEC*TICKVOLT*0.001/(MASS*KAMU*OMEGA2*ZZERO)
                        '.001 TO CHANGE FROM mV TO V

    TICKXI= XI + PI/360*TICKPHASE

    ALPHABETA=TICKFREQ/FREQ*2000
    TICKCOS1=TICKQ*COS(ALPHABETA*TICKXI)*DELTXI
    TICKCOS2=TICKQ*COS(ALPHABETA*(TICKXI+0.5*DELTXI))*DELTXI
    TICKCOS3=TICKQ*COS(ALPHABETA*(TICKXI+DELTXI))*DELTXI

    A1=ZDOT*DELTXI
    B1=-2*ICOS1*Z-TICKCOS1
    A2=(ZDOT+.5*B1)*DELTXI
    B2=-2*ICOS2*(Z+.5*A1)-TICKCOS2
    A3=(ZDOT+.5*B2)*DELTXI
    B3=-2*ICOS2*(Z+.5*A2)-TICKCOS2
    A4=(ZDOT+B3)*DELTXI
    B4=-2*ICOS3*(Z+A3)-TICKCOS3

END SELECT

DELTZ=(A1+2*A2+2*A3+A4)/6
Z=Z+DELTZ

ZDOT=ZDOT+(B1+2*B2+2*B3+B4)/6
```

```
     UDOT=SQR(XDOT*XDOT+YDOT*YDOT+ZDOT*ZDOT)

     IF UDOT>UDOTMAX THEN UDOTMAX=UDOT          'get max velocity.

     XI=XI+DELTXI

     RETURN  '------------------------------------------------------//

SetUpScreen:

     SP5$="     "
     SP10$="          "
     SP15$="               "
     SP20$="                    "
     SP25$="                         "
     SP40$="                                        "
     SP80$=SP40$+SP40$
     STANDARD=.0122 '     INITIAL WINDOW VALUE FOR Z DIRECTION IN METERS

     SCREEN 9

     X1W1=190:X2W1=638  'FIRST SCREEN
     Y1W1=41:Y2W1=319

     X1W0=X1W1:X2W0=X2W1      'ASSIGN FIRST SCREEN AS DEFAULT
     Y1W0=Y1W1:Y2W0=Y2W1

     NEWSTAND=STANDARD/ZOOM
     VIEW (X1W0,Y1W0)-(X2W0,Y2W0),,3
     WINDOW (-NEWSTAND,-NEWSTAND*0.85)-(NEWSTAND,NEWSTAND*0.85)
     CLS
     GOSUB DrawTrap
     LOCATE 1,1
     PRINT SP80$;
     PRINT SP80$
     LOCATE 1,1
     COLOR 14      'YELLOW
     PRINT PROGRAMNAME$;
     GOSUB DisplayHelp
     GOSUB DisplayList
     PRESET (X,Z)
     RETURN


ToggleList:
      IF LISTGET=0 THEN LISTGET=1 ELSE LISTGET=0
      IF LISTGET=0 THEN GOSUB ClearList
      IF LISTGET=1 THEN GOSUB DisplayList
      RETURN

ToggleScan:
     IF SCANTOGGLE=0 THEN SCANTOGGLE=1 ELSE SCANTOGGLE=0
     SELECT CASE SCANTOGGLE
     CASE 0
      DELTRF=0
     CASE 1
     '     INCREMENT RF:(amu/ms)*(volts/amu)*(us/ms)/(increments/us)
     DELTRF=SCANRATE*4*.0056197/(360/DELTPH)
     END SELECT
     GOSUB CLEARLIST
     GOSUB DISPLAYLIST
     RETURN
```

```
ToggleTickle:
     IF TICKLETOGGLE=0 THEN TICKLETOGGLE=1 ELSE TICKLETOGGLE=0
     GOSUB CLEARLIST
     GOSUB DISPLAYLIST
     RETURN

ToggleTime:
     IF TIMEGET=0 THEN TIMEGET=1 ELSE TIMEGET=0
     IF TIMEGET=0 THEN LOCATE 1,65:PRINT SP15$:LOCATE 2,65:PRINT SP15$
     RETURN

ZoomIn:   ' Increase the zoom factor for scaling the trajectory
on-screen.
     ZOOM = ZOOM * 2
     GOSUB SetUpScreen
     RETURN

ZoomOut:    '     Decrease Zoom factor.
     ZOOM=ZOOM/2
     IF ZOOM <1 THEN ZOOM=1
     GOSUB SetUpScreen
     RETURN

DEF FNCalcBeta(Q,A)
     B= (ABS(A + Q*Q/((2+A+Q*Q/2)^2-A)))^.5
     COUNTER = 0
     R=1
     COEFFFRAC1 = 1
     COEFFFRAC2 = 0
     WHILE ABS((COEFFRAC1-COEFFRAC1a)/B)>0.00001
        COUNTER=COUNTER+1
        R2B  = (2*R+B)^2
        R22B = (2*R+2+B)^2
        R24B = (2*R+4+B)^2
        R26B = (2*R+6+B)^2
        R28B = (2*R+8+B)^2

        COEFFRAC6=0
        COEFFRAC5 = Q^2/(R28B*R26B)/(1-A/(R28B-COEFFRAC6))
        COEFFRAC4 = Q^2/(R26B*R24B)/(1-A/(R26B-COEFFRAC5))
        COEFFRAC3 = Q^2/(R24B*R22B)/(1-A/(R24B-COEFFRAC4))
        COEFFRAC2 = Q^2/(R2B*R22B)/(1-A/(R22B-COEFFRAC3))
        COEFFRAC1 = -Q/R2B /(1-A/(R2B - COEFFRAC2))

        R2N2B = (2*R-2+B)^2
        R2N4B = (2*R-4+B)^2
        R2N6B = (2*R-6+B)^2
        R2N8B = (2*R-8+B)^2
        R2N10B = (2*R-10+B)^2

      COEFFRAC6A=0
        COEFFRAC5A= Q^2/(R2N8B*R2N10B)/(1-A/R2N10B-COEFFRAC6A)
        COEFFRAC4A = Q^2/(R2N6B*R2N8B)/(1-A/R2N8B-COEFFRAC5A)
        COEFFRAC3A = Q^2/(R2N4B*R2N6B)/(1-A/R2N6B-COEFFRAC4A)
        COEFFRAC2A = Q/(R2N4B)/(1-A/R2N4B-COEFFRAC3A)
        COEFFRAC1A = (-R2N2B+A)/Q + COEFFRAC2A

        B= B + ABS(B)^0.5*(COEFFRAC1A-COEFFRAC1) /LOG(COUNTER+10)

        IF ABS(B)>1 THEN COEFFRAC1 = COEFFRAC1A

     WEND
     IF ABS(B) > 1 THEN B=0
     FNCalcBeta = B
END DEF

DEF
FNCalcEnergy(MASS,VELOCITY)=MASS*KAMU*(VELOCITY*2*PI*FREQ)^2/(2*QELEC)

DEF FNChangeValue(LABEL$,OLDVALUE)
     LOCATE 1,25
     PRINT LABEL$;"=";
     PRINT USING "#####.#####";OLDVALUE
     LOCATE 2,25
     INPUT "New value:";NEWVALUE
     LOCATE 1,25 : PRINT SP40$
     LOCATE 2,25 : PRINT SP40$
     lOCATE 1,25
     IF NEWVALUE=0 THEN INPUT "Are you sure you want zero";JUNK$
     LOCATE 1,25 : PRINT SP40$

     if NEWVALUE=0 THEN IF JUNK$<>"Y" THEN NEWVALUE=OLDVALUE

     FNChangeValue=NEWVALUE
END DEF
```

REFERENCES

1 Paul, W.; Steinwedel, H. "Apparatus For Separating Charged Particles of Differing Specific Charges" U.S. Patent 2,939,952, June 7, 1960.

2 Fischer, E. "Three-dimensional Stabilization of Charge Carriers in a Quadrupole Field" Zeit. fur Physik **1959**, *156*, 1-26.

3 Dawson, P.H. *Quadrupole Mass Spectrometry and its Applications*, Dawson, P.H., Ed.; Elsevier: Amsterdam, 1976.

4 Stafford, G.C.; Kelley, P.E.; Bradford, D.C."Advanced Ion Trap Technology in an Economical Detector for GC" *Amer. Lab* June **1983** 51-57.

5 Louris, J.; Schwartz, J.; Stafford, G.C.; Syka, J.E.P.; Taylor, D. "The Paul Ion Trap Mass Selective Instability Scan: Trap Geometry and Resolution" *Proceedings of the 40th ASMS Conference on Mass Spectrometry and Allied Topics*, Washington, DC, May 31 - June 5, 1992, 1003-1004.

6 Wuerker, R.F.; Shelton, H.; Langmuir, R.V. "Electrodynamic Containment of Charged Particles" *J. Appl. Phys.* **1959,** *30*, 342-349.

7 Dawson, P.H.; Whetten, N.R. "Ion Storage in Three-Dimensional, Rotationally Symmetric, Quadrupole Fields. II. A Sensitive Mass Spectrometer " *J. Vac. Sci. Technol.* **1968**, *5*, 11-18.

8 Stafford, G.C., Jr.; Kelley, P.E.; Syka, J.E.P.; Reynolds, W.E.; Todd, J.F.J. "Recent Improvements in and Analytical Applications of Advanced Ion Trap Mass Spectrometry" *Int. J. Mass Spectrom. Ion Proc.* **1984**, *60*, 85-98.

9 Syka J.E.P.; Fies, W. J. Jr. "A Fourier Transform Quadrupole Ion Trap Mass Spectrometer" *Proceedings of the 35th ASMS Conference on Mass Spectrometry and Allied Topics*, May 24-29, 1987, Denver, CO, 767-768.

10 Dawson, P.H.; Whetten, N.R. "Ion Storage in Three-Dimensional, Rotationally Symmetric, Quadrupole Fields. I." *J. Vac. Sci. Technol.* **1968**, *5*, 1-11.

11 Dawson, P.H.; Whetten, N.R. "The Three-Dimensional Quadrupole Ion Trap" *Naturwissenschaften* **1969**, *56*, 109-112.

12 Bonner, R.F.; Lawson, G.; Todd, J.F.J. "A Low-pressure Chemical Ionisation Source: An Application of a Novel Type of Ion Storage Mass Spectrometer" *J.C.S. Chem. Comm.* **1972**, 1179-1180.

13 Lawson, G.; Bonner, R.F.; Todd, J.F.J. "The Quadrupole Ion Store (QUISTOR) as a Novel Source for a Mass Spectrometer" *J. Phys. E.: Sci. Instrum.* **1973**, *6*, 357-362.

14 Todd, J.F.J.; Waldren, R.M.; Mather, R.E.; Lawson, G. "On the Relative Efficiencies of Confinement of Ar^+ and Ar^{2+} Ions in a Quadrupole Ion Storage Trap (QUISTOR)" *Int. J. Mass Spectrom. Ion Phys.* **1978**, *28*, 141-151.

15 Todd, J.F.J.; Waldren, R.M.; Mather, R.E. "The Quadrupole Ion Store (QUISTOR). Part IX. Space Charge and Ion Stability. A Theoretical Background and Experimental Results. *Int. J. Mass Spectrom. Ion Phys.* **1980**, *34*, 325-349.

16 Mather, R.E.; Waldren, R.M.; Todd, J.F.J. "The Characterisation of a Quadrupole Ion Storage Mass Spectrometer" in *Dynamic Mass Spectrometry* **1978**, *5*, 71-84.

17 Lawson, G.; Todd, J.F.J. "Radiofrequency Quadrupole Mass Spectrometers" *Chem. Brit.* **1972**, *8*, 2-36.

18 Lawson, G.; Todd, J.F.J. "Weak Peak Enhancement by Selective Ion Trapping in a Quadrupole Ion Storage Source" *Anal. Chem.* **1977**, *49*, 1619-1622.

19 Fulford, J.E.; March, R.E.; Mather, R.E.; Todd, J.F.J.; Waldren, R.M. "The Cylindrical Ion Trap: A Theoretical and Experimental Study" *Can. J. Spectrosc.* **1980**, *25*, 85-97.

20 Fulford, J.E.; March, R.E. "A New Mode of Operation for the Three-Dimensional Quadrupole Ion Store (QUISTOR): The Selective Ion Reactor" *Int. J. Mass Spectrom. Ion Phys.* **1978**, *26*, 155-162.

21 Fulford, J.E.; Hoa, D.-N.; Hughes, R.J.; March, R.E.; Bonner, R.F.; Wong, G.J. "Radio-Frequency Mass Selective Excitation and Resonant Ejection of Ions in a Three-Dimensional Quadrupole Ion Trap." *J. Vac. Sci. Technol.* **1980**, *17*, 829-835.

22 March, R.E.; Hughes, R.J. *Quadrupole Storage Mass Spectrometry*, John Wiley and Sons: New York, 1989.

23 March, R.E.; McMahon, A.W.; Londry, F.A.; Alfred, R.L.; Todd, J.F.J.; Penman, A.D.; Vedel, F. "Resonance Excitation of Ions Stored in a Quadrupole Ion Trap Part I. A Simulation Study" *Int. J. Mass Spectrom. Ion Proc.* **1989**, *95*, 119-156.

24 March, R.E.; McMahon, A.W.; Allison, E.T.; Londry, F.A.; Alfred, R.L.; Todd, J.F.J.; Vedel, F. "Resonance Excitation of Ions Stored in a Quadrupole Ion Trap Part II. Further Simulation Studies" *Int. J. Mass Spectrom. Ion Proc.* **1990**, *99*, 109-124.

25 March, R.E.; Londry, F.A.; Alfred, R.L.; Todd, J.F.J.; Penman, A.D.; Vedel, F.; Vedel, M. "Resonance Excitation of ions Stored in a Quadrupole Ion Trap Part III. Introduction to the Field Interpolation Simulation Method" *Int. J. Mass Spectrom. Ion Proc.* **1991**, *110*, 159-178.

26 Weber-Grabau, M.; Kelley, P.E.; Bradshaw, S.C.; Hoekman, D.J. "Advances in MS/MS Analysis with the Ion Trap Mass Spectrometer" *Presented at the 36th Annual Conference on Mass Spectrometry and Allied Topics*, San Francisco, CA, June 5-10, 1988, 1106-1107.

27 Strife, R.J.; Simms, J.R.; Lacey, M.P. "Ion Trap Quantitative MS/MS Assays Using RF/DC" *Proceedings of the 37th Annual Conference on Mass Spectrometry and Allied Topics*, Miami, FL; May 21-26, 1989, 1266-1267.

28 Simms, J.R.; Strife, R.J. "Ion trap Tandem Mass Spectrometry (MS/MS) for the Determination of Eicosanoids" *Proceedings of the 37th Annual Conference on Mass Spectrometry and Allied Topics*, Miami, FL; May 21-26, 1989, 1264-1265.

29 Louris, J.N.;, Cooks, R.G.;, Syka, J.E.P.; Kelley, P.E.; Stafford, G.C. Jr.; Todd, J.F.J. "Instrumentation, Applications and Energy Deposition in Quadrupole Ion Trap Tandem Mass Spectrometry" *Anal. Chem.* **1987**, *59*, 1677-1685.

30 Kaiser, R.E. Jr.; Cooks, R.G.; Moss, J.; Hemberger, P.H. "Mass Range Extension in a Quadrupole Ion Trap Mass Spectrometer" *Rapid Commun. Mass Spectrom.* **1989**, *3*, 50-53.

31 Johnson, J.V.; Pedder, R.E.; Yost, R.A.; Story, M.A. "Quadrupole Ion Trap Mass Spectrometer Having Two Pulsed Axial Excitation Input Frequencies and Method of Parent and Neutral Loss Scanning and Selected Reaction Monitoring," U.S. Patent No. 5,075,457, December 24, 1991.

32 Pedder, R.A.; Johnson, J.V.; Yost, R.A."Electron Energy in a Quadrupole Ion Trap Mass Spectrometer" *Proceedings of the 40th ASMS Conference on Mass Spectrometry and Allied Topics*, Washington, DC, May 31 - June 5, 1992, 1761-1762.

33 Louris, J.N.; Amy, J.; Ridley, T.; Kascheres, C.; Cooks, R.G., Weber-Grabau, M.; Stafford, G.Jr. "The Quadrupole Ion Trap as a Tandem Mass Spectrometer: Instrumentation and Applications" *Presented at the 35th Annual Conference on Mass Spectrometry and Allied Topics*, Denver, CO, May 24-29, 1987, 769-770.

34 Schwartz, J.C.; Cooks, R.G.; Weber-Grabau, M.; Kelley, P.E. "Quantitative Evaluation of Ion Injection into a Quadrupole Ion Trap" *Presented at the 36th Annual Conference on Mass Spectrometry and Allied Topics*, San Francisco, CA, June 5-10, 1988, 634-635.

35 Asano, K.G.; Glish, G.L.; McLuckey, S.A. "Coupling of an Atmospheric Sampling Ion source with an Ion Trap Mass Spectrometer" *Presented at the 36th Annual Conference on Mass Spectrometry and Allied Topics*, San Francisco, CA, June 5-10, 1988, 636-637.

36 Louris, J.N.; Amy, J.W.; Ridley, T.Y.; Cooks, R.G."Injection of Ions into a Quadrupole Ion Trap Mass Spectrometer" *Int. J. Mass Spectrom. Ion Proc.* **1989**, *88*, 97.

37 Pedder, R.E.; Yost, R.A.; Weber-Grabau, M. "Injection of Ions Into a Quadrupole Ion Trap from a Chemical Ionization Source Using a DC Quadrupole Deflector" *Proceedings of the 37th Annual Conference on Mass Spectrometry and Allied Topics*, Miami, FL; May 21-26, 1989, 468-469.

38 Kaiser, R.E. Jr.;, Cooks, R.G.;, Stafford, G.C. Jr.;, Syka, J.E.P.; Hemberger, P.H. "Operation of a Quadrupole Ion Trap Mass Spectrometer to Achieve High Mass/Charge Ratios" *Int. J. Mass Spectrom. Ion Proc.* **1991**, *106*, 79-115.

39 Kaiser, R.; Lammert, S.A.; Williams, J.; Cooks, R.G.; Zakett, D. "Thermospray LC/MS with a Quadrupole Ion Trap and Recent Applications of Ion Injection" *Proceedings of the 37th Annual Conference on Mass Spectrometry and Allied Topics*, Miami, FL; May 21-26, 1989, 369-370.

40 Campana, J.E. "Elementary Theory of the Quadrupole Mass Spectrometer" *Int. J. Mass Spectrom. Ion Phys.* **1980**, *33*, 101-117.

41 Knight, R.D. "The General Form of the Quadrupole Ion Trap Potential" *Int. J. Mass Spec. Ion Phys.* **1983**, *50*, 127-131.

42 McLachlan, N.W. *Theory and Applications of Mathieu Functions*, Clarendon: Oxford, **1947**.

43 Major, F.G.; Dehmelt, H.G. "Exchange-Collision Technique for the RF Spectroscopy of Stored Ions" *Phys. Rev.* **1968**, *170*, 91-107.

44 Todd, J.F.J.; Lawson, G.; Bonner, R.F. "Quadrupole Ion Traps" *Quadrupole Mass Spectrometry and its Applications*, Dawson, P.H., Ed.; Elsevier: Amsterdam, 1976; 181-224.

45 Berberich, D.W.; Yost, R.A. "Negative Ionization in Quadrupole Ion Trap Mass Spectrometry: Effects of Applied Voltages and Reaction Times" *J. Amer. Soc. Mass Spectrom.* submitted 1992.

46 Stafford, G.C.; Kelley, P.E.; Stephans, D.R. "Method of Mass Analyzing a Sample by Use a Quadrupole Ion Trap" U.S. Patent 4,540,884, September 10, 1985.

47 Lever, R.F. "Computation of Ion Trajectories in the Monopole Mass Spectrometer by Numerical Integration of Mathieu's Equation" *IBM J. Res. Develop.* **1966**, *10*, 26-40

48 Whetten, N.R.; Dawson, P.H. "Some Causes of Poor Peak Shapes in Quadrupole Mass Analyzers" *J. Vac. Sci. Technol.* **1969**, *6*, 100-103.

49 Dawson, P.H.; Whetten, N.R. "Non-Linear Resonances in Quadrupole Mass Spectrometers Due to Imperfect Fields" *Int. J. Mass Spectrom. Ion Phys.* **1969**, *2*, 45-59.

50 Dawson, P.H.; Lambert, C. "A Detailed Study of the Quadrupole Ion Trap" *Int. J. Mass Spectrom. Ion Phys.* **1975**, *16*, 269-280.

51 Baril, M.; and Septier, A. "Ion Storage in a Three-Dimensional High Frequency Quadrupole Field" *Rev. Phys. Appl.* **1974**, *9*, 525-531.

52 Ghosh, P.K.; Arora, A.S.; Narayan, L. "Ion Path Lengths in a Three-Dimensional RF Quadrupole Trap" *Int. J. Mass Spectrom. Ion Phys.* **1977**, *23*, 237-240.

53 O,C.-S.; Schuessler, H.A. "Confinement of Pulse-Injected Ions into a Radiofrequency Quadrupole Ion Trap" *Int. J. Mass Spectrom. Ion Phys.* **1981**, *40*, 53-66.

54 O, C.-S.; Schuessler, H.A. "Confinement of Ions Injected into a Radiofrequency Quadrupole Ion Trap: Pulsed Ion Beams of Different Energies" *Int. J. Mass Spectrom. Ion Phys.* **1981**, *40*, 67-75.

55 O, C.-S.; Schuessler, H.A. "Confinement of Ions Injected into a Radiofrequency Quadrupole Ion Trap: Energy-Selective Storage of Pulse-Injected Ions" *Int. J. Mass Spectrom. Ion Phys.* **1981**, *40*, 77-86.

56 Todd, J.F.J.; Bexon, J.J.; Smith, R.D. "Stability Diagram Determination and Ion Trajectory Modeling for the Ion Trap Mass Spectrometer" *Presented at the 35th Annual Conference on Mass Spectrometry and Allied Topics*, Denver, CO, May 24-29, 1987, 787-788.

57 Pedder, R.E.; Yost, R.A."Enhancements to MS/MS in a Quadrupole Ion Trap Mass Spectrometer," *Conference on Chemical Defense Research*, November 18, 1987.

58 Pedder, R.E.; Yost, R.A. "Computer Simulation of Ion Trajectories in a Quadrupole Ion Trap Mass Spectrometer," *Proceedings of the 36th Annual*

Conference on Mass Spectrometry and Allied Topics, San Francisco, CA, June 5-10, 1988, 632-633.

59 Julian, R.K. Jr.; Reiser, Hans-Peter; Cooks, R.G. "Large Scale Simulation of Resonant Ejection in the Quadrupole Ion Trap Mass Spectrometer" *Proceedings of the 40th ASMS Conference on Mass Spectrometry and Allied Topics*, Washington, DC, May 31 - June 5, 1992, 1777-1778.

60 Reiser, H.-P.,; Julian, R.K. Jr.; Cooks, R.G. "A Versatile Method of Simulating the Operation of the Ion Trap Mass Spectrometer" *Int. J. Mass Spectrom. Ion Proc.* (In Press).

61 Lammert, S.A.; Cooks, R.G. "Evidence for RF Phase Coherence Using Surface-Induced Dissociation in the Ion trap Mass Spectrometer" *Proceedings of the 39th ASMS Conference on Mass Spectrometry and Allied Topics*, Nashville, TN, May 19-24, 1991,467-468.

62 Lammert, S.A.; Cooks, R.G. "Surface Induced Dissociation of Molecular Ions in a Quadrupole Ion Trap Mass Spectrometer" *J. Am. Soc. Mass Spectrom.* **1991**, *2*, 487-491.

63 Press, W.H.; Flannery, B.P.; Teukolsky, S.A.; Vetterling, W.T. *Numerical Recipes in C The Art of Scientific Computing* Cambridge University Press: Cambridge, U.K., 1988; 566-573.

64 Basic, C. "Probing Trapped Ion Energies in a Quadrupole Ion Trap Mass Spectrometer" Doctoral Dissertation, University of Florida, 1992.

65 Vargas, R.R.; Yost, R.A.; Lee, M.S.; Moon, S.L.; Rosenberg, I.E. "Analysis of Spiperone in a Biological Matrix using Laser Desorption/ Quadrupole Ion Trap Mass Spectrometry" *Proceedings of the 40th ASMS Conference on Mass Spectrometry and Allied Topics*, Washington, DC, May 31 - June 5, 1992, 1751-1752.

66 Williams, J.D.; Reiser, H.-P.; Kaiser, R.E., Jr. Cooks, R.G.; "Resonance Effects During Ion Injection into a Quadrupole Ion Trap Mass Spectrometer" *Int, J. Mass Spec. and Ion Proc.* **1991**, *108*, 199-220.

67 "NIST/EPA/MSDC Mass Spectral Database" National Institute of Standards and Technology, Standard Reference Data, 221/A323, Gaithersburg, MD 20899

68 Watson, J.T. *Introduction to Mass Spectrometry*, Second Ed. Raven Press: New York, 1985.

69 Harrison, A.G. *Chemical Ionization Mass Spectrometry* CRC Press: Boca Raton, FL, 1981, Chapter 2.

70 Mather, R.E.; Todd, J.F.J."The Quadrupole Ion Store (QUISTOR). Part VII. Simultaneous Positive/Negative ion Mass Spectrometry" *Int, J. Mass Spec. and Ion Phys.* **1980**, *30*, 159-165.

71 McLuckey, S.A.; Glish G, C.; Kelley, P.E. "Collision Activated Dissociation of Negative Ions in an Ion Trap Mass Spectrometer" *Anal. Chem.* **1987**, *59*, 1670-1674.

72 March, R.E.; Hughes, R.J. *Quadrupole Storage Mass Spectrometry*, John Wiley and Sons, New York, **1989**, Chapter 7.

73 Berberich, D.W.; Yost, R.A. "Negative Ionization in Quadrupole Ion Trap Mass Spectrometry: Effects of Applied Voltages" *Proceedings of the 37th Annual Conference on Mass Spectrometry and Allied Topics,*; Miami Beach, FL 1989, 1250-1251.

74 Berberich, D.W.; Orth, R.G. " Comparison of Gas Chromatograph/Mass Spectrometry Analysis of Organic Compounds Using Electron Ionization, Positive Chemical Ionization and Negative Chemical Ionization Utilizing the Ion Trap Mass Spectrometer" *Proceedings of the 38th Annual Conference on Mass Spectrometry and Allied Topics*, Tucson, AZ, June 3-8, 1990, 870-871.

75 Harden, C.S.; Wagner, P.E. "A Three Dimensional Mass Analyzer" *Presented at the 19th Annual Conference on Mass Spectrometry and Allied Topics*, Atlanta, GA, May 2-7, 1971, 246-253.

76 *CRC Handbook of Chemistry and Physics*, Weast, R.C.; Astle, M.J. Ed., 62nd edition CRC Press: Boca Raton, FL, **1981**.

77 Massey, H.S.W.;, Burhop, E.H.S. *Electronic and Ionic Impact Phenomena*, Oxford University Press: Oxford, **1952**, 265.

78 Johnson, J.V.; Pedder, R.E.; Yost, R.A. "The Stretched Quadrupole Ion Trap: Implications for the Mathieu a_u and q_u Parameters and Experimental Mapping of the Stability Diagram" Rapid Commun. Mass. Spectrom. (In Press).

79 *The ARRL Handbook for the Radio Amateur*, Wilson, M.J.; Hale, B.S. Ed., American Radio Relay League: Newington, CT. **1987**, 2-12.

80 Simms, J.R.; Strife, R.J. "Relative Ion Trap Storage Efficiencies of Ions Up to m/z 1500 by Capillary GC/MS" *Proceedings of the 39th Annual Conference on Mass Spectrometry and Allied Topics*, Nashville, TN, May 19-24, 1991, 1485-1486.

81 Griffiths, I.W.; Mukhtar, E.S.; March, R.E.; Harris, F.M.; Beynon, J.H. "Comparison of Photo-Excitation of Ions and Collisional Excitation using Gases" *Int. J. Mass Spectrom. Ion Phys.* **1981**, *39*, 125-132.

82 Baer, T.; Dutuit, O.; Mestdagh, H.; Rolando, C. "Dissociation Dynamics of n-butylbenzene Ions: The Competitive Production of m/z 91 and 92 Fragment Ions" *J. Phys. Chem.* **1988**, *92*, 5674-5679.

83 Griffiths, I.W.; Harris, F.M.; Mukhtar, E.S.; Beynon, J.H. "Calculation of the Abundance Ratio (91+/92+) From n-Butylbenzene Molecular Ions as a Function of Internal Energy" *Int. J. Mass Spectrom. Ion Phys.* **1981**, *41*, 83-88.

84 Dawson, P.H.; Lambert, C. "Pulse-Out Synchronization in the Quadrupole Ion Trap" *Int. J. Mass Spectrom. Ion Phs.* **1974**, *14*, 339-347.

85 Bier, M.E.; Hartford, R.E.; Herron, J.R.; Stafford, G.C. "Coupling a Particle Beam and a Thermospray Interface to a Quadrupole Ion Trap Mass Spectrometer" *Proceedings of the 39th ASMS Conference on Mass Spectrometry and Allied Topics*, Nashville, TN, May 19-24, 1991, 538-539.

86 Schwartz, J.C.;, Syka, J.E.P.;, Jardine, I. "High Resolution on a Quadrupole Ion Trap Mass Spectrometer" *J. Am. Soc. Mass Spectrom.* **1991**, *2*, 198-204.

87 Kleintop, B.L.; Eades, D.M.; Yost, R.A."Particle Beam/Ion Trap Mass Spectrometry for LC/MS Analysis of Compounds of Environmental Interest" *Presented at the Pittsburgh Conference on Analytical Chemistry and Applied Spectroscopy*, March 9, 1992.

88 O, C.-S.; Schuessler, H.A. "Confinement of Ions Created Externally in a Radio-Frequency Ion Trap" *J. Appl. Phys.* **1981**, *52*, 1157-1166.

89 Curtis, J.E.; Kamar, A.; March, R.E.,; Schlunegger, U.P. "An Improved Hybrid Mass Spectrometer for Collisionally Activated Dissociation Studies" *Proceedings of the 35th Annual Conference on Mass Spectrometry and Allied Topics*, Denver, CO; May 24-29, 1987; 237-238.

90 Williams, J.D.; Cox, K.; Morand, K.L.; Cooks, R.G.; Julian, R.K.; Kaiser, R.E. "High Mass-Resolution Using a Quadrupole Ion trap Mass Spectrometer" *Proceedings of the 39th ASMS Conference Mass Spectrometry and Allied Topics*, Nashville, TN, May 19-24, 1991, 1481-1482.

91 Dawson, P.H. "Fringing Fields and other Imperfections" *Quadrupole Mass Spectrometry and its Applications*, P.H. Dawson, Ed., Elsevier: Amsterdam, **1976**, 95-119.

92 Zeman, H.D. "Deflection of an Ion Beam in a 2-Dimensional Electrostatic Quadrupole Field" *Rev. Sci. Instrum.* **1977**, *48*, 1079-1085.

93 Huber, B.A.; Miller, T.M.; Cosby, P.C.; Zeman, H.D.; Leon, L.; Mosely, J.T.; Peterson, J.R. "Laser-Ion Coaxial Beam Spectrometer" *Rev. Sci. Instrum.* **1977**, *48*, 1306-1313

94 Hanson, C.D.; Castro, M.E.; Russell, D.H. "A TOF-FTMS System for Probing High Mass Analysis by FT-ICR Methods" *Proc. of the 35th Annual Conference on Mass Spectrometry and Allied Topics*, Denver, CO; May 24-29, 1987; 1152-1153

95 Dahl, D.A.; Delmore, J.E. *"The SIMION PC/PS2 User's Manual Version 4.0"* Idaho National Engineering Laboratory, EGG-CS-7233, April, 1988.

BIOGRAPHICAL SKETCH

Randy Pedder was born and raised in Westmoreland County, Pennsylvania, near the geographic center of the known universe (Pittsburgh, Pennsylvania). He attended Penn-Trafford High School, and matriculated to Saint Vincent College in Latrobe, Pennsylvania, to major in chemistry, graduating with a B.A. in 1985. By the middle of his junior year of college, he decided that graduate school was preferable to medical school, having found excitement in the challenges of instrumentation development and using computers to solve chemical problems.

He chose to attend the University of Florida in order to study under Professor Richard A. Yost, in part because of the warm environment he found in the Yost group (friendly people, that is). While studying under Dr. Yost, he focused on fundamental and instrumental aspects of quadrupole ion trap mass spectrometry. He had the great fortune of being able to participate in a joint venture between Finnigan, NASA, and the University of Florida, which allowed him to spend six months at Finnigan Corporation in San Jose, California, from Memorial Day to Thanksgiving of 1988. This work experience helped demonstrate the excitement that is offered in instrumentation development in mass spectrometry.

Randy prematurely left the University of Florida in 1989 due to family reasons, deciding to temporarily (sic) delay the finalization of his dissertation (ultimately a three year delay). Randy currently works in the Research and Development Department of Millipore Corporation's Extrel Mass Spectrometry Division in Pittsburgh, where he continues to apply fundamental principles in the development of software and instrumentation.

I certify that I have read this study and that in my opinion it conforms to acceptable standards of scholarly presentation and is fully adequate, in scope and quality, as a dissertation for the degree of Doctor of Philosophy.

Richard A. Yost, Chair
Professor of Chemistry

I certify that I have read this study and that in my opinion it conforms to acceptable standards of scholarly presentation and is fully adequate, in scope and quality, as a dissertation for the degree of Doctor of Philosophy.

James D Winefordner

James D. Winefordner
Graduate Research Professor of Chemistry

I certify that I have read this study and that in my opinion it conforms to acceptable standards of scholarly presentation and is fully adequate, in scope and quality, as a dissertation for the degree of Doctor of Philosophy.

John R. Eyler

John R. Eyler
Professor of Chemistry

I certify that I have read this study and that in my opinion it conforms to acceptable standards of scholarly presentation and is fully adequate, in scope and quality, as a dissertation for the degree of Doctor of Philosophy.

Peggy R Borum

Peggy R. Borum
Professor of Food Science and Human Nutrition

I certify that I have read this study and that in my opinion it conforms to acceptable standards of scholarly presentation and is fully adequate, in scope and quality, as a dissertation for the degree of Doctor of Philosophy.

W. W. Harrison

Willard W. Harrison
Professor of Chemistry

This dissertation was submitted to the Graduate Faculty of the Department of Chemistry in the College of Liberal Arts and Sciences and to the Graduate School and was accepted as partial fulfillment of the requirements for the degree of Doctor of Philosophy.

December, 1992

Dean, Graduate School